THE β-DECAY BRANCHING RATIOS OF THE NEUTRON-RICH NUCLEUS ^{15}B

By

Richard Harkewicz

A DISSERTATION

Submitted to
Michigan State University
in partial fulfillment of the requirements
for the Degree of

DOCTOR OF PHILOSOPHY

Department of Chemistry

1992

ABSTRACT

THE β-DECAY BRANCHING RATIOS OF THE NEUTRON-RICH NUCLEUS ^{15}B

By

Richard Harkewicz

Detailed experimental information on the β-decay properties of nuclei far from stability can provide crucial tests of the validity of shell-model Hamiltonians which have been constructed from data associated with stable and near stable nuclei. Such tests can lead to refinement of shell-model interactions. The neutron-rich boron isotopes are particularly interesting in that the ratio of neutrons to protons lies in a range of two to almost three. While progress in establishing the limits of particle stability for the boron isotopes has been quite good, suprisingly up to now much remains unknown about the decay of ^{15}B.

In the present study ^{15}B nuclei were produced at the National Superconducting Cyclotron Laboratory at Michigan State University through fragmentation of an E/A = 80 MeV ^{18}O beam from the K1200 cyclotron in a thick ^{9}Be target. The products of this reaction were then separated using the momentum-loss achromat mode of the NSCL A1200 separator. This technique provided a nearly pure beam of ^{15}B ions ($>$ 93%) which was transported to a low background experimental vault with an overall yield of approximately 600 ^{15}B ions per second. The ^{15}B ions were implanted in the center of the NSCL neutron detector array, a device designed to study the decay of β-delayed neutron emitting nuclei. The array consists of 16 proton-recoil plastic

scintillation neutron detectors which covers a total solid angle of approximately 1.9 steradians that can measure neutron energies by the time-of-flight method.

In the present work, the first β-delayed neutron spectroscopy of ^{15}B was performed, and in addition, a remeasurement of the ^{15}B half-life was made. As a result of these measurements, the ^{15}B β-decay branching ratios have been established.

The experimentally determined ^{15}B β-decay properties from the present work are compared to shell-model calculations carried out in the complete *psd* model space using the Millener-Kurath-Wildenthal interaction. Future work at the NSCL using the neutron detector array to study other β-delayed neutron emitting nuclei is suggested. Ideas concerning how the array may be improved are also provided.

ACKNOWLEDGEMENTS

It has been an honestly dynamic, eye opening, "part of me dying – part of me being born" time at the cyclotron lab (or I should more bluntly say the great Midwest) since I ventured out here four and a half years ago, coming by way of the mean, backstreets of Newark, New Jersey (*my home town*).

First off, I must thank Dave Morrissey for his guidance and belief in me during my graduate career. Dave, thanks for your patience and understanding and thank you for being an active, "always there" advisor. Thank you for your encouragement when it would have been easiest just to quit – I owe more than words can express to you Dave.

The entire staff at the lab has been true family to me and I don't know where to start in expressing my appreciation to each and everyone. Well, special thanks go out to Dennis and Anne Swan for their genuine friendship. Thanks Dennis and Anne for keeping my car running and keeping my stomach full during some cold, dark Michigan winters – I hope, one day, your garage is complete.

Thank you Jerry Nolen for all your guidance and support and thanks for letting me do what I do best – you're a natural mentor. Thank you Brad Sherrill for your exhaustive efforts in making it all work. Thanks go out to so many more friends. Dick Blue, Walt Benenson, Ed Kashy, Arron Galonsky, Harold Hilbert (thanks for letting me burn so much solder), Steve Hickson, Steve Bricker, Bob Young, Jan Mooney, Phil Fighter and the guys in the shop (where I always felt most at home), all my ^{15}B collaborators (Dave, Alex, Jerry, Brad, Nigel, John and Jeff), Renan Fontus and Tom Jones (for the electronic diagrams), Don Lawton and Rick Swanson, Al Zeller and Tim Antaya (for getting me into ultra-marathons in the 90's), Doug Harris (for teaching me to bend conduit), and all my fellow grad students (especially Don Sackett, Raman

Pfaff and Mike Lisa). I know I've left out names but you're all in my heart – I'm going to miss you wonderful people; I really mean that.

I'd like to thank my Mom, Alice, for raising the four kids and still having time for the somewhat odd last one when he came along. Thanks go out to my sister Janet, her husband Tony and my swell nephew Anthony (also my Godson); thanks for the support. I'd also like to thank my brother Ken (mi compadre) and my brother Ed. I just have to say the past is behind us, we all survived (with a few scars) and I truly love you all.

Last, and certainly not least (perhaps just saving the best for last) thank you Gena from the bottom of my heart for your understanding and just for being who you are. It's been a real journey with you and there's a place deep within me that is there for only beautiful you. Thanks Josh for being the fun kid you are and being so honest. The two of you mean a real lot to me.

Contents

LIST OF TABLES ix

LIST OF FIGURES xii

1 Introduction 1

1.1 A Brief Overview of β-Decay 3

1.2 ^{15}B and the Other Neutron-Rich Boron Isotopes 11

2 Experimental Details 16

2.1 The NSCL A1200 Radioactive Beam Facility 16

2.2 The Neutron Detector Array 21

2.3 Neutron detector efficiency 29

2.4 Comparison of the Measured (PuBe) Efficiency to a Monte-Carlo Calculated Efficiency for an Array Detector 35

2.5 Exploring Position Sensitivity with the Neutron Detector Array . . . 41

2.6 Cyclotron Beam On/Beam Off Cycles for Decay Studies 46

3 Results and Analysis 49

3.1 A Summary of the Experimental Runs Made to Measure the Decay of ^{15}B 50

3.1.1 Group One Experimental Runs 50

3.1.2 Group Two Experimental Runs 56

3.1.3 Group Three Experimental Runs 56

3.2 A Measurement of the Half-life of ^{15}B 60

3.3 ^{15}B β-Decay to ^{15}C Bound States 66

3.3.1 ^{15}C β-Decay Following the Implantation of ^{15}B 66

3.3.2 The Implantation Detector's β-Detection Efficiency 70

3.3.3 Determination of the β-Decay Branch to ^{15}C Bound States . . 78

3.4 ^{15}B β-Decay to ^{15}C Unbound States – β-Delayed Neutron Emission . 81

3.4.1 ^{15}B β-Delayed Neutron Time-of-Flight Measurements 81
3.4.2 Other Decay Channels for ^{15}B β-Delayed Neutron Emission . 96
3.5 The ^{15}B β-Decay Branching Ratios 101

4 Discussion – Comparison to Theoretical Predictions **110**
4.1 The Nuclear Shell-Model 110
4.2 Shell-Model Calculations for ^{15}B 116

5 Conclusions **121**

LIST OF REFERENCES **125**

List of Tables

1.1 Summary of the half-life measurements made for the decay of ^{15}B. Listed is the reasercher and date the measurement was published, the reaction used to produce the ^{15}B, and the reported ^{15}B half-life. . . . 14

2.1 Summary of the A1200 beam purity for the implantation of the ^{15}B secondary beam. 27

2.2 Summary of the measured neutron detection efficiencies (using the PuBe source) for the sixteen array detectors. Listed are the measured efficiencies, including the estimated error associated with each measurement, for the detection of 1.8 MeV, 3.0 MeV and 4.5 MeV neutrons. Also included is the mean and standard deviation of the sixteen measurements for the three energy bins. 34

2.3 Comparison of measured (PuBe) and calculated (Monte-Carlo) efficiencies for neutron array detector # 1 as a function of neutron energy (not including solid angle). 40

2.4 Summary of the NSCL neutron detector array specifications. 45

2.5 Beam On/beam Off ^{60}Co γ-ray source measurements used to calibrate exact times of On/Off cycles. Listed are the time cycles, number of γ events recorded during On/Off cycle, time calibration of real time clock, last channel of Off cycle time spectrum, and calculated exact times of beam On/beam Off cycles. 48

3.1 Summary of part of the experimental runs (Group One) involved with measuring the decay of ^{15}B. These runs were used to obtain a ^{15}B half-life measurement and β-delayed neutron time-of-flight spectra. Listed are the run number and corresponding on/off cycle, the time of each run, the total number of ^{15}B ions deposited in the implantation detector (per run), the A1200 ^{15}B production rate, and the total number of ^{15}B atoms (per run) remaining at the end of the implantation period (see text for explanation). 55

3.2 Summary of part of the experimental runs (Group Two) involved with measuring the decay of ^{15}B. These runs were used to measure the ^{15}B β-decay branch to ^{15}C bound states. Listed are the run number and on/off cycle (only 5 s/6 s cycle was used for these runs), the time of each run, the total number of ^{15}B ions deposited in the implantation detector (per run), the A1200 ^{15}B production rate, and the total number of ^{15}C atoms (per run) remaining at the end of the implantation period **assuming** a 100% ^{15}B β-decay branch to ^{15}C bound states (see text). 58

3.3 Summary of part of the experimental runs (Group Three) involved with measuring the decay of ^{15}B. This run was used to determine the implantation detector's β-decay detection efficiency for ^{15}C. Listed is the run number and on/off cycle (only 5 s/7 s cycle was used), the time of the run, the total number of ions deposited in the implantation detector (per run), the A1200 production rate, and the total number of atoms (per run) remaining at the end of the implantation period. . 59

3.4 Summary of the half-life, $t_{1/2}$, and true activity present at the end of the implantation period, $A_{0,true}$, obtained from the decay of ^{15}B inclusive β-emission for the Group One experimental runs (one through ten). Also included is the background component for each run and the reduced chi-square for the least-square fitting procedure. 63

3.5 Summary of the Group Two experimental runs in which ^{15}B ions were deposited into the implantation detector during a 5 s beam on period and decays were monitored during a 6 s beam off period. The decay curves from these runs were fit with a least-square procedure in which each component's decay constant was a fixed parameter and its activity was a free parameter. The components of each fit and the corresponding activity, A_0, are shown in the fourth column. The adjusted activities, $A_{0,true}$, account for the 0.375 s that elapsed between the end of implantation period and the beginning of the fit and are shown in the fifth column. The last column lists the reduced chi-square for the least-square fitting procedure. 68

3.6 Summary of the implantation detector's β-detection efficiency for the β-decay of ^{15}B from the Group One experimental runs. 74

3.7 Summary of the implantation detector's β-detection efficiency from the Group Three run. The $A_{0,true}$ values were obtained from the fitted decay curve shown in Figure 3.4; also listed is the reduced chi-square value for the least-square fitting procedure used to obtain these values. The efficiencies were deduced from these $A_{0,true}$ values and the number of atoms present at the end of the implantation period. 76

3.8 Summary of the implantation detector's β-detection measured efficiency for implantated ions from Groups One, Two and Three runs. Also listed is the "actual" average β-particle energy from the decay (see text for explanation) and the depth of implantation into the 10 mm thick implantation detector. 77

3.9 Summary of the determined ^{15}B β-decay branching ratios to ^{15}C bound states determined individually from the three experimental runs of Group Two. Also listed is the decay branch determined from the decay curve generated from the summation of these runs. 80

3.10 Summary of the calculated neutron energies from the fitted spectra of the sixteen neutron detectors. The flight path was calibrated using the lowest energy neutron peak in the fitted spectra as a standard; this peak represents a 1.759 MeV neutron and corresponds to the known 3.103 MeV state in ^{15}C. The other neutron energies shown below were calculated using this calibrated flight path and their associated peak centroid supplied by the fitting procedure. All neutron energies are in MeV. 92

3.11 Summary of the relative β-delayed neutron branching ratios for the populated states in ^{15}C determined from the results of the sixteen array detector time-of-flight measurements. Listed is the mean and standard deviation for the branching ratio percentages; first, to include the detector # 7 values, and second, to exclude them. All branching ratios are in percent. Errors associated with each detector measurement are dealt with later. 93

3.12 Summary of the relative β-delayed neutron branching ratios for the populated states in ^{15}C with their corresponding uncertainties. Also listed is the "weighted" mean and uncertainty for each branching ratio percentage. The details concerning the method used to determine the uncertainties and weighted values are explained in the text. All values are in percentage. Note that the detector # 7 values are not included. 94

3.13 Neutron energies, measured ^{15}C states (*this work*), known ^{15}C states [a], β branching and $logft$ values in ^{15}B decay. All energies are in MeV. 106

4.1 Measured and predicted Gamow-Teller β-decay strengths to the lowest $\frac{1}{2}^-$, $\frac{5}{2}^-$, $\frac{3}{2}^-$, $\frac{1}{2}^-$ and $\frac{5}{2}^-$ [a] states in mass 15; also included are the measured and predicted energy levels of ^{15}C populated. The 3.103 MeV ^{15}C level was adjusted in the shell-model calculations to match the experimental value. (BR) denotes branching ratio. All energies are in MeV. 119

List of Figures

1.1 Experimental $log ft$ values and associated types of β-decays. From K. Krane, *Introductory Nuclear Physics* (New York: John Wiley and Sons, 1988). 10

1.2 Energy level scheme of ^{15}C. From F. Ajzenberg-Selove, Nucl. Phys. **A523**, 1 (1991). 15

2.1 Schematic drawing of the NSCL A1200 radioactive beam facility and the K1200 cyclotron. 19

2.2 Schematic view of the NSCL experimental floor layout.The ^{15}B secondary beam was produced and separated at the A1200 and then transported to a low background experimental vault, some 60 meters away from the primary ^{18}O reaction. 20

2.3 Schematic drawing of the NSCL neutron detector array and the experimental setup. The numbering of each neutron detector is consecutive going from # 1 to # 16. 24

2.4 A close-up view of the detectors (implantation and the two silicon surface barrier) and associated hardware located at the center of the neutron detector array. 25

2.5 Energy spectra obtained from the ΔE detector and the veto detector (located at the center of the neutron detector array) for the implantation of the ^{15}B secondary beam. 26

2.6 Schematic drawing of the electronic setup used in the ^{15}B decay study. This setup could remain essentially the same for other β-delayed neutron decay experiments. 28

2.7 Time-of-flight spectra obtained from an array detector and the small, standard detector using the PuBe neutron source. These spectra were used, in part, in determining the neutron detector array neutron detection efficiency. The peaks labeled "flag" and "cosmic" are explained in the text. 32

2.8 Energy "bins" selected from the PuBe neutron source time-of-flight spectra. 33

2.9 Compton edges obtained in the pulse height spectrum of the standard detector using ^{60}Co and ^{134}Cs γ-ray sources. Note that the location of the Compton edge was taken to be the half-height of the edge. 37

2.10 Array detector showing the five positions a ^{60}Co source was placed in order to determine the detector's neutron threshold setting and its dependence on position. The source was collimated and placed flush against the detector. 38

2.11 Compton edges obtained, using a ^{60}Co source, from the left and right sides of array detector # 1 for the five positions shown in Figure 2.10. 39

2.12 Results of placing a collimated ^{60}Co source at the five array detector locations shown in Figure 2.10 and using the "position through timing" function (Equation 2.6). 44

3.1 Experimental decay curve for ^{15}B inclusive β-emission obtained by summing all the 20/40 cycle runs (4 through 10). The solid line corresponds to a single-component fit plus a constant background. 64

3.2 Experimental decay curve for ^{15}B requiring β-neutron coincidence. The solid line corresponds to a single-component fit plus a constant background. 65

3.3 Experimental decay curve generated by summing the three individual runs of Group Two. During these runs ^{15}B ions were deposited into the implantation detector during the 5 s beam on period and decays were monitored during the 6 s beam off period. The solid line corresponds to a three-fit component (^{6}He, ^{9}Li, ^{15}C) plus a constant background. The error bars are statistical. 69

3.4 Experimental decay curve for the Group Three experimental run. During run # 14, ^{15}C and ^{17}N ions from the A1200 were deposited into the implantation detector during a 5 s implantation period and decays were monitored during the 7 s beam off period. The solid line corresponds to a two component-fit plus a constant background. 75

3.5 Top figure is the raw, unfitted β-delayed neutron time-of-flight spectrum obtained from detector # 6. The x-axis corresponds to time, with the lowest energy neutrons in the highest channel number peak. Shown is the "fast" β-peak and the "cosmic" peak; these are explained in the text. Bottom figure is the above spectrum which has been fitted. The five unfolded β-delayed neutron peaks, with their energies, are shown. The spectrum is not corrected for neutron efficiency. The fits to individual peaks are indicated with solid lines, the background by long dashes, and the sum of all contributions by the short dashes. The fitting procedure is described in the text. 89

3.6 Fitted β-delayed neutron time-of-flight spectra obtained from the neutron array detectors # 1 through 8. 90

3.7 Fitted β-delayed neutron time-of-flight spectra obtained from the neutron array detectors # 9 through 16. 91

3.8 The β-delayed neutron decay branching ratios obtained from the different array detectors. The solid lines and values on the right are the weighted averages obtained for each of the five percentages from the detector measurements; note that the detector # 7 values are shown here but its values were not used in calculating the weighted averages. 95

3.9 Neutron energy spectrum generated from the sixteen neutron detector time-of-flight measurements. Top figure is the energy spectrum with a linear y-axis, bottom figure is the same spectrum with a log y-axis. Note the evidence of only five β-delayed neutron peaks. 99

3.10 Two dimensional spectra showing the neutron time-of-flight measurement for detector #6 (x-axis) vs. the neutron time-of-flight measurement for the fifteen other detectors (y-axis, and numbered for detector number). These spectra were used to look for two neutron coincidence events and evidence of ^{15}B β-delayed two neutron emission via the ground state of ^{13}C. 100

3.11 Efficiency curve for the polyethylene-moderated neutron detection system used by Reeder *et al.* [Re91] in their recent measurement of the ^{15}B P_{1n}. Calculated Monte-Carlo efficiencies are represented by the solid circles and experimentally determined efficiencies by the open circles. See text for a detailed explanation. 107

3.12 Experimental decay curve for ^{17}N inclusive β-emission; ^{19}O was an impurity. The solid line corresponds to a two-component fit, the reduced chi-square for this fit was 0.5. 108

3.13 Time-of-flight β-delayed spectrum obtained for the decay of ^{17}N from neutron array detector number # 6. Shown are the "fast" β-peak and the 1.702 MeV and 1.172 MeV neutron peaks. Note that the detector was not able to detect the 0.383 MeV neutrons from the decay of ^{17}N, however the spectrum location where they would be expected is shown. 109

4.1 At the left are the energy levels calculated using the Woods-Saxon potential (Eq. 4.1) alone (Intermediate form). At the right are the energy levels calculated when the spin-orbit potential is included (Intermediate form with spin orbit); notice the spin-orbit interaction splits the levels with $l > 0$ into two new levels. To the right of each energy level is, first the individual nucleon capacity of that level and, second the cumulative number of nucleons up to that level. The inclusion of the spin-orbit potential results in the magic numbers (shown in the circles) being exactly reproduced. From K. Krane, *Introductory Nuclear Physics* (New York: John Wiley and Sons, 1987). 115

4.2 Graphical comparison of the experimentally determined Gamow-Teller β-decay strengths for ^{15}B and those predicted by the theoretical shell-model for mass 15. The y-axis represents the energy levels (E_x) in ^{15}C. Refer to Table 4.1 for the actual B(GT) and E_x values. 120

Chapter 1

Introduction

β-decay is the process through which a nucleus that has an imbalance in its number of protons and neutrons can become more stable by converting a proton into a neutron or a neutron into a proton. In this process, the mass number of the nucleus, A, remains unchanged but the atomic number, Z, changes by one unit; this transformation is accompanied by the emission from the nucleus of an electron and an anti-neutrino (for neutron excessive nuclei, where a neutron is converted into a proton) or a positron and a neutrino (for proton excessive nuclei, where a proton is converted into a neutron)[1]. β-decay was one of the first forms of radioactivity to be observed, and it still provides new valuable insight into the internal structure of the nucleus. An important nuclear model, the *shell model*, was formulated nearly fifty years ago, and is able to successfully explain and predict various nuclear properties, including details of β-decay. Two important assumptions of the shell-model are (1) the nucleons within the nucleus move in a potential that they themselves create, and (2) the motion of a single nucleon is governed by a potential caused by all of the other nucleons. Detailed experimental information on the β-decay properties of nuclei far from stability are particularly important because they can provide crucial tests of the

[1]Both the electron and positron can be referred to as "β-particles", and both the neutrino and anti-neutrino can be referred to as "neutrinos" in these decays.

validity of the assumptions used to construct shell-model Hamiltonians which have been based on data associated with stable and near-stable nuclei. These tests can lead to refinement of the knowledge of shell-model interactions. With such refinements, the shell-model extrapolations for the properties of even more exotic nuclei become, of course, more reliable.

The further nuclei are from stability, the more energy they have available for decay processes and the more exotic these processes become. One such decay process is that of β-delayed nucleon emission. With the increased decay energy, the decay may populate highly excited states in the daughter nucleus and these states may subsequently decay by prompt nucleon emission[2]. The emitted nucleon may actually provide more information than the β-particle because, while the energy of the β-particle is continuous due to the decay energy being shared among three bodies, the nucleon has a definite energy determined by the energy of the populated excited state in the daughter nucleus, as this is a two body decay. By observing the emitted nucleons' energies and emission probabilities, the populations of the excited states of the daughter from the β-decay can be determined. This experimentally determined information can then be related to theoretically predicted quantities; as will be expanded upon shortly. It should also be noted that with the advancements in accelerator technology, the ability to produce nuclei further and further from stability at unprecedented rates will continue to yield new experimental data from which the shell-model can be "put to the test".

The goal of the present work was to establish the previously unknown ^{15}B β-decay branching ratios; ^{15}B already known to be a β-delayed neutron emitter. A large part of the present work involved designing, constructing and testing the *NSCL neutron*

[2]The emission of the nucleon occurs typically in 10^{-20} seconds after the excited state has been populated through the β-decay, so essentially the β-particle and nucleon are emitted from the nucleus simultaneously.

detector array, a detector array designed to study β-delayed neutron emitting nuclei. In this opening chapter, (1) some discussion of the types of β-decays will be presented (allowed and forbidden) along with an explanation of some experimentally derived quantities which bridge the gap between theory and experiment, and (2) the neutron-rich boron isotopes will be examined (with an emphasis on ^{15}B). Chapter II describes the production and separation of ^{15}B using the MSU NSCL A1200 radioactive beam device, the experimental setup, and detailed information on the neutron detector array. In Chapter III, the experimental results and analysis are presented, and the ^{15}B β-decay branching ratios established. Lastly, Chapter IV compares the experimental results to shell-model calculations carried out in the *psd* model space.

1.1 A Brief Overview of β-Decay

An entire derivation of the Fermi theory of β-decay is not the purpose of this section; the steps of this derivation can be found in almost any introdutory nuclear physics text (such as "Introductory Nuclear Physics" by K. Krane [Kr88] or "Nuclear and Radiochemistry" by Friedlander, Kennedy, Macias, and Miller [Fr81]). What will be presented here are a few tenets of Fermi's theory of β-decay explicated by K. Krane [Kr88] and D. Mikolas [Mi89] and how they relate to experimentally determined quantities. This will aid in some of the discussions which follow latter.

Fermi treated the β-decay causing interaction as a weak pertubation. Through Fermi's *Golden Rule*, he related the transition probability for β-decay, λ, to the interaction that causes the transition between an initial and final quasi-stationary state, V, and also a density of final states that is accessible during the decay, $\rho(E_f)$:

$$\lambda = \frac{2\pi}{\hbar} |V_{fi}|^2 \rho(E_f) \tag{1.1}$$

where V_{fi} is the integral of the interaction that causes the transition between the

initial and final states of the system:

$$V_{fi} = \int \psi_f^* V \psi_i dv \tag{1.2}$$

The density of final states term in the above equation has the obvious effect that a given transition is more likely to occur if there is a large number of accessible final states.

Different mathematical forms of V are available which discribe its transformation properties and its behavior under rotation and space inversion. These include, but are not limited to, the vector operator (V_V), and the axial vector operator (V_A) which will be addressed later; for now V will be used to represent either of these operators. For β-decay, the wave functions of the β-particle and the neutrino must also be considered, where ψ_f only refers to the final *nuclear* wave function, so the more complete interaction matrix element should have the form:

$$V_{fi} = g \int (\psi_f^* \varphi_\beta^* \varphi_\nu^*) V \psi_i dv \tag{1.3}$$

where g represents the β-decay strength constant and determines the strength of the transformation interaction. The β-particle and neutrino wave functions are usually assumed to have plane wave forms $\varphi_\beta(\vec{r}) \propto e^{i\vec{p}\cdot\vec{r}/\hbar}$ and $\varphi_\nu(\vec{q}) \propto e^{i\vec{q}\cdot\vec{r}/\hbar}$, where $\vec{p}$ is the β-particle momentum and $\vec{q}$ the neutrino momentum. Expanding the exponential forms of these functions gives:

$$e^{i\vec{p}\cdot\vec{r}/\hbar} = 1 + \frac{i\vec{p}\cdot\vec{r}}{\hbar} + \frac{1}{2}[\frac{i\vec{p}\cdot\vec{r}}{\hbar}]^2 + \cdots \tag{1.4}$$

$$e^{i\vec{q}\cdot\vec{r}/\hbar} = 1 + \frac{i\vec{q}\cdot\vec{r}}{\hbar} + \frac{1}{2}[\frac{i\vec{q}\cdot\vec{r}}{\hbar}]^2 + \cdots \tag{1.5}$$

Notice that in these expressions, the β-particle and neutrino wave functions depend on $\vec{r}$, the location in the nucleus where the two particles are created. If the particles are created at the nuclear origin ($r = 0$), then they cannot carry off any

orbital angular momentum ($l = 0$) and the wave functions both reduce to a value of 1. This limit is known as the *allowed* approximation and the only factors that depend on the β-particle and neutrino energy come from the density of final states. Eq. 1.3 can then reduce to:

$$M_{fi} = g \int \psi_f^* V \psi_i dv \tag{1.6}$$

where M_{fi} is the nuclear matrix element and accounts for the overlap of initial and final nuclear states.

Two types of allowed β-decay exist, called Fermi and Gamow-Teller decay and can be distinguished by the spins of the particles. In allowed Fermi decay, the β-particle and neutrino are emitted such that their intrinsic spins of 1/2 (s = 1/2) are anti-parallel and couple to zero. With $l = 0$, in Fermi decay there is no change in the spin of the nucleus. Using the standard quark-model of the nucleons, only the identity of one of the three quarks within the nucleon changes, ($[udd] \rightarrow [uud]$ for example, neutron $\rightarrow$ proton), while the spin of the nucleon, and hence the spin of the entire nucleus, remains unchanged [Mi89]. The only thing that does change is the charge of the nucleus which has been labeled the total isospin vector, T_z [3]; the isospin, T (to be described shortly), remains unchanged in pure Fermi β-decay and, as a result this quantity can be thought of as conserved during the decay and connects two states of identical nuclear wave functions[4]. All the Fermi decay strength should go into this single daughter state known as the *analog state.* In allowed Fermi decay, the transition operator is of the vector form, V_V. The charge independence of the nuclear force allows the neutron and proton to be treated as two different states of the same particle, the *nucleon.* In the absence of an electromagnetic field the proton and

[3]The total isospin vector, T_z, has the value $\frac{1}{2}(N - Z)$. The isospin of a nucleus, T, can have values ranging from $|T_z|$ to $|A/2|$.

[4]In the first order, the strong or nuclear force is not effected by the charge of a nucleon (an electromagnetic force). The daughter state connected by pure Fermi decay, the analog state, has an identical nuclear wave function to that of the parent.

neutron are degenerate. The nucleon is thus assigned a "quasi" spin vector, called the "isospin", with the isospin quantum number being $+\frac{1}{2}$ or isospin-up for the neutron and $-\frac{1}{2}$ or isospin-down for the proton.

β-decay can also occur in the Gamow-Teller mode in which the β-particle and neutrino are emitted parallel and their spins couple to a spin of S = 1. In a more microscopic picture the spin of a quark must flip, and this allows both the spin and isospin of the nucleus to change by one unit. Gamow-Teller decay populates many more states in the daughter than does Fermi decay; recall that Fermi decay is limited to feed *only* the analog state, where as Gamow-Teller decay can also feed the analog state but is not limited exclusively to it. In allowed Gamow-Teller decay, the transition operator is of the axial vector form, V_A. Also note that in either Fermi or Gamow-Teller allowed β-decay the parity of the initial and final states is not permitted to change.

β-decay selection rules can be written in terms of these permitted spin and parity changes. For allowed Fermi decay, ΔT = 0, ΔJ = 0, and $\Delta\pi$ = no. Examples of allowed pure Fermi decay are the $0^+ \rightarrow 0^+$ decays of $^{14}O \rightarrow {}^{14}N^*$ and $^{34}Cl \rightarrow {}^{34}S$; these decays cannot occur through a Gamow-Teller transition. For allowed Gamow-Teller decay, ΔT= 0 or 1; ΔJ = 0 or 1; and $\Delta\pi$ = no. Decays such as $^6He \rightarrow {}^6Li$ ($0^+ \rightarrow 1^+$) and $^{13}B \rightarrow {}^{13}C$ ($\frac{3}{2}^- \rightarrow \frac{1}{2}^-$) are pure Gamow-Teller transitions and contain no Fermi component. A decay such as n $\rightarrow$ p ($\frac{1}{2}^+ \rightarrow \frac{1}{2}^+$) can satisfy both the Fermi and Gamow-Teller selection rules and is an example of a "mixed" Fermi/Gamow-Teller transition.

In both the allowed Fermi and Gamow-Teller transitions the β-particle and the neutrino are emitted with zero orbital angular momentum. In cases where the two particles must carry off one or more units of orbital angular momentum, these decays are called *forbidden* decays – the degree of "forbiddeness" (1st, 2nd, etc.) correspond-

ing to the number of units of orbital angular momentum carried off (1 $\hbar$, 2 $\hbar$, etc.). The assumption in Eqs. 1.4 and 1.5 that the β-particle and neutrino wave functions reduce to the value of one is obviously not valid here; each succeeding term in the expansion of the exponential form of the plane wave function gives a higher order of forbiddeness. Generally, forbidden β-decay is a much more difficult process to calculate accurately than allowed decay. Since a difference in the parity of the initial and final states of a nucleus requires an odd number of orbital angular momentum units to be emitted, this represents the most frequent occurrence of forbidden decays. Selection rules for first-forbidden decays are $\Delta J = 0$, 1, or 2 and $\Delta\pi$ = yes; examples being $^{17}N \rightarrow {}^{17}O$ ($\frac{1}{2}^- \rightarrow \frac{5}{2}^+$) and $^{15}B \rightarrow {}^{15}C$ ($\frac{3}{2}^- \rightarrow \frac{1}{2}^+$). Selection rules for second-forbidden decays are $\Delta J = 2$ or 3 and $\Delta\pi$ = no; an example being $^{22}Na \rightarrow {}^{22}Ne$ ($3^+ \rightarrow 0^+$). There are also third-forbidden decays (four cases known) and fourth-forbidden decays (two cases known). As expected, the higher the order of forbiddeness, the less likely is the probability for the β-transition. If the opportunity permits, a nucleus will decay via an allowed or lowest order transition possible. Only when no other decay channel is possible, do the higher-order decays occur.

In his formulation of allowed β-decay theory, one of Fermi's goals was to be able to predict the momentum and energy distributions for specific β-decays and have these agree with actual experimental results. Using the relationships established in Eqs. 1.1 through 1.6, and others, Fermi was able to successfully predict the shape of β-decays by including three factors. These are (1) a statistical term which accounts for the number of final states accessible to the emitted particles; (2) a term which accounts for the influence of the nuclear Coulomb field; and (3) a term which includes the nuclear matrix element $|M_{fi}|^2$ to account for the overlap of initial and final nuclear states. The first and second terms can be combined into one term known as the *Fermi integral*, $f(Z, E_0)$, where Z is the atomic number of the daughter nucleus and E_0 is the

"state-specific" β-endpoint energy ($Q_\beta - E_x$); this integral can be calculated knowing the Z and E_0. Using a calculated quantity known as the *comparative half-life*, ft,

$$ft = \frac{f(Z, E_0)t_{1/2,(total)}}{BR} \tag{1.7}$$

experimentally determined values such as the total half-life (the actual half-life which is measured) and β-decay branching ratios (BR) can be used to indicate how well initial and final nuclear state wave functions overlap. Comparative half-lives (expressed in the units of seconds) allow us to put all β-decays on equal footing ("normalized" for the number of final accessible states and the nuclear Coulomb field), and therefore differences in ft values indicate differences in the matching of the initial and final nuclear states.

As an example, consider the β-decay of ^{15}B ($J^\pi = \frac{3}{2}^-$ [Aj91]) to the 3.103 MeV, $\frac{1}{2}^-$ state in ^{15}C (this is the lowest energy negative parity state in ^{15}C). In the present work, a total half-life of 10.3 ms was measured for ^{15}B, as was a 62.8% decay branch to the 3.103 MeV state. Using the method of Wilkinson and Macefield [Wi74] to calculate the Fermi integral, and taking the *maximum* β-endpoint energy, Q_β, to be 19.1 MeV [Aj91], the comparative half-life is determined as follows:

$$ft = \frac{f(Z = 6, E_0 = 16MeV) \bullet 0.0103\ s}{0.628} = 21,878\ s \tag{1.8}$$

Typically, the log of the ft values are reported, so for the above example the $logft$ value is 4.34. The $logft$ value can be related to the order of forbiddeness of a decay; Figure 1.1 summarizes experimental $logft$ values for many different decays. It is clear from this figure that there is a correlation between the $logft$ value and the order of forbiddeness. Each additional degree of forbiddeness increases the $logft$ value by approximately 3.5, representing a reduction in the transition probability of about 3×10^{-4}. Most allowed decays have $logft$ values in the range of 3.5 to 6.5, and first-forbidden decays have values in the range of 6.5 to 9.0. Second-forbidden decays have

$log ft$ values in the range of 10 to 13, third-forbidden decays 14 to 20, and fourth-forbidden decays have $log ft$ values of near 23. The utility of $log ft$ values lies in their predictive ability. For example, given the β-decay of ^{15}B, if a $log ft$ value of 5.4 was deduced for the decay to an unknown state in ^{15}C, it would be reasonable to assume that this was an allowed decay, and the ^{15}C state's J^{π} would be limited to $\frac{1}{2}^{-}$, $\frac{3}{2}^{-}$, or $\frac{5}{2}^{-}$, since the J^{π} of ^{15}B is $\frac{3}{2}^{-}$.

Now, with some of the basics of β-decay having been reviewed, the neutron-rich boron isotopes will be discussed next.

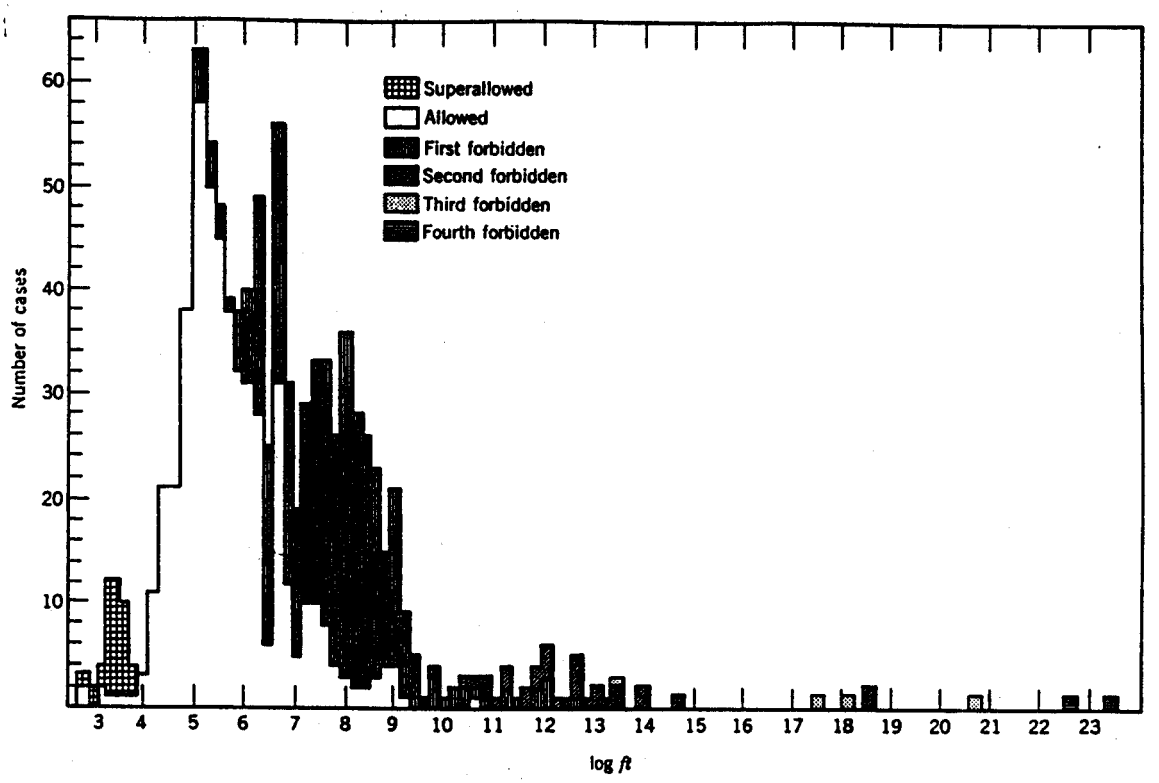

Figure 1.1: Experimental $logft$ values and associated types of β-decays. From K. Krane, *Introductory Nuclear Physics* (New York: John Wiley and Sons, 1988).

1.2 ^{15}B and the Other Neutron-Rich Boron Isotopes

The stable boron isotopes include ^{10}B and ^{11}B (20% and 80% atom percent abundance, respectively). Although it may be proper to refer to any boron isotope with mass greater than eleven as being "neutron-rich", in the present work the neutron-rich boron isotopes will be taken to be those with a mass of fifteen or more. Such neutron-rich boron isotopes have been studied over a long period of time, and they are particularly interesting in that the ratio of neutrons to protons is very large, being in the range of two to almost three. ^{15}B was first observed to be stable against prompt particle emission in 1966 [Po66]. In 1974 the particle stability of ^{17}B and the particle instability of ^{16}B were shown [Bo74]. Recently, in 1984, ^{19}B was shown to be the most neutron-rich stable boron isotope; in that same experiment ^{18}B was shown to be unstable to prompt neutron emission [Mu84]. Thus progress in establishing the limits of particle stability for the neutron-rich boron isotopes has been quite good. Suprisingly though, up till now nearly twenty-five years after it was first observed to be particle stable, much remains unknown about the decay of ^{15}B.

The half-life of ^{15}B has been measured by a number of different research groups most of which are in good agreement. Table 1.1 gives a summary of these half-life measurements. If the particularly low value of 8.8 ms observed by Curtin *et al.* [Cu86] is excluded, the weighted average obtained from the remaining half-life measurements is 10.3±0.2 ms. The value of 10.5±0.3 ms for the ^{15}B half-life has been adopted by Ajzenberg-Selove [Aj91].

However, not much is known about the β-delayed neutron decay of ^{15}B, other than that it is dominated mostly by single β-delayed neutron emission. In 1984 Dufour *et al.* [Du84] established the limits of $P_{0n} < 5\%$ and $P_{2n} < 1.5\%$ for ^{15}B decay (implying

therefore $P_{1n} > 93.5\%$), and more recently Reeder *et al.* observed $P_{1n} > 77.3\%$ and $P_{2n} = 0.4 \pm 0.2\%$ [Re91, Re90]. However, no measurement of the β-delayed neutron energies has been made, hence the β-decay branching ratios of ^{15}B to states in ^{15}C is not known. Referring to Figure 1.2 (the energy level scheme for ^{15}C), the ^{15}B β-decays that populate the ground state (E_x = 0.00 MeV, $J^\pi = \frac{1}{2}^+$) and first excited state (E_x = 0.74 MeV, $J^\pi = \frac{5}{2}^+$) of ^{15}C would be (1) particle bound due to the 1.218 MeV neutron separation energy, and (2) first-forbidden decays due to the positive parity of these states. The observed low P_{0n} is consistent with the fact that these are first-forbidden decays. Decays to the low-level, negative parity states in ^{15}C would be allowed (due to the spins and negative parity of these states) and additionally favored by the large phase space available; since these states have energies above the 1.218 MeV neutron separation energy (neutron emission via the ground state of ^{14}C), neutrons with kinetic energies in the range of 1.8 to 5 MeV will be emitted as a result of their feeding — this is consistent with the observed large P_{1n}. If the higher level states in ^{15}C are populated by the β-decay, it is possible they can decay by emitting one neutron via the first excited state of ^{14}C (^{15}C level must be at least 7.31 MeV) or even decay by emitting two neutrons via the ground state of ^{13}C (^{15}C level must be at least 9.39 MeV). It would be expected though that decays occurring via these two channels would be severely restricted due to the smaller amount of available phase space and this is partially supported by the observed low P_{2n}.

The importance of establishing the ^{15}B β-decay branching ratios to test the validity of shell-model calculations for nuclei far from stability was pointed out in the first section of this chapter. It should also be noted that ^{15}B has been used as a calibration standard for other β-delayed neutron experiments, and that such calibrations depend on the assumed neutron energy distribution [Mu88, Le89]. A measurement of the neutron energy spectrum for ^{15}B is important for establishing the utility of

^{15}B as such a standard. Lastly, the decay study of ^{15}B in the present work was partially undertaken as the "ground breaking" in the technical development of the hardware which would hopefully be used in the future studies of many other, more exotic, β-delayed neutron emitting nuclei at the NSCL using the newly designed and constructed neutron detector array.

Table 1.1: Summary of the half-life measurements made for the decay of ^{15}B. Listed is the reasercher and date the measurement was published, the reaction used to produce the ^{15}B, and the reported ^{15}B half-life.

Researcher (year)	Reaction	Half-life (ms)
Dufour *et al.* [Du84] (1984)	^{18}O fragmentation	11±1
Curtin *et al.* [Cu86] (1986)	^{18}O fragmentation	8.8±0.6
Mueller *et al.* [Mu88] (1988)	^{86}Kr fragmentation	10.4±0.3
Samuel *et al.* [Sa88] (1988)	^{22}Ne fragmentation	10.8±0.5
Lewitowicz *et al.* [Le89] (1989)	^{48}Ca fragmentation	10.3±0.6
Reeder *et al.* [Re91] (1991)	proton spallation	10.1±0.2

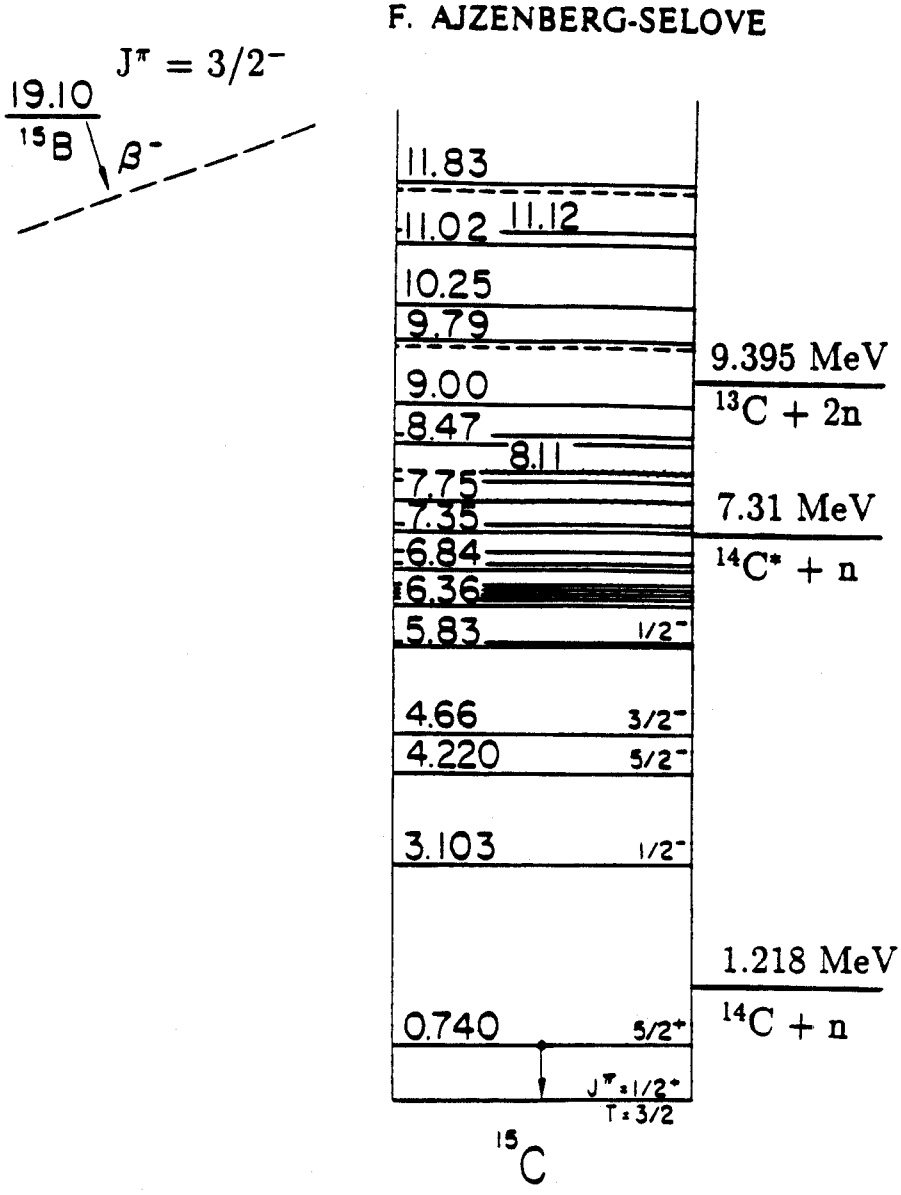

Figure 1.2: Energy level scheme of ^{15}C. From F. Ajzenberg-Selove, Nucl. Phys. **A523**, 1 (1991).

Chapter 2

Experimental Details

This chapter describes the experimental details involved with measuring the decay of ^{15}B. The information provided, however, could also be used as a guide in the future decay studies of other neutron-rich exotic nuclei using the NSCL neutron detector array. The production and separation of ^{15}B using the NSCL A1200 radioactive beam facility is briefly described, along with the transportation of the ^{15}B secondary beam to a low background experimental vault. The recently constructed neutron detector array, a device designed for the study of β-delayed neutron emitting nuclei, is introduced and its performance and specifications are described in detail. The method used to determine the neutron efficiency of the array is also outlined. Lastly, because it is necessary for decay studies to pulse the primary cyclotron beam on and off, the different cycles employed in this experiment, and the technique used, are described.

2.1 The NSCL A1200 Radioactive Beam Facility

The ^{15}B nuclei observed in this work were produced at the National Superconducting Cyclotron Laboratory at Michigan State University with an E/A = 80 MeV $^{18}O^{6+}$ beam, with an intensity of 12 pnA, from the K1200 cyclotron. A ^{9}Be tar-

get, 790 mg/cm^2 thick, was used and the reaction products were separated using the momentum-loss achromat mode of the A1200. A limited description of the A1200 separator is presented below and a full description of the device has been provided by Sherrill *et al.* [Sh91]

A schematic view of the A1200 radioactive beam facility is shown in Figure 2.1. The device consists of a series of fourteen superconducting quadrupole and four superconducting dipole magnets. It can be operated as a fragment separator with an angular acceptance of 0.8 msr, a 3% momentum acceptance, and a maximum rigidity of 5.4 Tm. The ^{9}Be target was placed at the "object" position of Figure 2.1 and heavy-ion reaction products resulting from the projectile fragmentation of the ^{18}O beam moved in the forward direction with essentially the beam velocity. Initial selection of reaction products with a specific m/q is accomplished with the first two dipole magnets; in the present experiment the dipole magnets were tuned (3.535 Tm) for an m/q = 3. Reaction products having a different m/q are filtered out or *dumped* at these first two dipole magnets. For example, the primary ^{18}O beam with an m/q of 2.25, after passing through the Be target ($^{18}O^{8+}$), was dumped on a catcher bar inside the first dipole magnet and did not continue forward through the remainder of the A1200 device.

A thin (7.84 mg/cm^2) plastic scintillation detector, placed at Image # 1 of Figure 2.1, was used to make a time-of-flight measurement of reaction products. The forward moving reaction products with the same m/q then travel through an achromatic wedge placed at Image # 2. The wedge introduces a Z dependent momentum shift due to the Z and velocity dependent energy-loss in the wedge given for example by the Bethe formula:

$$-dE/dx \propto Z^2/v^2 \tag{2.1}$$

This momentum shift is converted into a physical separation of the isotopes at the

final image of the A1200 by the last two dipole magnets. A wedge shaped degrader, as compared to a uniform thickness degrader (or flat degrader), results in the focussing of isotopes with the same Z and mass but different velocities at the A1200 final image; hence, maintains the achromaticity of the device. For this experiment, an aluminum wedge with a median thickness of 365 mg/cm^2 and an angle of 2.8 mrad was used. The last two dipole magnets were tuned (3.393 Tm) for $^{15}B^{5+}$ ions with the expected energy per nucleon of E/A = 59.8 MeV. Most of the reaction products with m/q = 3 and $Z < 5$ were dumped at the last two dipole magnets and did not reach the A1200 final image.

The A1200 provided a nearly pure (> 93%) beam of $^{15}B^{5+}$ ions at the its final image; impurities were $^{12}Be^{4+}$, $^{9}Li^{3+}$, $^{6}He^{2+}$ and $^{3}H^{1+}$ (described in more detail below). The ^{15}B secondary beam was then transported through a beamline to a low background experimental vault, some 60 meters away (including a total of 3 meters of concrete shielding) from the site of the primary ^{18}O reaction (see Figure 2.2), with an overall yield of approximately 600 particles per second.

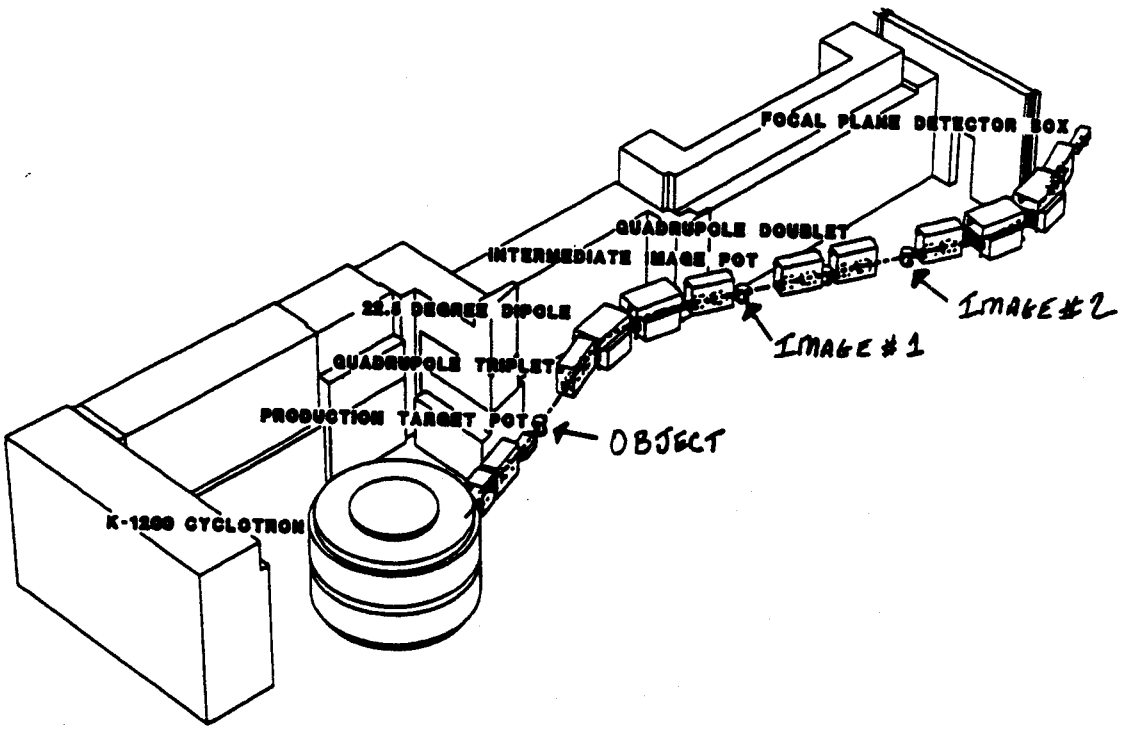

Figure 2.1: Schematic drawing of the NSCL A1200 radioactive beam facility and the K1200 cyclotron.

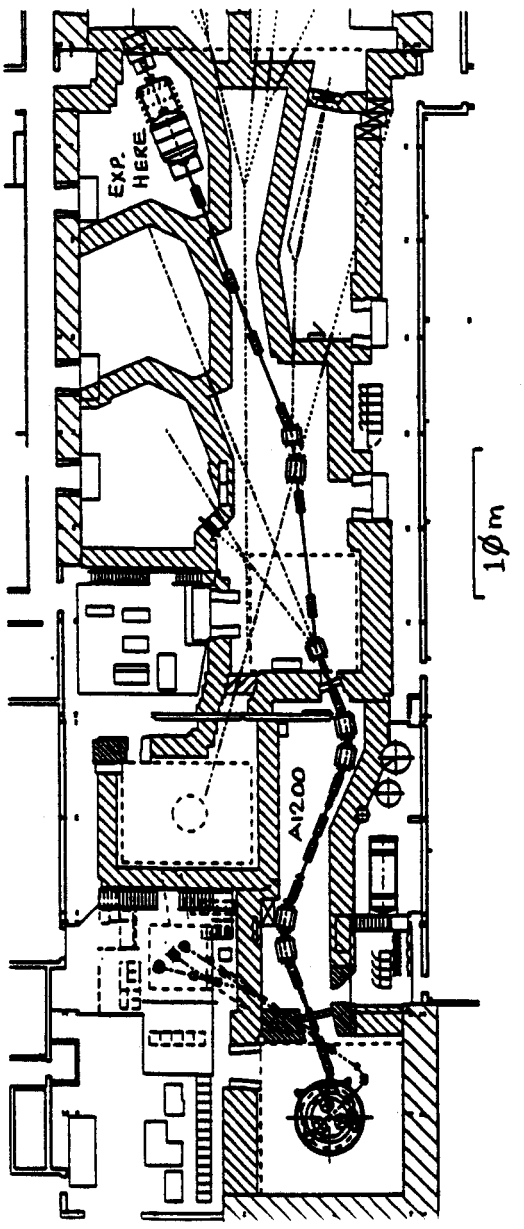

Figure 2.2: Schematic view of the NSCL experimental floor layout.The ^{15}B secondary beam was produced and separated at the A1200 and then transported to a low background experimental vault, some 60 meters away from the primary ^{18}O reaction.

2.2 The Neutron Detector Array

The ^{15}B ions were stopped in an active detector in the center of an array of neutron detectors. A schematic view of the NSCL neutron detector array is shown in Figure 2.3. The ^{15}B beam (E/A = 59.8 MeV) passed through a thin *kapton* window (0.25 mm thick) that separated the vacuum of the beamline from the air, approximately one meter of air, 6.8 mm of aluminum degrader (exiting with E/A $\approx$ 25 MeV), a silicon surface barrier ΔE detector (0.2 mm thick, 300 mm^2 area) and came to rest at a depth of 5.2$\pm$1.2 mm (the 1.2 mm is a limit, **not** 1σ) in a 10 mm thick plastic scintillator, referred to as the *implantation detector* (*BC412*, 2.0 cm by 2.5 cm by 1 cm deep). A close-up view of the detectors and associated hardware located at the center of the array is shown in Figure 2.4. The energy-loss of the ^{15}B ions in air and silicon, and the amount of aluminum degrader needed to stop the ions in the center of the implantation detector was determined using the NSCL program *INTENSITY* [Wi91]. This program uses the energy-loss parameters explicated by Hubert *et al.* [Hu90].

Energy loss in the ΔE detector, in addition to a time-of-flight measurement, allowed on-line monitoring of the purity of the ^{15}B secondary beam. The time-of-flight measurement was started by a signal from the start detector at Image # 1 of the A1200 (refer to Figure 2.1) and stopped by a signal from the ΔE detector at the center of the neutron detector array (refer to Figure 2.3). This arrangement also allowed us to determine the exact number of ^{15}B ions deposited in the implantation detector. A thick silicon surface barrier veto detector (1 mm thick, 300 mm^2 area) was placed behind the implantation detector in order to verify that the ^{15}B ions were indeed stopped in the plastic material. Figure 2.5 shows the energy spectra obtained from the ΔE detector and the veto detector for the implantation of the ^{15}B sec-

ondary beam. The ions and their relative percentages that entered the ΔE detector were $^{3}H^{1+}$ (2.7%), $^{6}He^{2+}$ (1.7%), $^{9}Li^{3+}$ (1.3%), $^{12}Be^{4+}$ (0.8%), and $^{15}B^{5+}$ (93.5%). By comparing the number of ions that entered the ΔE detector to the number that entered the veto detector, the relative percentages of ions that actually stopped in the implantation detector were $^{3}H^{1+}$ (0.17%), $^{6}He^{2+}$ (0.56%), $^{9}Li^{3+}$ (0.83%), $^{12}Be^{4+}$ (0.62%), and $^{15}B^{5+}$ (97.8%). Notice that, most of the ^{3}H passed through the implantation detector and all the ^{15}B stopped in it. The purity of the A1200 secondary beam for this experiment is summarized in Table 2.1.

As indicated in Figure 2.3, the implantation detector was partially surrounded by sixteen large rectangular (157 cm by 7.6 cm by 2.54 cm thick, each) *BC412* plastic neutron detectors bent in a one meter radius of curvature. The gap between adjacent neutron detectors had an area of approximately 800 cm^2. Neutrons leaving the central implantation detector and interacting with any part of any one of the sixteen neutron detectors would have a uniform flight path of one meter. The sixteen detectors covered a total solid angle of approximately 1.9 steradians.

The production rate of ^{15}B was sufficiently high that the cyclotron beam was cycled on and off, discussed below, and neutrons were observed during the beam-off period. The β-decay of the ^{15}B was detected by two photomultiplier tubes (1.9 cm diameter, *HAMAMATSU H3167*) attached to the implantation detector. The calculated mean-time of these signals served as the start for the neutron time-of-flight measurement. Each neutron detector also had two photomultiplier tubes (7.6 cm diameter, *THORN EMI 9821B*) and the mean-time served as a neutron time-of-flight stop.

Figure 2.6 is a schematic diagram of the electronic setup used for the ^{15}B decay experiment. The electronic modules used for the secondary beam purity time-of-flight measurement are shown (beam On period), as are the electronic modules used for

the β-delayed neutron time-of-flight measurement (beam Off period). The electronic modules needed to pulse the primary cyclotron beam on and off, in addition to those necessary for obtaining a half-life measurement during the beam Off period, are shown and details concerning their use are described later in this chapter. (This setup could remain essentially the same for other β-delayed neutron decay experiments).

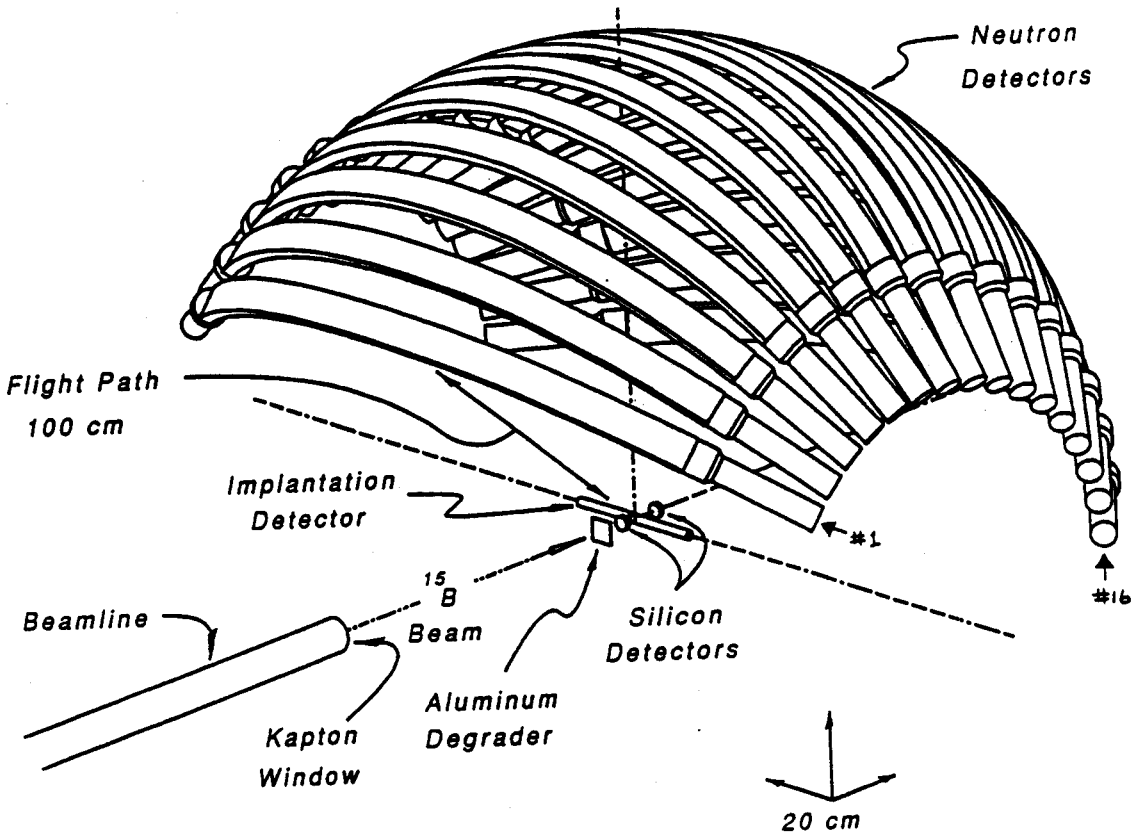

Figure 2.3: Schematic drawing of the NSCL neutron detector array and the experimental setup. The numbering of each neutron detector is consecutive going from # 1 to # 16.

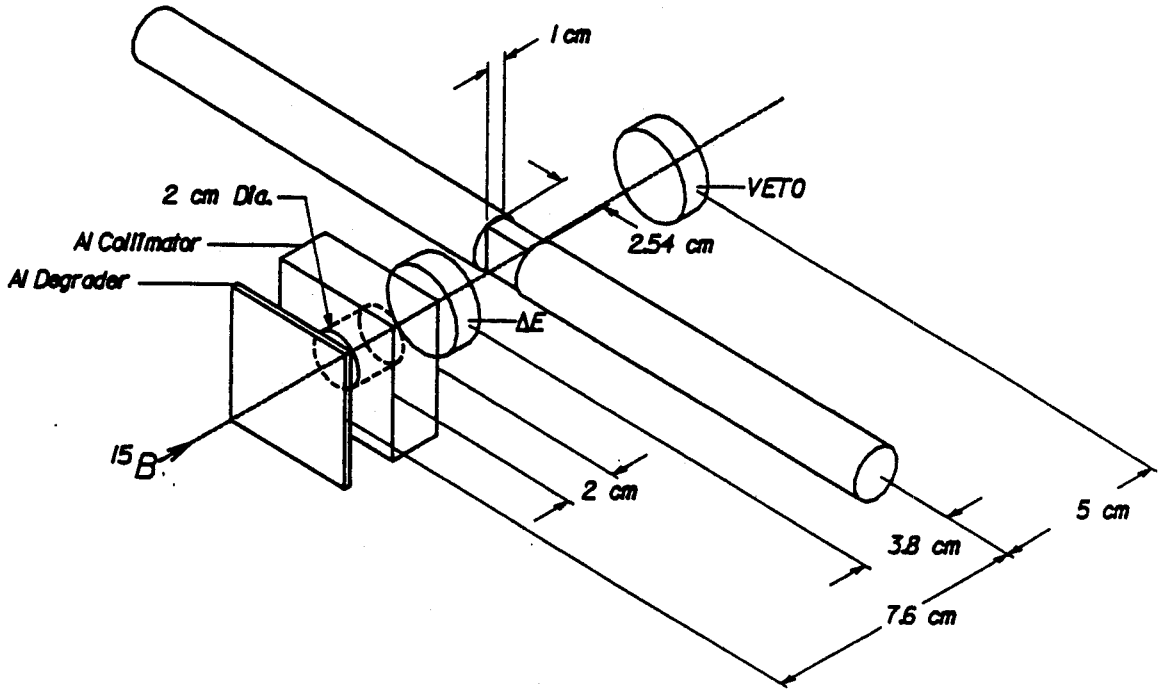

Figure 2.4: A close-up view of the detectors (implantation and the two silicon surface barrier) and associated hardware located at the center of the neutron detector array.

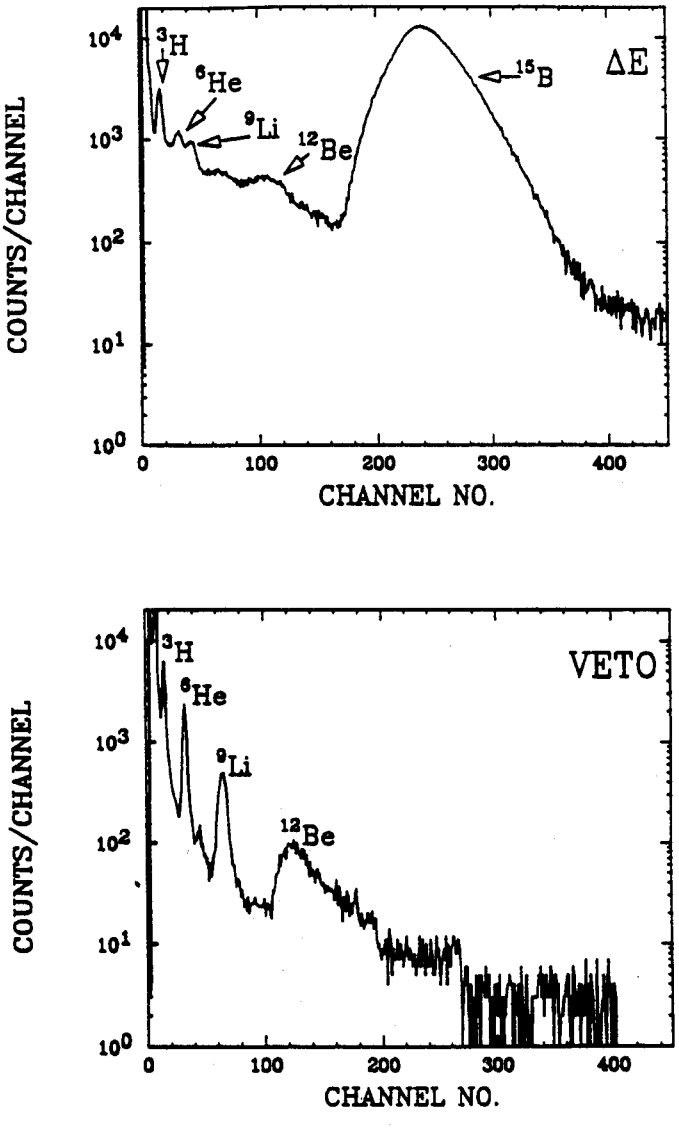

Figure 2.5: Energy spectra obtained from the ΔE detector and the veto detector (located at the center of the neutron detector array) for the implantation of the ^{15}B secondary beam.

Table 2.1: Summary of the A1200 beam purity for the implantation of the ^{15}B secondary beam.

- ^{15}B beam purity monitored by time-of-flight measurement (start from start detector at "Image 1" of A1200, stop from ΔE detector signal) and energy loss in ΔE detector.

- A1200 secondary beam purity from ΔE detector:
  - $^{3}H^{1+}$ 2.7%
  - $^{6}He^{2+}$ 1.7%
  - $^{9}Li^{3+}$ 1.3%
  - $^{12}Be^{4+}$ 0.8%
  - $^{15}B^{5+}$ 93.5%

- A1200 secondary beam purity that *actually* stopped in implantation detector (determined from ΔE and veto detectors):
  - $^{3}H^{1+}$ 0.17%
  - $^{6}He^{2+}$ 0.56%
  - $^{9}Li^{3+}$ 0.83%
  - $^{12}Be^{4+}$ 0.62%
  - $^{15}B^{5+}$ 97.8%

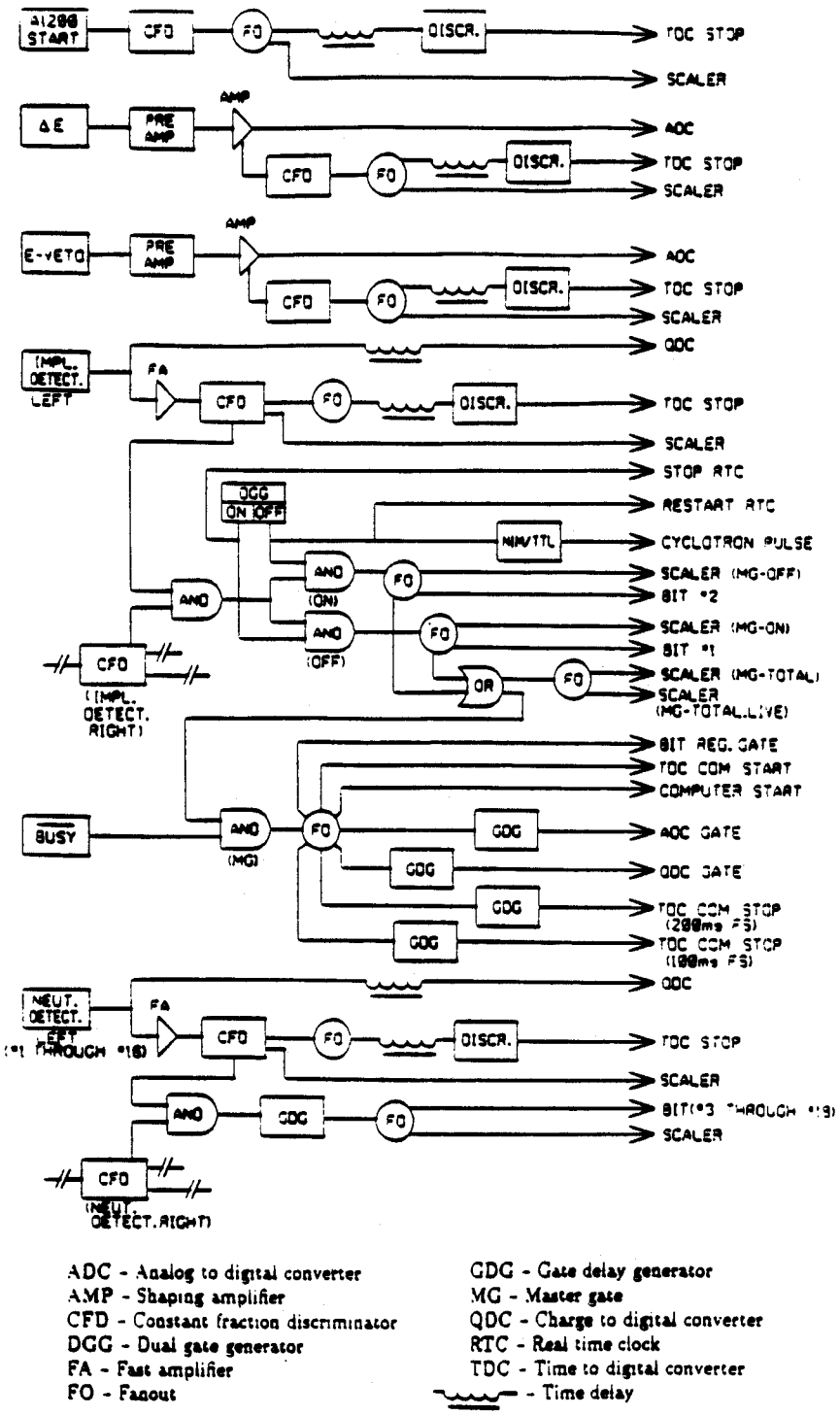

Figure 2.6: Schematic drawing of the electronic setup used in the ^{15}B decay study. This setup could remain essentially the same for other β-delayed neutron decay experiments.

2.3 Neutron detector efficiency

The neutron detection efficiency of the neutron detector array was determined as a function of threshold setting using a plutonium-beryllium source (PuBe source) positioned at the center of the detector array. In addition, a small liquid scintillation detector which will be referred to as the *standard detector* (*BC501*, 6.75 cm diameter by 3.60 cm deep), whose efficiency could be reliably determined to within 5% using a Monte-Carlo efficiency code [Ce79], was also placed a distance of one meter from the PuBe source to be used as a reference in our efficiency calibration. The PuBe source produces neutrons in coincidence with a 4.4 MeV γ-ray through the $^{9}Be(^{4}He,n)^{12}C^{*}$ reaction. The 4.4 MeV γ-ray produced in this reaction was detected in a 5 cm diameter by 10 cm deep BaF_2 detector and served as a time-of-flight start signal. The BaF_2 detector was used here because it had fast timing characteristics comparable to the implantation detector, but unlike the implantation detector, it also had superior stopping power to identify the full energy of the 4.4 MeV γ-ray.

Neutron time-of-flight spectra were obtained for each of the sixteen array detectors in addition to the standard detector (here the standard detector had a neutron threshold set at 0.2 MeV electron-equivalent energy). Figure 2.7 shows the time-of-flight spectrum obtained for one of the array detectors (each of the other fifteen were very similar) and the time-of-flight spectrum obtained for the standard detector. The "fast" γ-ray peak seen in each spectrum established "time-zero"; this peak is due to the PuBe source producing γ-rays (in addition to neutrons) in coincidence with the 4.4 MeV γ-ray. The peak labeled "cosmic" resulted from cosmic particles passing through a neutron detector first and then passing through the implantation detector and triggering the master gate of the data acquisition system; a peak appeared in this same channel location of the time-of-flight spectra when a γ-ray source was placed

on the outer side of a neutron detector. The peak labeled "flag" was a diagnostic marker written into software to indicate when a neutron detector did not have an event occurring within a selected time window. Having an accurate time calibration of each spectrum (obtained by using an ORTEC model # 462 time calibrator) and a fixed flight path of one meter, neutron energy "bites" were obtained from each time-of-flight spectrum (the sixteen array detectors and the standard detector) for neutrons with kinetic energies in the likely energy range for the decay of ^{15}B (1.8, 2.8, 3.2, 4.3 and 4.8 MeV; this deduced from the known states in ^{15}C and the neutron separation energy of ^{14}C [Aj91], and shell-model predictions [Cu86]).

For 1.8 MeV neutrons, an energy bin (bin # 1) of 1.6 MeV to 2.0 MeV was selected; the calculated Monte-Carlo neutron detection efficiency for the standard detector was 17.6% for 1.60 MeV neutrons and 22.9% for 2.0 MeV neutrons (hence, an average efficiency of 20.3% for this energy bin). For 2.8 MeV and 3.2 MeV neutrons, an energy bin (bin # 2) of 2.4 MeV to 3.4 MeV was selected; the calculated Monte-Carlo neutron detection efficiency for the standard detector was 24.0% for 2.4 MeV neutrons and 23.9% for 3.4 MeV neutrons (hence, an average efficiency of 23.95% for this energy bin). Lastly, for 4.3 MeV and 4.8 MeV neutrons, an energy bin (bin # 3) of 4.0 MeV to 5.0 MeV was selected; the calculated Monte-Carlo neutron detection efficiency for the standard detector was 22.9% for 4.0 MeV neutrons and 21.9% for 5.0 MeV neutrons (hence, an average efficiency of 22.4% for this energy bin). Figure 2.8 shows these three energy bins for the PuBe time-of-flight spectra.

The efficiency of each array detector was then determined by (1) taking the ratio of number of neutrons detected in an array detector and the standard detector as a function of energy (number of neutrons in the specific energy bin), (2) normalizing for the solid angle of the array detector (119.5 msr) and the standard detector (3.585 msr), and (3) normalizing according to the calculated Monte-Carlo neutron

detection efficiency for the standard detector for the specific energy bin (using the average efficiency specified in the previous paragraph). For purpose of example, the neutron detection efficiency of array detector # 1 for 1.8 MeV neutrons was determined as follows:

$$\epsilon = \frac{7735}{209} \times \frac{3.858}{119.5} \times 0.203 \times 100 = 22.5\% \tag{2.2}$$

The estimated error associated with this measured efficiency accounted for the number of neutrons available for the measurement, the 5% uncertainty in the Monte-Carlo calculation, and an additional term to account for uncertainties related to the PuBe energy bin (this estimated to be 5% for bin # 1, 1% for bin # 2, and 2% for bin #3), and was determined as follows (for bin # 1, det # 1):

$$\frac{\delta\epsilon}{\epsilon} = \sqrt{(\frac{\sqrt{209}}{209})^2 + (\frac{\sqrt{7735}}{7735})^2 + (0.05)^2 + (0.05)^2} = 0.100 \tag{2.3}$$

As such, array detector # 1 had a detection efficiency of 22.5±2.25% for 1.8 MeV neutrons. Table 2.2 summarizes the neutron detection efficiency measurements for the sixteen array detectors; included is the estimated error associated with each measurement in addition to the mean and standard deviation of the efficiency measurements.

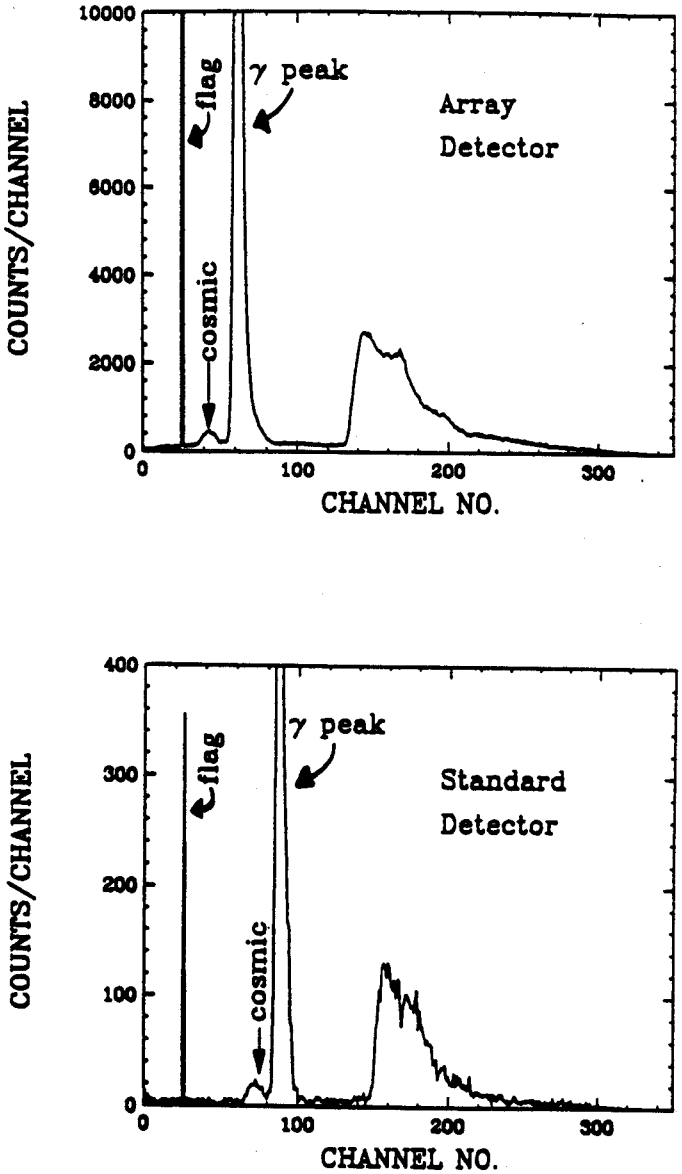

Figure 2.7: Time-of-flight spectra obtained from an array detector and the small, standard detector using the PuBe neutron source. These spectra were used, in part, in determining the neutron detector array neutron detection efficiency. The peaks labeled "flag" and "cosmic" are explained in the text.

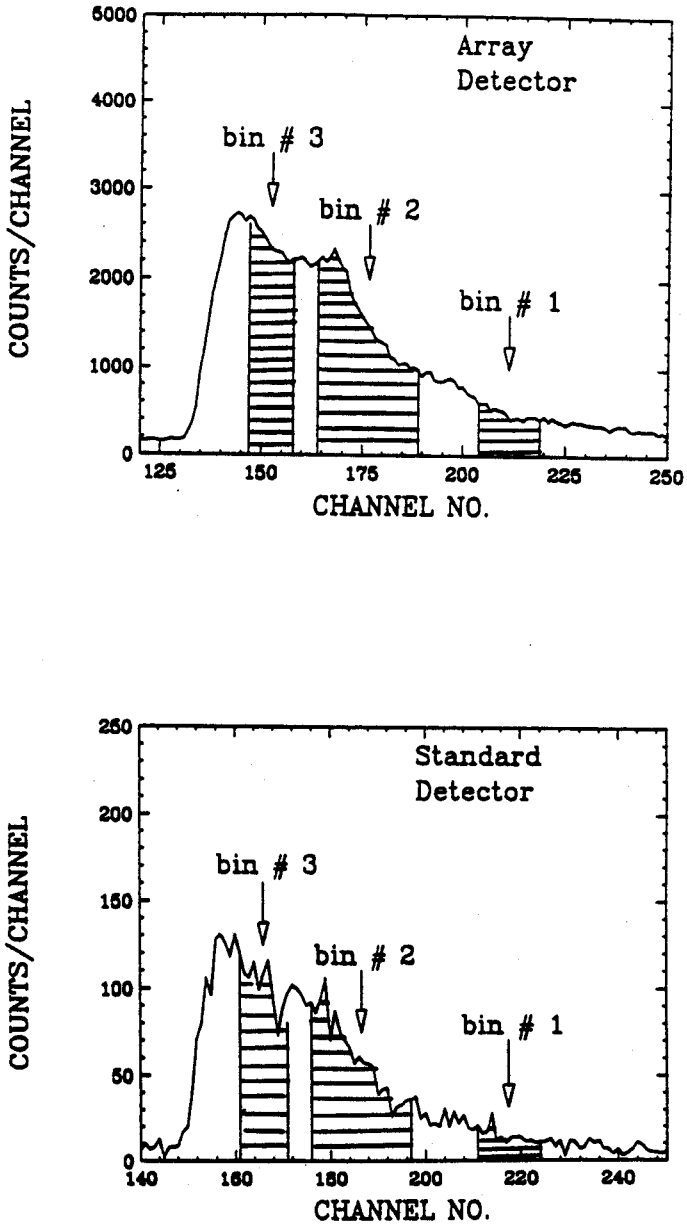

Figure 2.8: Energy "bins" selected from the PuBe neutron source time-of-flight spectra.

Table 2.2: Summary of the measured neutron detection efficiencies (using the PuBe source) for the sixteen array detectors. Listed are the measured efficiencies, including the estimated error associated with each measurement, for the detection of 1.8 MeV, 3.0 MeV and 4.5 MeV neutrons. Also included is the mean and standard deviation of the sixteen measurements for the three energy bins.

Detector	1.8 MeV	3.0 MeV	4.5 MeV
# 1	22.5±2.25%	21.8±1.27%	18.0±1.11%
# 2	20.7±2.07%	20.6±1.20%	17.5±1.08%
# 3	23.3±2.33%	21.8±1.27%	17.8±1.10%
# 4	23.2±2.32%	22.4±1.30%	17.0±1.05%
# 5	21.7±2.17%	21.4±1.24%	16.6±1.03%
# 6	22.5±2.25%	22.4±1.30%	17.1±1.06%
# 7	22.3±2.23%	22.1±1.28%	17.4±1.08%
# 8	21.7±2.17%	21.3±1.24%	17.6±1.09%
# 9	21.9±2.19%	22.7±1.32%	17.9±1.11%
# 10	21.0±2.10%	24.0±1.40%	17.1±1.06%
# 11	22.0±2.20%	21.7±1.26%	17.9±1.11%
# 12	20.7±2.07%	21.2±1.23%	17.1±1.06%
# 13	22.3±2.23%	22.0±1.28%	17.4±1.08%
# 14	23.4±2.34%	22.3±1.30%	15.9±0.98%
# 15	24.0±2.40%	22.1±1.29%	17.4±1.08%
# 16	23.2±2.32%	21.8±1.27%	15.6±0.96%
$\overline{x}_{eff}$	22.3	22.0	17.2
σ_{eff}	1.02	0.78	0.71

2.4 Comparison of the Measured (PuBe) Efficiency to a Monte-Carlo Calculated Efficiency for an Array Detector

The measured neutron detection efficiency of an array detector (det # 1), which was obtained using the PuBe source, was compared to a Monte-Carlo [Ce79] calculated efficiency. The neutron detection efficiency of a detector is a strong function of the detector's threshold setting. Typically, the threshold setting of a neutron detector is determined using γ-ray sources which, in their interaction with the scintillation material, produce Compton edges of specific energies. For example, a Compton edge obtained using a ^{60}Co source (which yields a Compton edge of approximately 1.0 MeV) with the standard detector used in the PuBe efficiency measurement appeared at channel 103 of the detector's pulse height (energy) spectrum[1]. Using a ^{134}Cs source (which produces two Compton edges, one at 0.42 MeV and one at 0.61 MeV) two Compton edges appeared in the pulse height spectrum at channel 42 and channel 60. These are shown in Figure 2.9. A threshold set at channel 20 of the detector's pulse height spectrum, therefore, would correspond to a 0.2 MeV electron-equivalent neutron energy threshold (equivalent to approximately a 1.0 MeV neutron energy cut-off).

For an array detector, establishing the known threshold setting was more complicated because the pulse height channel a Compton edge appeared at was dependent on the location along the detector a γ-ray source was placed (varying distances from the right and left photomultiplier tubes). Figure 2.10 shows the five positions a collimated ^{60}Co source was placed at in order to determine the detector's threshold setting and its dependence on position. Figure 2.11 shows the Compton edges obtained from

[1]The position of half-height was used to denote the Compton edge of all appropriate measurements in this work.

the left and right sides of array detector # 1 for these five positions.

Referring to the electronics diagram (Figure 2.6), a logical "and" was required between the left and right sides of an array detector for an event to be valid. For this reason, the validity of an event occurring on the left half of the detector would be determined by the signal detected in the right photomultiplier tube and its associated threshold setting (since, for such an event, the right signal is smaller then the left signal and hence the limiting factor), while the validity of an event occurring on the right half of the detector would be determined by the detector's left side. Referring to Figure 2.11 and observing the Compton edge obtained from the detector's right side for positions # 1, 2 and 3 in addition to observing the Compton edge obtained from the detector's left side for positions # 3, 4 and 5, an *average* threshold of 0.12 MeV electron-equivalent energy was estimated (equivalent to approximately a 0.8 MeV neutron energy cut-off). A Monte-Carlo efficiency calculation [Ce79] was performed for array detector # 1 using the 0.12 MeV electron-equivalent threshold setting. The results of the measured (PuBe) and Monte-Carlo calculated efficiencies are shown in Table 2.3 (not including solid angle). The overall agreement is quite good.

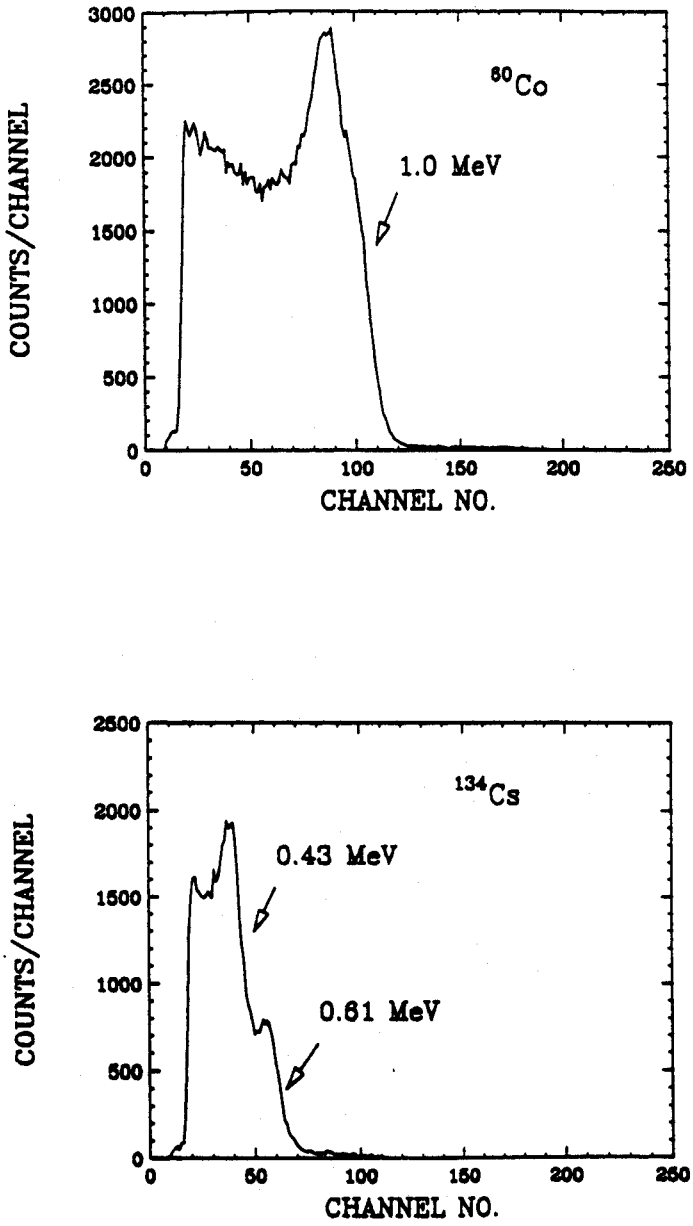

Figure 2.9: Compton edges obtained in the pulse height spectrum of the standard detector using ^{60}Co and ^{134}Cs γ-ray sources. Note that the location of the Compton edge was taken to be the half-height of the edge.

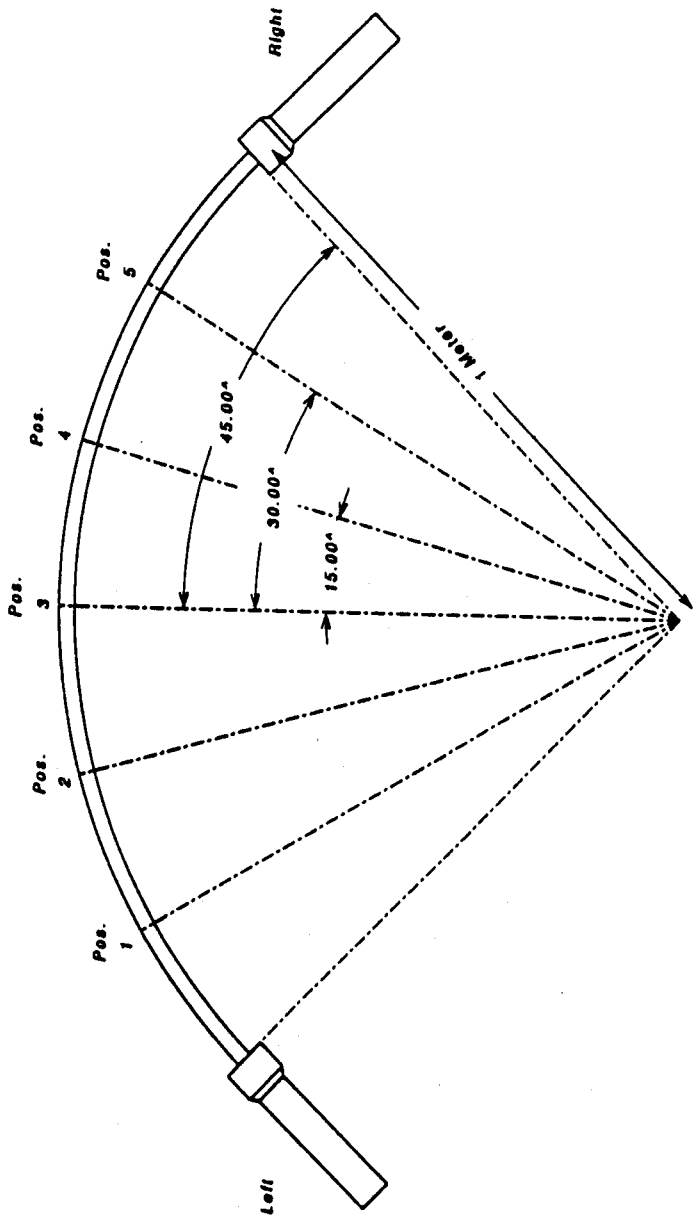

Figure 2.10: Array detector showing the five positions a ^{60}Co source was placed in order to determine the detector's neutron threshold setting and its dependence on position. The source was collimated and placed flush against the detector.

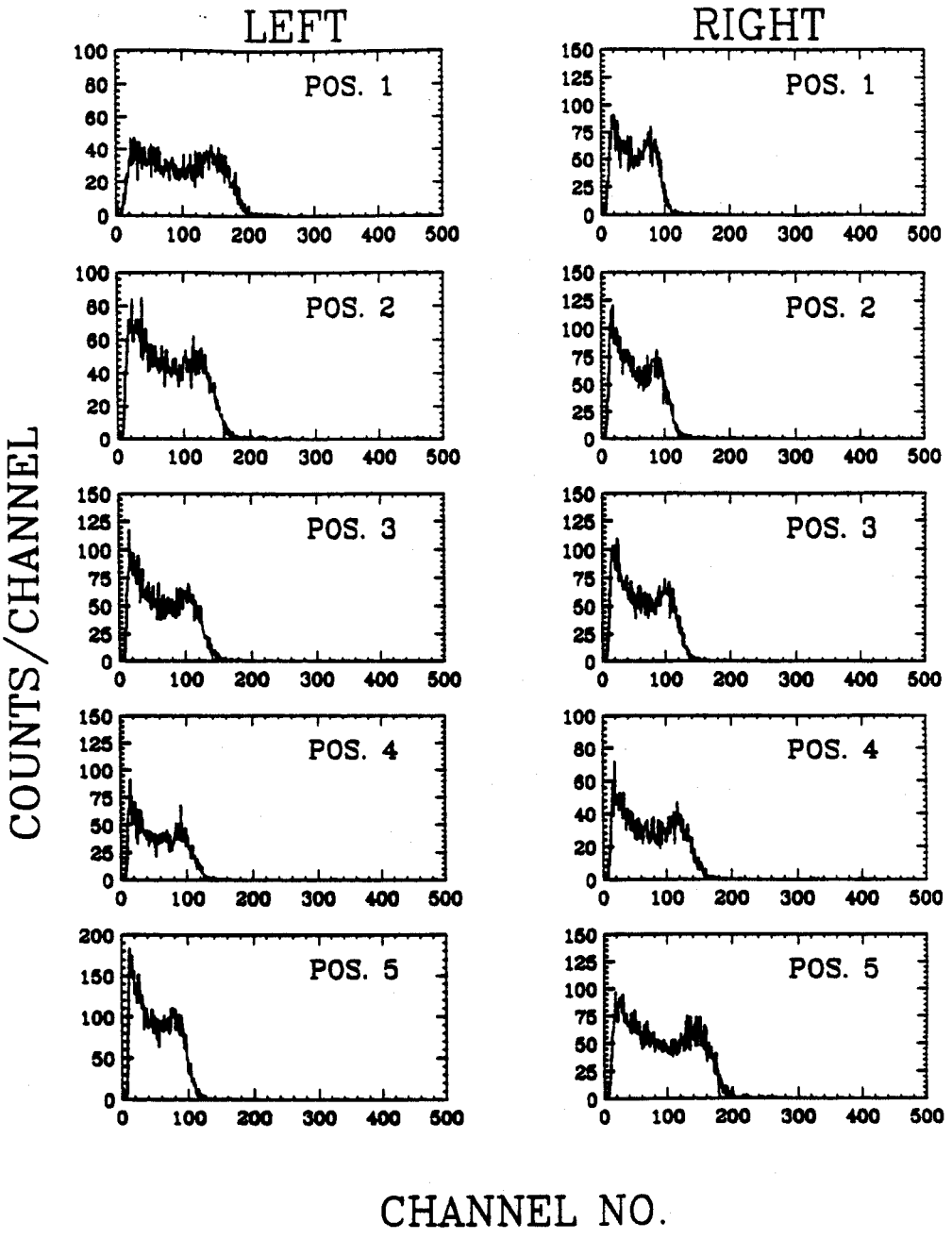

Figure 2.11: Compton edges obtained, using a ^{60}Co source, from the left and right sides of array detector # 1 for the five positions shown in Figure 2.10.

Table 2.3: Comparison of measured (PuBe) and calculated (Monte-Carlo) efficiencies for neutron array detector # 1 as a function of neutron energy (not including solid angle).

Energy (MeV)	Measured (PuBe)	Calculated (Monte-Carlo)
1.8	22.5±2.25%	22.0%
3.0	21.8±1.27%	20.8%
4.5	18.0±1.11%	18.8%

2.5 Exploring Position Sensitivity with the Neutron Detector Array

While a technique which would identify and confine a neutron interaction to a specific location on an individual array detector was not needed for the ^{15}B decay experiment (since the neutrons were emitted isotropically from the implantation detector), the ability to achieve position sensitivity with individual array detectors was explored. It is already possible to determine events occurring in different array detectors simultaneously; for example, in the ^{15}B experiment it would have been possible to identify that events had occurred in detectors # 1, 4 and 14, or any combination, from a single decay. Going a step further and being able to associate an event with a specific sector of a single detector could expand the usefulness of the neutron detector array in angular correlation experiments.

To determine if position sensitivity was possible with an array detector, a collimated ^{60}Co source was placed at positions one through five of an array detector (refer to Figure 2.10). Two techniques were then investigated. One technique used the pulse height (energy) signal measured at each end of the detector, the other technique used the timing signal measured at each detector end.

The technique using pulse height signals to determine position is based on the principle of light attenuation through the plastic. When the ^{60}Co source is placed at array detector position # 3 (center), the pulse height measured from the left and right sides of the detector should be the same; this of course if the two sides are gain matched. When the source is placed at position # 1, the pulse height measured at the detector's left side is larger than that measured at its right side. Simply, the more plastic the light must travel through before reaching a photomultiplier tube, the more the light is attenuated, hence the smaller its measured pulse height signal. Two

functions were used to obtain position information from pulse height measurements. The first assumed linear attenuation of light through the plastic scintillator:

$$POS_{linear} = offset + slope \times \frac{L_{pulseheight}}{L_{pulseheight} + R_{pulseheight}} \tag{2.4}$$

The second assumed exponential attenuation of light through the plastic:

$$POS_{exponential} = offset + slope \times ln(\frac{L_{pulseheight}}{R_{pulseheight}}) \tag{2.5}$$

The technique using timing signals to determine position information is based on the fact that light traveling through the plastic scintillator travels at a finite and measurable velocity (roughly 15 cm/ns). When the ^{60}Co source is placed at position # 3 (center) of the array detector, light reaches the left and right photomultiplier tubes at nearly the same time, about 5.2 ns after being created. When the ^{60}Co source is placed at position # 1, light will reach the left photomultiplier tube in about 1.7 ns, while it will take about 8.7 ns to reach the right tube. The function used to obtain position information from the timing signals was:

$$POS_{timing} = offset + slope \times \frac{R_{time} - L_{time}}{R_{time} + L_{time}} \tag{2.6}$$

The method employing pulse height signals supplied position sensitivity with a resolution of approximately 25 cm (FWHM) using the linear function and approximately 20 cm (FWHM) using the exponential function. The method employing timing signals proved superior, supplying position sensitivity with a resolution of approximately 13 cm (FWHM). Figure 2.12 shows the results of placing the ^{60}Co source at the five detector locations and using the "position through timing" function (Equation 2.6); those shown in the figure are the results obtained with detector # 6.

By taking the centroid of the five position peaks shown in Figure 2.12 and their associated array positions in θ (-30 $^\circ$ for pos # 1, -15 $^\circ$ for pos # 2, 0 $^\circ$ for pos #

3, 15 ° for pos #4 and 30 ° for pos # 5), a linear function was generated that would identify an event to a detector position in θ. It should be noted that the position resolution of 13 cm corresponds to approximately 7 ° in θ.

Table 2.4 summarizes the specifications of the NSCL neutron detector array described throughout this chapter.

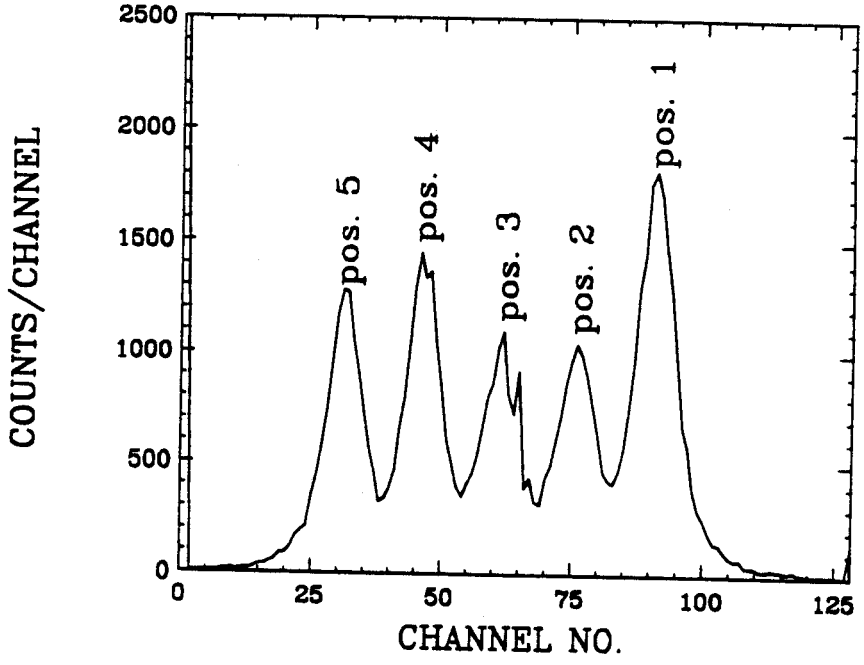

Figure 2.12: Results of placing a collimated ^{60}Co source at the five array detector locations shown in Figure 2.10 and using the "position through timing" function (Equation 2.6).

Table 2.4: Summary of the NSCL neutron detector array specifications.

1. Implantation detector constructed from *BC412* plastic scintillator (2 cm square by 1 cm deep) and *HAMAMATSU H3167* (1.9 cm diameter) photomultiplier tubes.

2. Neutron detectors constructed from *BC412* plastic scintillator and *THORN EMI 9821B* (7.6 cm diameter) photomultiplier tubes.

3. Sixteen individual neutron detector elements in total array.

4. Total array active area covers a solid angle of approximately 1.9 steradians.

5. Each neutron detector element (157 cm by 7.6 cm by 2.54 cm thick) has an active area which covers a solid angle of approximately 120 msr (0.076 rad in angle θ, 1.57 rad in angle ϕ).

6. Gap between adjacent detectors measures approximately 800 cm^2 or approximately 0.05 rad in angle θ (approximately 70% area of one detector element).

7. Neutron energy determined by time-of-flight method with flight path equal to 1 meter. Time-of-flight start from calculated meantime of implantation detector, time-of-flight stop from calculated meantime of neutron detector.

8. Total timing resolution of detectors determined by combination of electronics contribution (approximately 1 ns) and neutron-energy dependent time-uncertainty owing to a flight path uncertainty (for a *typical* detector, flight path uncertainty is approximately 4 cm). As such, total time resolution (FWHM) for detector is 2.4 ns for 1.8 MeV neutron, 1.9 ns for 3.2 MeV neutron, and 1.7 ns for 4.8 MeV neutron.

9. Position information (in angle θ) for each neutron detector determined by timing comparison of left vs. right side of detector ($\frac{T_R - T_L}{T_R + T_L}$). This results in a position resolution of approximately 13 cm (FWHM) or 7° in angle θ.

2.6 Cyclotron Beam On/Beam Off Cycles for Decay Studies

In order to study the decay of ^{15}B it was necessary to pulse the primary cyclotron beam on and off for fixed intervals of time. Since the production rate of ^{15}B was relatively high considering its 10.5 ms half-life (one ^{15}B ion produced per 1.9 ms), it was most efficient to pulse the beam at fixed intervals. In decay studies for very exotic species, the half-lives tend to be very short (large λ) and the times between implantation of these nuclei tend to be long (many times $1/\lambda$). In these cases, it is most efficient to shut off the primary beam after each arrival, and the decay of the single atom is observed; this technique is explained in detail by Mikolas [Mi89].

The pulsing of the primary beam was accomplished with a gate module that periodically sent a logic signal to a fast phase shifter in the rf transmitter of one of the "dees" of the K1200 cyclotron. The cyclotron beam was interrupted within approximately 40 μs [Mi89]. To measure the decay branches of ^{15}B to neutron-unbound states in ^{15}C a 50 ms On/50 ms Off cycle was used for part of the experiment and later changed to a 20 ms On/40 ms Off cycle. ^{15}B ions were deposited in the implantation detector during the beam on time and decays were monitored during the subsequent beam off time. A real time clock module started at the beginning of each beam off interval (zeroed at the beginning of each subsequent beam on interval) was used to measure the time of each event relative to the end of the beam on period. The total beam off period was easily measured with the real time clock. The beam on period was calibrated by recording events from a ^{60}Co γ-ray source positioned near the implantation detector (during these runs there was no cyclotron beam) for the different time cycles. By ratio of the number of γ-rays observed during the two periods and knowing the beam off time period exactly, the exact times of the cycles

turned out to be 49.23 ms On/49.80 ms Off and 20.33 ms On/39.55 ms Off. For purpose of example, the 50 ms/50 ms cycle was calculated in the following manner. In order to determine the exact time of the Off cycle, the last channel of the time spectrum from the real time clock was simply multiplied by the time per channel which was controlled by a crystal oscillator:

$$102ch. \times 0.4883\frac{ms}{ch.} = 49.80ms. \tag{2.7}$$

To determine the exact time of the On cycle, the exact time of the Off cycle was multiplied by the ratio of γ events recorded for the On/Off cycles:

$$49.80ms \times \frac{7129}{7212} = 49.23ms. \tag{2.8}$$

It should be noted that the computer dead time and sampling efficiency was the same for the On and Off cycle.

To determine the number of ^{15}B decays that led to bound states in ^{15}C ($t_{1/2}$ = 2.449±0.005 s, [Aj91]), the cyclotron beam cycle was later changed to 4.847 s On/5.719 s Off. Here, ^{15}B ions were deposited in the implantation detector during the beam on period and ^{15}C decays (β-emission) were counted during the beam off period.

To determine the efficiency of the implantation detector for ^{15}C β-particles, the A1200 was used to produce ^{15}C and ^{17}N and these ions were deposited in the implantation detector using a 4.762 s On/7.063 s Off cycle. The results of this implantation are discussed later.

Table 2.5 lists the measurements recorded in order to determine the exact times of the different time cycles.

Table 2.5: Beam On/beam Off ^{60}Co γ-ray source measurements used to calibrate exact times of On/Off cycles. Listed are the time cycles, number of γ events recorded during On/Off cycle, time calibration of real time clock, last channel of Off cycle time spectrum, and calculated exact times of beam On/beam Off cycles.

time cycle (On/Off)	γ events (On/Off)	time/channel	last channel (Off cycle)	exact time (On/Off)
50 ms/50 ms	7129/7212	0.4883 ms	102	49.23 ms/49.80 ms
20 ms/40 ms	8270/16088	0.4883 ms	81	20.33 ms/39.55 ms
5 s/6 s	7764/9161	0.03125 s	183	4.847 s/5.719 s
5 s/7 s	3165/4694	0.03125 s	226	4.762 s/7.063 s

Chapter 3

Results and Analysis

This chapter presents the experimental results and analysis involved with measuring the decay of ^{15}B. The opening section gives a summary of the different experimental runs used to accomplish this measurement. The information provided not only gives the reader a concise overview of the entire experiment, but it also contains valuable information about A1200 exotic nuclei production rates and systematics which can be helpful in other decay studies. In the second section, the ^{15}B half-life obtained from this work is compared to the published values of earlier studies. The third section presents the results of depositing ^{15}B ions into the implantation detector and observing the β-decay of ^{15}C to determine the ^{15}B β-decay branch to ^{15}C bound states. The fourth section concentrates on the ^{15}B β-decay branch to unbound states in ^{15}C, and includes the results of the ^{15}B β-delayed neutron time-of-flight measurements. In the final section the β-decay branching ratios of ^{15}B are presented and discussed.

3.1 A Summary of the Experimental Runs Made to Measure the Decay of ^{15}B

The experimental runs involved with the present work can be divided into three basic groups[1]. The runs in Group One involved the deposition of ^{15}B ions into the implantation detector during the beam on period and then monitoring their decays during the beam off period. These runs were used to obtain a half-life and β-delayed neutron time-of-flight measurements of ^{15}B; this group included runs (which will be referred to as) # 1, 2 and 3 (50 ms/50ms - on/off cycle) and runs # 4 through 10 (20 ms/40 ms - on/off cycle). The runs in Group Two involved the deposition of ^{15}B ions into the implantation detector during the beam on period and then monitoring ^{15}C decays during the beam off period in order to determine the ^{15}B β-decay branch to ^{15}C bound states; this group included runs # 11, 12 and 13 (5 s/6 s - on/off cycle). Lastly, a run in Group Three involved the deposition of ^{15}C and ^{17}N ions from the A1200 radioactive beam device into the implantation detector during the beam on period and then monitoring their decays during the beam off period. This run was used to determine the detector's β-decay detection efficiency for nuclei other than ^{15}B (specifically ^{15}C); this will be described in more detail below. The third group included run # 14 (5 s/7 s - on/off cycle).

3.1.1 Group One Experimental Runs

Two different beam on/beam off cycles were used for the Group One experimental runs, the 50 ms/50 ms and the 20 ms/40 ms. Although either cycle alone could have provided the half-life and β-delayed neutron time-of-flight measurements of ^{15}B, the 20/40 was found to be more efficient (described below). In addition, using the

[1]Note that these do not include the PuBe source efficiency runs or the short duty cycle runs used to determine the exact times of the beam on/off cycles.

different cycle times provided a test to see if similar results would be obtained under different conditions; for example, the implantation detector's β-detection efficiency. Table 3.1 provides a summary of specific quantities related to the Group One runs.

The total time of each run (to the nearest 0.01 s) was written to magnetic tape by the data acquisition program. The total number of ^{15}B ions deposited in the implantation detector for each run was determined event by event from the particle identification in the ΔE detector/time-of-flight measurement and then normalizing this measurement to account for the beam on computer dead time[2]. Once the actual number of implanted ^{15}B ions was known, the A1200 production rates were easily determined by using the total time of each run and the exact times of the beam on/off cycle (Table 2.5).

It should be noted that the A1200 ^{15}B production rates (ions per ms) for runs 1 through 10 were, overall, fairly uniform with a high of 0.647, a low of 0.418, the mean value was 0.532 with standard deviation of 0.081. This variation can be accounted for by variations of the K1200 cyclotron primary beam current.

For purposes of discussion, "beam on period" and "implantation period" can be considered synonymous, as can "end of the implantation period" and "beginning of the beam off period". The last column of values in Table 3.1 is the sum of the number of ^{15}B ions that existed at the end of each implantation period for the entire run. Consider the following example: it was determined (described below) that for run #1, 9.34 ^{15}B atoms were present in the implantation detector at the end of each implantation period. With a total of 32,445 implantation periods for run #1, the total number of ^{15}B atoms present at the end of all the implantation periods for run # 1 was 3.03E5; this is the number listed in Table 3.1. This number is smaller than

[2]The computer dead time was determined by the ratio of two scaler values that were read for all measurements every time an event occurred, one scaler value being read uninhibited and the other read only when the computer was not busy.

the number of ^{15}B ions implanted (third column in Table 3.1) because some of the ^{15}B atoms decayed while the implantation was still in progress. It is the number of atoms present at the end of the implantation period (when decays are able to be observed) that comprise the sample population from which decay-related observables, like half-life, are determined. Decays that occur while the implantation is still in progress contribute nothing to these determinations.

The number, N, of atoms present at any time, t, during the implantation period increases in proportion to the production rate, R, and decreases due to decay: $dN = Rdt - \lambda N dt$. This simple differential equation can be solved for N:

$$\frac{dN}{R - \lambda N} = dt$$

$$\int \frac{dN}{R - \lambda N} = \int dt$$

$$R - \lambda N = Ce^{-\lambda t}$$

$$N = \frac{R - Ce^{-\lambda t}}{\lambda}$$

Knowing that at time zero, N equals zero and at time infinity N equals R/λ gives:

$$N = \frac{R}{\lambda}(1 - e^{-\lambda t}) \tag{3.1}$$

This expression assumes that the rate of production, R, is constant throughout the run. If this rate fluctuates considerably during the run, the implantation should be divided into time intervals, t_i, during which time the rate, R_i, is steady and then N can be determined as a summation of many short runs. In the present work, the production rate during each run was assumed to be constant. The validity of this assumption will be shown later in the section on the implantation detector's β-detection efficiency.

The number of ^{15}B atoms that existed at the end of each implantation period, referred to as N_0 [3], is determined by knowing the A1200 production rate in ions per ms, $R_{^{15}B}$, the ^{15}B decay constant $\lambda_{^{15}B}$ = (6.60±0.07)E-2 ms^{-1} [Aj91], and the exact time of the implantation period, t_{on}:

$$N_0 = \frac{R_{^{15}B}}{\lambda_{^{15}B}}(1 - e^{-\lambda_{^{15}B} t_{on}}) \tag{3.2}$$

To account for ^{15}B atoms that were "left over" (hadn't decayed) from the previous implantation period, referred to as $N_{leftovers}$, the exponential decay of N_0 is determined for the time of one implantation period, t_{on}, *and* one beam off period, t_{off}:

$$N_{leftovers} = N_0 e^{-\lambda(t_{on}+t_{off})} \tag{3.3}$$

$N_{leftovers}$ is only $(1.8 \times 10^{-2})N_0$ for the 20/40 cycle and $(1.4 \times 10^{-3})N_0$ for the 50/50 cycle. Left overs from two cycles ago would result in $(1.8 \times 10^{-2})^2 N_0$ for the 20/40 cycle and $(1.4 \times 10^{-3})^2 N_0$ for the 50/50 cycle. It is clear that left overs from even earlier implantation periods become insignificant. It was assumed therefore, that the number of ^{15}B atoms present at the end of each implantation period, $N_{0+leftovers}$, is well approximated by the expression:

$$N_{0+leftovers} = N_0(1 + e^{-\lambda(t_{on}+t_{off})}) \tag{3.4}$$

The values in the last column of Table 3.1 were determined by multiply this quantity by the total number of implantation periods during an entire run.

When the total number of implanted ^{15}B ions is compared to the number of ^{15}B atoms still remaining at the end of all the implantation periods, it is observed that the 20/40 cycle is nearly twice as efficient as the 50/50 cycle. Almost 55% of the implanted ^{15}B ions remained to be studied at the end of the implantation period for the 20/40 runs, where as this quantity was less than 30% for the 50/50 runs. From Eq.

[3] N_0 does not account for ^{15}B atoms "left over" from previous implantation periods.

3.1, it can be shown that when the implantation period, t_{on}, is very long compared to the half-life of the species being implanted, a limit of R/λ is reached. When this is the case, new activity is being formed at the same rate at which the older activity decays; this is referred to as secular equilibrium. If the implantation period is twice the half-life, 75% of the maximum activity is produced and when the implantation period is three half-lives long, this will give 88% of the maximum activity. By keeping the implantation period between two and three half-lives, the accelerator is being used most efficiently.

Table 3.1: Summary of part of the experimental runs (Group One) involved with measuring the decay of ^{15}B. These runs were used to obtain a ^{15}B half-life measurement and β-delayed neutron time-of-flight spectra. Listed are the run number and corresponding on/off cycle, the time of each run, the total number of ^{15}B ions deposited in the implantation detector (per run), the A1200 ^{15}B production rate, and the total number of ^{15}B atoms (per run) remaining at the end of the implantation period (see text for explanation).

Run # (On/Off)	Run time (sec)	^{15}B ions implanted (per run)	A1200 ^{15}B production rate (ions/ms)	^{15}B atoms remaining at end of implan. period (per run)
1 (50/50)	3,213	1.033E6	0.647	3.03E5
2 (50/50)	4,560	1.194E6	0.527	3.50E5
3 (50/50)	7,440	1.547E6	0.418	4.54E5
4 (20/40)	10,183	1.566E6	0.453	8.58E5
5 (20/40)	7,894	1.186E6	0.442	6.49E5
6 (20/40)	7,163	1.378E6	0.566	7.54E5
7 (20/40)	10,797	2.036E6	0.555	11.2E5
8 (20/40)	14,175	2.341E6	0.486	12.8E5
9 (20/40)	14,188	2.826E6	0.587	15.5E5
10(20/40)	4,880	1.064E6	0.642	5.83E5
	Σ = 84,493 (23hr,30min)	Σ = 16.11E6 (50/50 = 3.774E6) (20/40 = 12.34E6)	$\overline{x}$ = 0.532 σ = 0.081	Σ = 7.90E6 (50/50 = 1.11E6) (20/40 = 6.79E6)

3.1.2 Group Two Experimental Runs

The second group of experimental runs (# 11, 12, and 13) involved the deposition of ^{15}B ions into the implantation detector and then monitoring ^{15}C decays (β-emission, $t_{1/2}$ = 2.449±0.005 s [Aj91]) in order to determine the ^{15}B β-decay branch to ^{15}C bound states. Table 3.2 provides a summary of the Group Two runs.

The three runs in this group all used the same on/off cycle (5 s/6 s). The runs are listed separately to demonstrate the consistency among the runs. The values in the last column of Table 3.2 are the number of ^{15}C atoms remaining at the end of the implantation period and were determined using the same technique employed in the previous section (Eq. 3.4). **It was assumed** here that 100% of the ^{15}B atoms β-decay to ^{15}C bound states; this assumption, is of course, not true and is made only to demonstrate the implantation efficiency[4] (approximately 55%). Since the half-life of ^{15}B is so short (10.5 ms, [Aj91]) compared to the implantation period of 4.847 s for these runs, it is fair to assume that nearly all (99.7%) of the implanted ^{15}B ions decay to some state of ^{15}C by the end of each implantation period. It is almost as though a ^{15}C ion beam of mixed energy states was being deposited into the implantation detector.

3.1.3 Group Three Experimental Runs

The third and final group of experimental runs (# 14) involved depositing beams of ^{15}C and ^{17}N into the implantation detector in order to determine the detector's β-decay detection efficiency for ^{15}C decays. This efficiency is important to determine the ^{15}B β-decay branch to ^{15}C bound states from the Group Two runs. Table 3.3 contains the information for this run.

[4]Not to be confused with the implantation detector's β-detection efficiency !

In run # 14 the A1200 was tuned such that both ^{15}C and ^{17}N ions were present at the focal plane of the device and transported to the implantation detector. From the projectile fragmentation of the primary ^{18}O beam, the production cross section for ^{17}N is much greater than it is for ^{15}C. While the A1200 was tuned for maximum transmission of ^{15}C, the "tail" of the ^{17}N momentum distribution appeared as a sizeable contaminant. The production rates of ^{15}C and ^{17}N for run 14, 0.43 ions/ms and 0.59 ions/ms respectively, confirm this. It was actually beneficial to have the ^{17}N ions, in addition to the ^{15}C, in understanding the implantation detector's β-detection efficiency; this will be explained later.

Table 3.2: Summary of part of the experimental runs (Group Two) involved with measuring the decay of ^{15}B. These runs were used to measure the ^{15}B β-decay branch to ^{15}C bound states. Listed are the run number and on/off cycle (only 5 s/6 s cycle was used for these runs), the time of each run, the total number of ^{15}B ions deposited in the implantation detector (per run), the A1200 ^{15}B production rate, and the total number of ^{15}C atoms (per run) remaining at the end of the implantation period **assuming** a 100% ^{15}B β-decay branch to ^{15}C bound states (see text).

Run # (On/Off)	Run time (sec)	^{15}B ions implanted (per run)	A1200 ^{15}B production rate (ions/ms)	^{15}C atoms remaining at end of implan. period (per run)
11 (5/6)	32,442	7.390E6	0.497	4.02E6
12 (5/6)	20,017	4.301E6	0.468	2.34E6
13 (5/6)	11,322	2.861E6	0.551	1.56E6
	Σ = 63,781 (17hr,45min)	Σ = 14.55E6	$\overline{x}$ = 0.505 σ = 0.042	Σ = 7.92E6

Table 3.3: Summary of part of the experimental runs (Group Three) involved with measuring the decay of ^{15}B. This run was used to determine the implantation detector's β-decay detection efficiency for ^{15}C. Listed is the run number and on/off cycle (only 5 s/7 s cycle was used), the time of the run, the total number of ions deposited in the implantation detector (per run), the A1200 production rate, and the total number of atoms (per run) remaining at the end of the implantation period.

Run # (On/Off)	Run time (sec)	Ions implanted (per run)	A1200 production rate (ions/ms)	Atoms remaining at end of implan. period (per run)
14 (5/7)	1,825	3.187E5 (^{15}C) 4.327E5 (^{17}N)	0.434 (^{15}C) 0.589 (^{17}N)	1.74E5 (^{15}C) 2.99E5 (^{17}N)

3.2 A Measurement of the Half-life of ^{15}B

In the present work, decay curves for ^{15}B inclusive β-emission were obtained for the Group One runs (one through ten). A least-square fitting procedure which assumed a single exponential decay component and a constant background was used to deduce the half-life of ^{15}B, and in addition, the activity present at time-zero, A_0 [5]. The least-square fitting procedure could be applied to the data between specified beginning and end channels (these channels correspond to time). Since the decay is exponential, the half-life should be independent as to where the fit is begun and ended. For example, the same half-life should be obtained for a fit between channels # 5 to # 80 (2.44 ms to 39.06 ms) or channels # 10 to # 75 (4.88 ms to 36.62 ms) where the 2.44 ms and 4.88 ms correspond to time after the end of the implantation period (calibration of 0.48828 ms/ch). Indeed, using these two different "fitting limits", half-life values of 10.3±0.2 ms and 10.2±0.3 ms were obtained for ^{15}B. The A_0 value obtained, however, will depend on where the fit is begun and must be corrected for the exponential decay that occurs between the actual end of the implantation period and start of the data fit in order to obtain the true activity, $A_{0,true}$, present at the end of the implantation period. For runs one through ten, the fit to the data began at 2.44 ms after the end of the implantation period (ch. # 5) and $A_{0,true}$ was calculated as:

$$A_{0,true} = \frac{A_0}{e^{-\lambda_{^{15}B}\cdot(2.44ms)}} \tag{3.5}$$

Channel # 5 was choosen because this gave good fitting results for all ten runs. Other fitting limits were tried, giving very similar $A_{0,true}$ values once the appropriate compensation was made to account for the exponential decay. Table 3.4 is a summary

[5] A similar fitting procedure was tried in which the components' decay constants could be fixed to include a ^{12}Be component, in addition to the ^{15}B component. The ^{12}Be appeared to make no noticeable contribution to these decay curves. Calculations made by estimating the amount of ^{12}Be that should decay along with ^{15}B (determined from the A1200 beam purity and on/off cycle time) indicate the ^{12}Be A_0 should at most be 0.35% that of the ^{15}B A_0.

of half-life and $A_{0,true}$ values obtained from the decay of ^{15}B during these runs.

Referring to Table 3.4, there is good agreement among the different runs for the half-life measurement of ^{15}B. Figure 3.1 is the decay curve obtained by summing all the 20/40 cycle runs (4 through 10). The same fitting procedure used to fit the individual runs was used here, giving a half-life of 10.3±0.2 ms and $A_{0,true}$ of (3.56±0.02)E5 cts./ms (the error in this value represents both the statistical error from the fitting procedure and the error in the ^{15}B decay constant needed to determined it). The background component was 3.53E3 cts./ms (bkgd:$^{15}B \approx$ 1:100); the reduced chi-square for this fit was 0.4. This half-life is in good agreement with the adopted value of 10.5±0.3 ms for ^{15}B from the literature [Aj91].

It should be noted that the decay curve shown in Figure 3.1 is the result of having a total of almost 5 million ^{15}B atoms in the sample population. The 5 million is determined by knowing the number of ^{15}B atoms at the end of all implantation periods and then determining the actual number that decayed during the beam off period, t_{off} (39.55 ms):

$$Decays = \frac{A_{0,true}}{\lambda_{^{15}B}}(1 - e^{-\lambda_{^{15}B} t_{off}}) \tag{3.6}$$

Earlier studies were conducted at the Michigan State University National Superconducting Cyclotron Laboratory of the ^{15}B half-life by Curtin, *et al.* in 1986 [Cu86] and Samuel, *et al.* in 1988 [Sa88]; refer to Table 1.1. These groups used the NSCL Reaction Products Mass Separator (RPMS) [Ha81] to separate out the ^{15}B nuclei produced in projectile fragmentation reactions. In each of these earlier experiments, a total of approximately 3000 ^{15}B decays were measured from which the half-life was determined. Comparing this number to the nearly 5 million of the present work, it is quite clear that the A1200 radioactive beam device can provide impressive production rates of exotic nuclei for decay studies.

In the present work, an additional decay curve was obtained for ^{15}B by requiring β-neutron coincidences from which a half-life of 10.5±0.5 ms was obtained. Here, the ^{15}B $A_{0,true}$ was 6.01E3 cts./ms and the background component was 1.37 cts./ms (bkgd:^{15}B $\approx$ 1:4400); the reduced chi-square for this fit was 1.08. This decay curve is shown in Figure 3.2. This measurement was obtained by requiring an event to occur in any one of the sixteen neutron detectors of the array in coincidence with a β-decay in the implantation detector (this was done entirely in software). When compared to the decay for inclusive β-emission, the β-neutron coincidence measurement had about a 44-fold decrease in background, as should be expected.

Table 3.4: Summary of the half-life, $t_{1/2}$, and true activity present at the end of the implantation period, $A_{0,true}$, obtained from the decay of ^{15}B inclusive β-emission for the Group One experimental runs (one through ten). Also included is the background component for each run and the reduced chi-square for the least-square fitting procedure.

Run # (On/Off)	$t_{1/2}$ (ms)	$A_{0,true}$ (cts./ms)	Bkgd. (cts./ms)	$R\chi^2$
1 (50/50)	10.5±0.38	1.54E4	1.29E2	1.19
2 (50/50)	10.3±0.36	1.79E4	2.68E2	1.10
3 (50/50)	10.2±0.34	2.32E4	4.12E2	0.83
4 (20/40)	10.2±0.30	4.41E4	6.99E2	1.05
5 (20/40)	10.2±0.31	3.37E4	6.25E2	0.97
6 (20/40)	10.4±0.30	3.92E4	3.82E2	0.78
7 (20/40)	10.3±0.29	5.83E4	6.28E2	0.90
8 (20/40)	10.3±0.28	6.74E4	8.07E2	0.86
9 (20/40)	10.4±0.31	8.23E4	6.79E2	0.74
10 (20/40)	10.4±0.32	3.07E4	1.86E2	0.77
	$\overline{x}_{weighted} = 10.3$ $\sigma_{weighted} = 0.11$	$\Sigma = 41.22E4$ (50/50) = 5.65E4 (20/40) = 35.57E4		

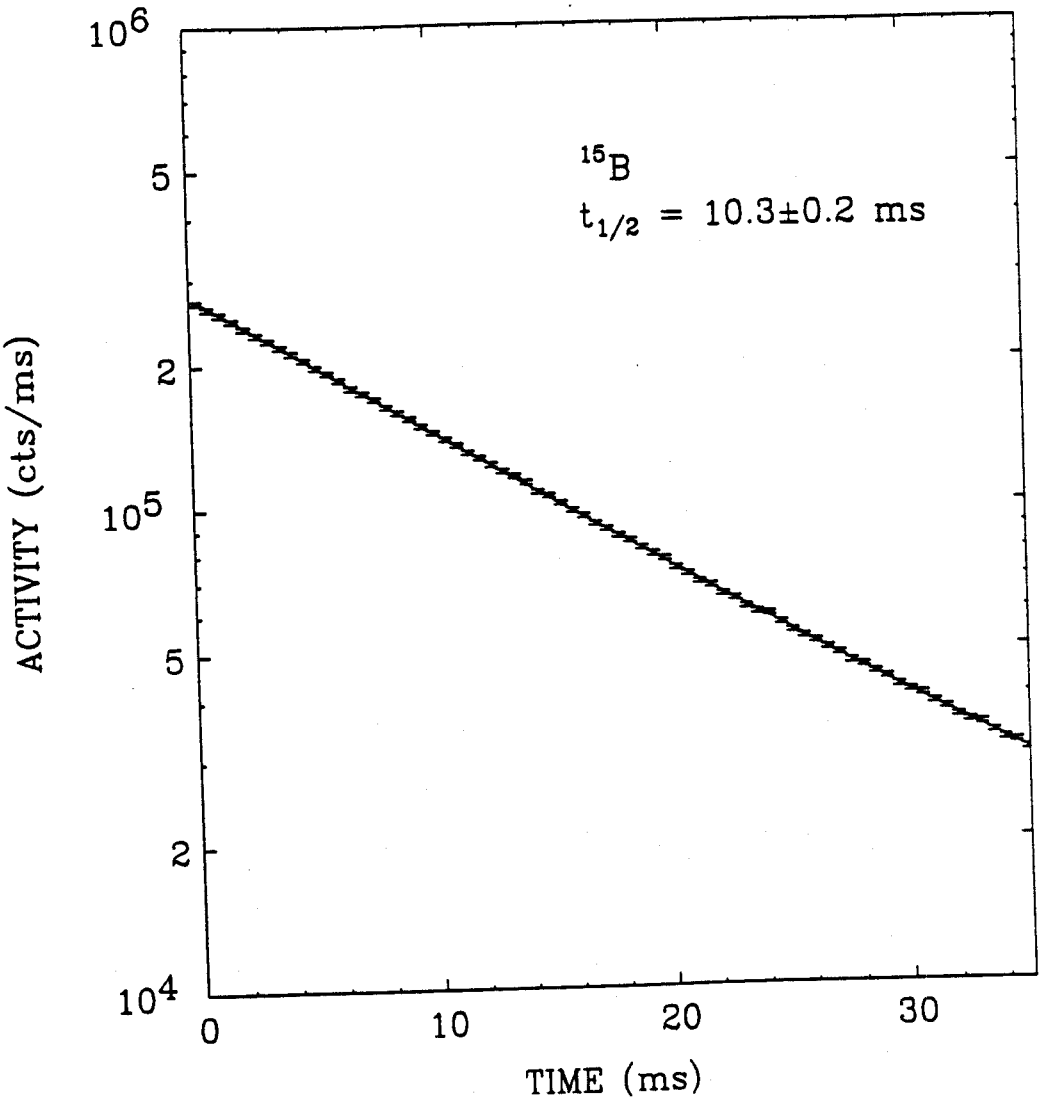

Figure 3.1: Experimental decay curve for ^{15}B inclusive β-emission obtained by summing all the 20/40 cycle runs (4 through 10). The solid line corresponds to a single-component fit plus a constant background.

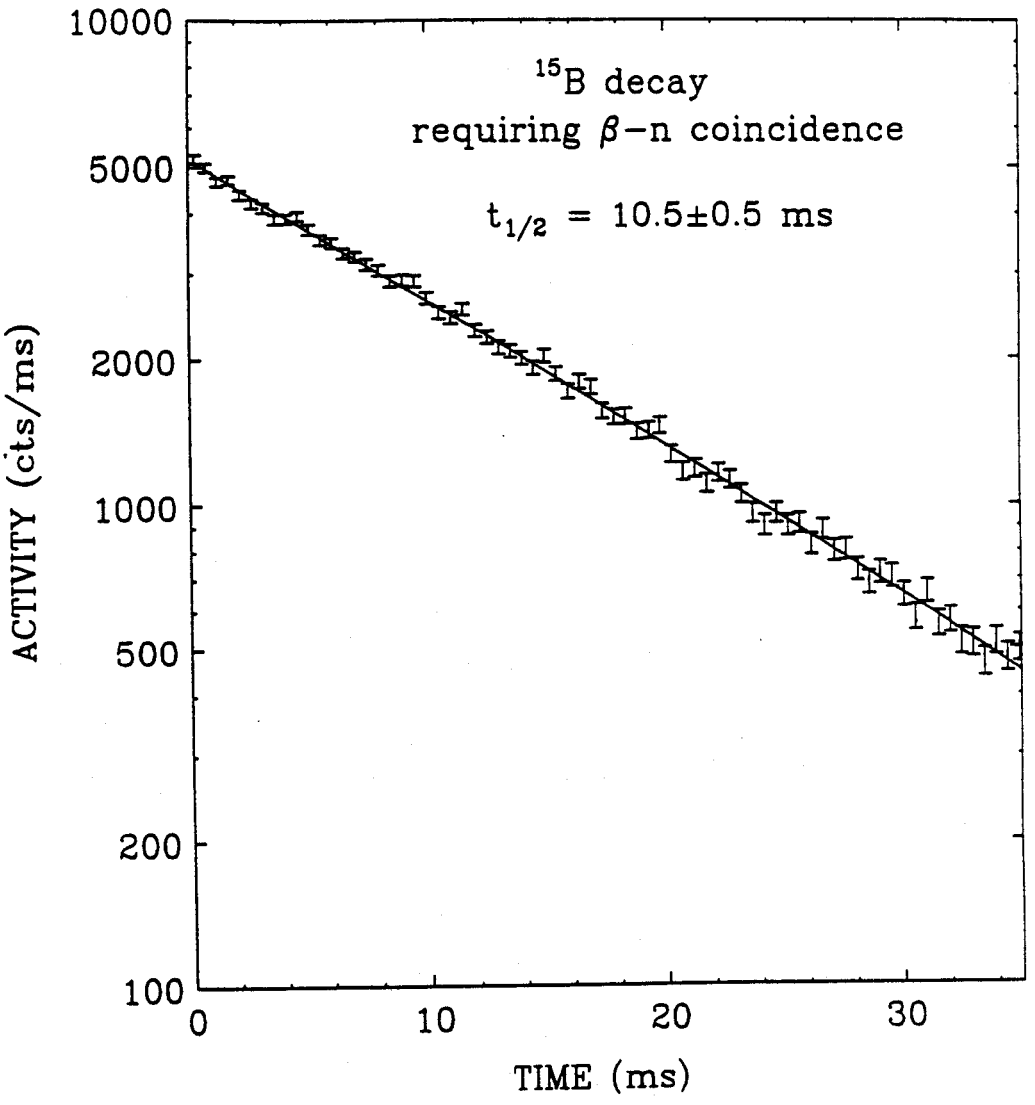

Figure 3.2: Experimental decay curve for ^{15}B requiring β-neutron coincidence. The solid line corresponds to a single-component fit plus a constant background.

3.3 ^{15}B β-Decay to ^{15}C Bound States

This section addresses the ^{15}B β-decay branch to bound states in ^{15}C. Recall, the Group Two runs involved the deposition of ^{15}B ions into the implantation detector during a 4.847 s beam on period and then monitoring the β-decay of ^{15}C during a 5.719 s beam off period, and the Group Three runs involved the deposition of ^{15}C and ^{17}N ions from the A1200 into the implantation detector in order to determine the detector's β-detection efficiency.

3.3.1 ^{15}C β-Decay Following the Implantation of ^{15}B

The decay curve obtained from each individual Group Two run was fit with a least-square fitting procedure in which each component's[6] decay constant was fixed and its activity (A_0) was a free parameter; the decay curve generated from the sum of these individual runs was also fit with this procedure. These results are summarized in Table 3.5 and the fitted decay curve for the summation of the three runs is shown in Figure 3.3. The least-square fit for these decay curves started at 0.375 s (channel # 3, 0.125 s/ch.) after the end of the ^{15}B implantation to insure that essentially all the implanted ^{15}B ions decayed (more about the decay of ^{15}B during these runs will be mentioned later).

Notice that the measurements from the Group Two runs were more sensitive to the longer lived A1200 impurities ^{6}He ($t_{1/2}$ = 0.807 s [Aj88]) and ^{9}Li ($t_{1/2}$ = 0.178 s [Aj88]). Referring to Table 2.1, the percentage of A1200 secondary beam that actually stopped in the implantation detector was 0.56% ^{6}He, 0.83% ^{9}Li, and 97.8% ^{15}B. Accounting for the number of ^{6}He and ^{9}Li atoms that would be present along with the 14.55E6 ^{15}B atoms implanted during these runs, 8.34E4 and 12.4E4

[6]The components for these runs include ^{15}C and the known impurities ^{9}Li, ^{6}He, and a constant background.

respectively, and then the number of ^{6}He and ^{9}Li atoms which would be present at the end of the implantation period using Eq. 3.4, 1.96E4 and 0.657E4 respectively, the measured initial count rate ($A_{0,true}$) should be 17.0E3 cts/s for ^{6}He and 25.6E3 cts/s for ^{9}Li, *if* the implantation detector was 100% efficient for the β-particle detection of decays from ^{6}He and ^{9}Li. Referring to the results in Table 3.5, the measured $A_{0,true}$ value was (6.5±1.7)E3 cts/s for ^{6}He and (7.3±4.3)E3 cts/s for ^{9}Li. These values are in reasonable agreement with the calculated estimates considering the large uncertainties in the A_0 values and also that the implantation detector does not have 100% β-detection efficiency. This efficiency will be addressed in the following subsection.

Before the ^{15}B β-decay branch to ^{15}C bound states can be deduced, the implantation detector's β-detection efficiency for ^{15}C decay must be determined.

Table 3.5: Summary of the Group Two experimental runs in which ^{15}B ions were deposited into the implantation detector during a 5 s beam on period and decays were monitored during a 6 s beam off period. The decay curves from these runs were fit with a least-square procedure in which each component's decay constant was a fixed parameter and its activity was a free parameter. The components of each fit and the corresponding activity, A_0, are shown in the fourth column. The adjusted activities, $A_{0,true}$, account for the 0.375 s that elapsed between the end of implantation period and the beginning of the fit and are shown in the fifth column. The last column lists the reduced chi-square for the least-square fitting procedure.

Run #	time of run (s)	^{15}B ions implanted	A_0 from fit (10E3 cts./s)	$A_{0,true}$ (10E3 cts./s)	$R\chi^2$
11	32,442	7.390E6	8.37±0.52 (Bkgd.)	8.37±0.52	0.90
			3.50±0.93 (^{15}C)	3.89±1.0	
			2.76±1.0 (^{6}He)	3.81±1.4	
			0.54±0.87 (^{9}Li)	2.3±3.7	
12	20,017	4.301E6	4.78±0.45 (Bkgd.)	4.78±0.45	1.21
			2.51±0.81 (^{15}C)	2.79±0.90	
			0.66±0.88 (^{6}He)	0.91±1.2	
			0.93±0.76 (^{9}Li)	4.0±3.3	
13	11,322	2.861E6	2.81±0.39 (Bkgd.)	2.81±0.39	0.97
			1.22±0.71 (^{15}C)	1.36±0.79	
			0.28±0.77 (^{6}He)	1.77±1.1	
			0.24±0.67 (^{9}Li)	1.0±2.9	
11,12,13 (sum)	63,781	14.55E6	16.0±0.61 (Bkgd.)	16.0±0.61	1.10
			7.26±1.1 (^{15}C)	8.07±1.2	
			4.68±1.2 (^{6}He)	6.45±1.7	
			1.70±1.0 (^{9}Li)	7.31±4.3	

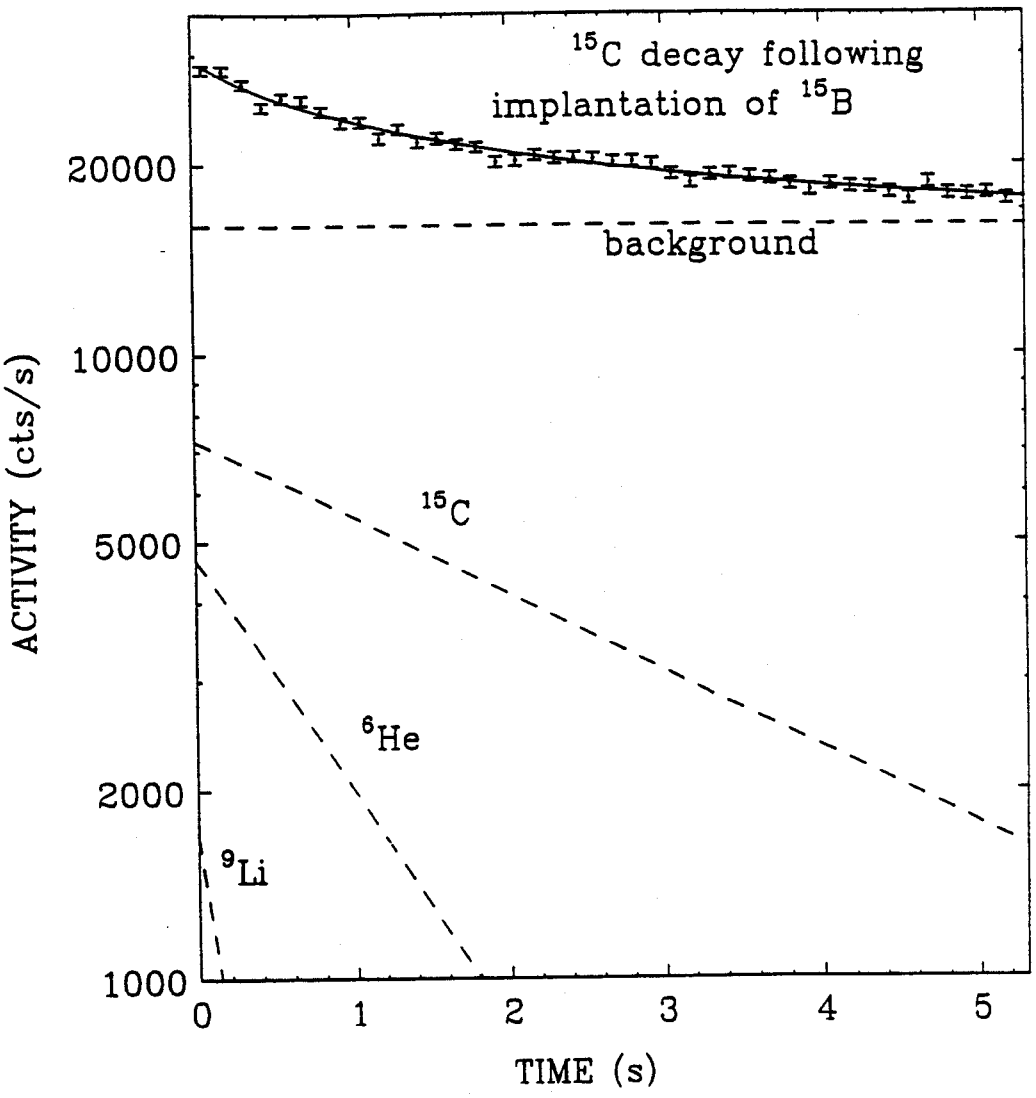

Figure 3.3: Experimental decay curve generated by summing the three individual runs of Group Two. During these runs ^{15}B ions were deposited into the implantation detector during the 5 s beam on period and decays were monitored during the 6 s beam off period. The solid line corresponds to a three-fit component (^{6}He, ^{9}Li, ^{15}C) plus a constant background. The error bars are statistical.

3.3.2 The Implantation Detector's β-Detection Efficiency

The implantation detector's β-detection efficiency for observing ^{15}C β-decay and its efficiency for ^{15}B β-decay must be determined. Recall it was shown in Section 2.2 of the previous chapter that the 60 MeV/A ^{15}B ions that entered the experimental vault came to rest at a depth of 5.2±1.2 mm in the 10.0 mm thick implantation detector. It can be assumed that *all* the implanted ^{15}B ions decayed by β-emission with a total half-life of 10.3±0.2 ms (half-life determined from the present work), without knowledge of what percentage of the decays populated bound states in ^{15}C. Using the number of ^{15}B atoms that remained at the end of the implantation period (listed in Table 3.1) and the measured activity as a result of these implantations, $A_{0,true}$ (listed in Table 3.4), the efficiency of the implantation detector for ^{15}B β-emission was determined for the Group One runs; these data are summarized in Table 3.6.

Referring to Table 3.6, there is good agreement among the efficiencies determined for the ten individual runs of Group One. It should also be noted such consistency between runs also supports the assumption that, for individual runs, the production rates were constant. The adopted value for the β-detection efficiency of the implantation detector for ^{15}B β-emission is taken to be 80.6±2.3% (uncertainty taken to be $\pm 2\sigma$).

Now that the β-detection efficiency of the implantation detector for ^{15}B decay has been established, the Group Three run (# 14) can be addressed. Recall that during the Group Three run ^{15}C ($t_{1/2}$ = 2.449 s [Aj91]) and ^{17}N ($t_{1/2}$ = 4.173 s [Aj86]) ions from the A1200 radioactive beam device were deposited into the implantation detector during a 4.762 s implantation period and decays monitored during a 7.063 s beam off period (refer to Table 3.3). The decay curve obtained from this run is shown in Figure 3.4. The same least-square fitting procedure used to fit the runs of Group Two

was used here (decay constants are fixed and activities are free parameters). Table 3.7 presents a summary of the measured activities from this run and the calculated β-detection efficiency of the implantation detector for the ^{15}C and ^{17}N decays.

The summary of the implantation detector's β-detection efficiency is thus 80.6±2.3%, 47.8±4% and 55.9±4% for the decay of ^{15}B, ^{15}C and ^{17}N, respectively. Recall, that 6.8 mm of aluminum degrader was used during the implantation of ^{15}B ions (Group One runs) and from the calculated energy-loss [Hu90], it was determined that the ^{15}B ions came to rest at a depth of 5.2±1.2 mm in the 10 mm thick detector. Using the same energy-loss calculation and technique as above, it is determined that 2.5 mm of aluminum degrader should have been used for the 54.3 MeV/A ^{15}C ions from the Group Three run in order that they come to rest in the center (depth of 5 mm) of the implantation detector. By having the ^{15}B and ^{15}C ions come to rest at the same depth of the implantation detector, a fair comparison of their efficiencies could be made; differences in the efficiencies could then be attributed solely to differences in the nature of the β-particles of the decays[7]. During the experiment 2.3 mm instead of 2.5 mm of aluminum degrader was used for the implantation of ^{15}C and ^{17}N. The ^{15}C ions actually came to rest at a depth of 6.4±0.8 mm and the ^{17}N ions at 5.4±0.7 mm in the 10 mm thick implantation detector. The efficiency of the implantation detector depends on the amount of energy a β-particle deposits in the detector (the more energy deposited, the more likely it will be detected). The amount of energy deposited by the β-particle is dependent on the amount of material it travels through and its kinetic energy (maximum energy deposited by low energy β-particles traveling through the maximum distance of material, in this case when it originates at the center of the detector). Before attempting any comparisons of the efficiencies, it is helpful to compare the implantation depth, the "actual" average β-

[7]Since the stopped ion, or properly termed atom, produces the β-particle, it can be assumed that the β-particle's origin in the implantation detector is where its parent ion came to rest.

particle energy from the decay[8], and the calculated implantation detector β-detection efficiency. Table 3.8 summarizes this comparison for ^{15}B, ^{15}C, ^{17}N, and also for the ^{6}He and ^{9}Li impurities of the Group Two runs.

Reiterating that the implantation detector's β-detection efficiency is dependent on the implantation depth and energy of the β-particle, and referring to the information contained in Table 3.8, several conclusions can be made. First, the efficiencies obtained for the ^{6}He and ^{9}Li impurities of the Group Two runs are too uncertain to serve in establishing what is needed to determine the ^{15}B decay branch to ^{15}C bound states (*the primary goal here*). While it is certain that some of the ^{6}He and ^{9}Li came to rest in the implantation detector, some passed through it without stopping (verified by these ions appearing in the veto detector), and it is fair to say that these ions most probably came to rest at various depths in the implantation detector. In addition, due to the uncertainity in the least-square fit of the decay curve for these impurities (refer to Table 3.5) there are large uncertainties in their calculated efficiencies.

For the ^{15}B, ^{15}C and ^{17}N, the efficiencies and implantation depths could be calculated with reasonable accuracy. While the average energy of the β-particle was greater from the decay of ^{15}B (5.4 MeV) than it was from the decay of ^{15}C (2.2 MeV) or ^{17}N (1.3 MeV), the detector's efficiency was highest for the ^{15}B (80.6%). Since higher energy β-particles deposit less energy in their passage through matter (smaller $-dE/dx$) than lower energy ones[9], the higher efficiency for the β-particles from the decay of ^{15}B may have to be attributed to the implantation depth. The lower efficiency of the detector for ^{15}C β-decay from the Group Three run might be attributed

[8]This "actual" average energy is 0.35 of a weighted average. The weighted average is determined by the states and branching ratios populated in the daughter atom; the 0.35 accounts for part of the decay energy carried away by the neutrino. The 5.4 MeV listed for ^{15}B is actually determined from information provided later in this chapter.

[9]Actually $-dE/dx$ for β-particles of these three energies are very similar, they are of energies that would classify all of them as being minimum ionizing.

to its "over-depth implantation" (the 6.4 mm depth instead of 5 mm for the ^{15}C)[10]; this however does not adequately explain the lower efficiency for ^{17}N β-decay, since the ^{17}N atoms came to rest almost in the center of the implantation detector (5.4 mm). It may also be that the A1200 beam spot was not centered on the implantation detector during the Group Three run; this could diminish the detector's efficiency.

By considering that (1) the β-decay of the ^{15}B parent and the ^{15}C daughter atoms took place at the same location inside the implantation detector, (2) the average energy of the β-particles from the decays of ^{15}B and ^{15}C differ by only 5% in their $-dE/dx$ in plastic [Pa72], and (3) the low energy threshold setting of the implantation detector (100 keV), it is concluded the implantation detector had the same β-detection efficiency for decays of ^{15}B and ^{15}C *as long as* these decays occur at the same detector depth; since the ^{15}C atoms are daughters of the ^{15}B atoms, the decays *do* occur at the same depth.

Having now established that the implantation detector's β-detection efficiency for the decay of ^{15}C is 80.6%, the ^{15}B β-decay branch to ^{15}C bound states can be addressed.

[10]When ions come to rest near the surface of the implantation detector, some β-particles exit the detector without having traveled through enough material to be detected.

Table 3.6: Summary of the implantation detector's β-detection efficiency for the β-decay of ^{15}B from the Group One experimental runs.

Run # (On/Off)	Implantation detector's β-efficiency
1 (50/50)	79.7%
2 (50/50)	79.8%
3 (50/50)	79.3%
4 (20/40)	79.4%
5 (20/40)	80.3%
6 (20/40)	80.7%
7 (20/40)	81.1%
8 (20/40)	81.4%
9 (20/40)	82.6%
10 (20/40)	82.0%
	$\overline{x} = 80.6\%$ $\sigma = 1.15$

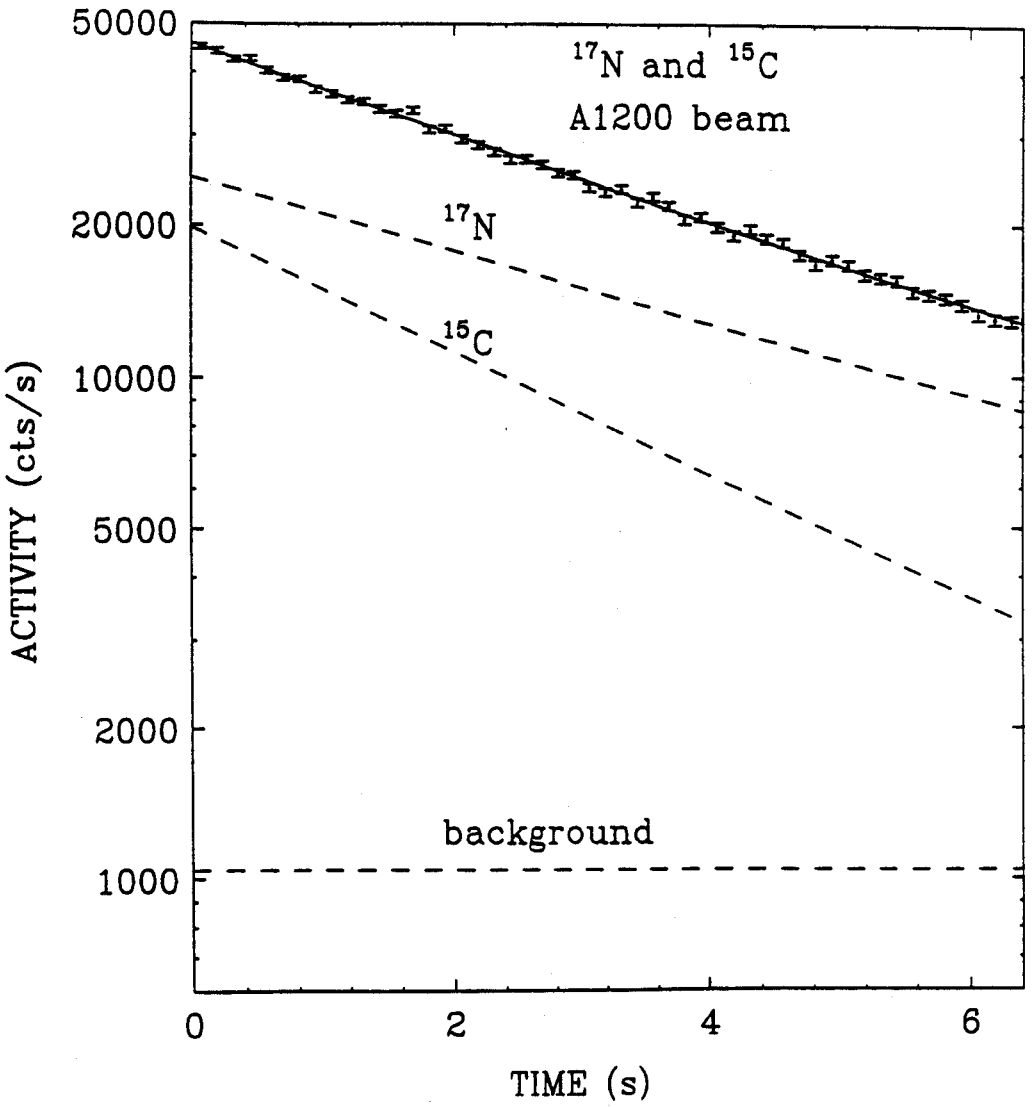

Figure 3.4: Experimental decay curve for the Group Three experimental run. During run # 14, ^{15}C and ^{17}N ions from the A1200 were deposited into the implantation detector during a 5 s implantation period and decays were monitored during the 7 s beam off period. The solid line corresponds to a two component-fit plus a constant background.

Table 3.7: Summary of the implantation detector's β-detection efficiency from the Group Three run. The $A_{0,true}$ values were obtained from the fitted decay curve shown in Figure 3.4; also listed is the reduced chi-square value for the least-square fitting procedure used to obtain these values. The efficiencies were deduced from these $A_{0,true}$ values and the number of atoms present at the end of the implantation period.

Run #	$A_{0,true}$ (10E3 cts./s)	$R\chi^2$	Implantation detector's β-efficiency
14	26.9±2.0 (^{17}N) 22.8±1.9 (^{15}C) 1.1±0.9 (Bkgd.)	0.833	55.9±4% 47.8±4%

Table 3.8: Summary of the implantation detector's β-detection measured efficiency for implantated ions from Groups One, Two and Three runs. Also listed is the "actual" average β-particle energy from the decay (see text for explanation) and the depth of implantation into the 10 mm thick implantation detector.

Ion implanted	Average β-particle energy (MeV)	Implantation depth (mm)	Implantation detector's β-detection efficiency
^{15}B (Group One runs)	5.4	5.2±1.2	80.6±2.3%
^{17}N	1.3	5.4±0.7	55.9±4%
^{15}C (Group Three run)	2.2	6.4±0.8	47.8±4%
^{9}Li	4.0	(disperse)	29±20%
^{6}He (Group Two runs)	1.2	(disperse)	39±12%

3.3.3 Determination of the β-Decay Branch to ^{15}C Bound States

As discussed earlier in this chapter, since the half-life of ^{15}B is so short compared to the 4.847 s implantation period, virtually all the implanted ^{15}B ions decayed to some state of ^{15}C before the end of the implantation period (99.7% using Eq. 3.4). A total of 14.55E6 ^{15}B ions were deposited into the implantation detector during all the Group Two runs. This would result in 4.5E4 ^{15}B ions still remaining at the end of the implantation period. Indeed, when the decay curve was generated from all the Group Two runs a sharp peak was observed in the first channel with 3.9E4 counts. Compensating for computer dead time and the β-detection efficiency gives 4.7E4 counts, in good agreement. As such, it can be imagined that a ^{15}C ion beam was deposited into the implantation detector. By determing the number of ^{15}C atoms that remained at the end of the implantation period (Table 3.2), knowing the activity attributed to the decay of ^{15}C (Table 3.5), and accounting for the implantation detector's β-detection efficiency, the ^{15}B β-decay branch to ^{15}C bound states can be determined; the summary of these findings are listed in Table 3.9.

Referring to Table 3.9, there is reasonable agreement among the three individual Group Three runs for the ^{15}B decay β-decay branch to ^{15}C bound states, and the value of 0.46$\pm$0.08% from the summed data will be adopted in the present work; the error in this value accounts for the statistical error in the least-square fitting procedure from which the ^{15}C activity was determined and also the error in the β-detection efficiency of the implantation detector. This measurement is in agreement with, though significantly lower than, the limit of $P_{0n} < 5\%$ established by Dufour *et al.* [Du84]. A more recent measurement of the P_{1n} for ^{15}B made by Reeder *et al.* [Re91] will be addressed in the next section of this chapter which supports the P_{0n} of 0.46% established here.

In the following section, the β-delayed neutron time-of-flight spectra obtained for ^{15}B will be examined and the decay branch to the unbound states in ^{15}C will be established, leading to a determination of the ^{15}B β-decay branching ratios.

Table 3.9: Summary of the determined ^{15}B β-decay branching ratios to ^{15}C bound states determined individually from the three experimental runs of Group Two. Also listed is the decay branch determined from the decay curve generated from the summation of these runs.

Run #	^{15}B β-decay branch to ^{15}C bound states
11	0.43±0.10%
12	0.53±0.15%
13	0.39±0.22%
Sum of runs 11, 12 and 13	0.46±0.08%

3.4 ^{15}B β-Decay to ^{15}C Unbound States – β-Delayed Neutron Emission

This section presents the results for the β-delayed neutrons emitted in the decay of ^{15}B. A review of the energy level scheme of ^{15}C (Figure 1.2) shows that three neutron decay channels are possible. The majority of the neutron decays occur via the ground state of ^{14}C and involve the populated low level (states below 7.31 MeV), negative parity states of ^{15}C. These decays will be addressed first in this section. If the state populated in ^{15}C is at least 7.31 MeV, single neutron decay via the first excited state of ^{14}C is possible, and two neutron emission via the ground state of ^{13}C is possible if the populated ^{15}C state is at least 9.40 MeV. These decay channels will be addressed in the latter part of this section.

3.4.1 ^{15}B β-Delayed Neutron Time-of-Flight Measurements

The Group One runs, in addition to supplying the data for the ^{15}B half-life determination, were used to obtain ^{15}B β-delayed neutron time-of-flight measurements. Each of the sixteen neutron detectors of the array provided a separate time-of-flight neutron spectrum. Figure 3.5 shows the results obtained from detector # 6; the top figure is the "raw" unfitted time-of-flight neutron spectrum, the bottom figure is the expanded, fitted spectrum showing five neutron peaks and their energies. The fitted time-of-flight spectra obtained from detectors # 1 through 8 are shown in Figure 3.6 (the bottom spectrum shown in Figure 3.5 is the same spectrum shown here for detector # 6, only larger), those obtained from detectors # 9 through 16 are shown in Figure 3.7. The details which will now be described concerning detector # 6 (raw spectrum and fitting procedure) pertain to and were observed in the other fifteen detectors, detector # 6 is used only as an of example.

Referring to Figure 3.5, the unfitted spectrum shows a peak centered at channel number 186.6 resulting from relativistic electrons that traveled from the implantation detector to the neutron detector (i.e. the β-decay of ^{15}B). These electrons travel at a velocity very near the speed of light, c, (their average energy is 5.4 MeV, giving them a velocity of 0.996c or 29.88 cm/ns), taking 3.35 ns to travel the 1 meter flight path, and are used to establish a time reference. An accurate time calibration of 0.3428 ns/ch was made using an electronic time calibrator. The small "cosmic" peak which was explained earlier in Section 3 of Chapter II, is seen here. The program PHAEDRUS [Sc83] was used to fit simultaneously the five β-delayed neutron peaks.

The low level, negative parity states of ^{15}C have level widths on the order of 10 to 40 keV [Aj91]; these are small compared to the peak widths caused by instrumentation. The peak widths used in the PHAEDRUS fitting procedure were forced to be fixed parameters. Their widths were determined from the total time uncertainty, a combination of 1.0 ns from the electronics[11], and a neutron-energy dependent time-uncertainty owing to a total flight path uncertainty, determined to be 4.25 cm[12] for detector # 6. This flight path uncertainty, and the subsequent width of the neutron peaks, were determined as follows.

First, an estimate of the neutron velocity in ns/cm corresponding to each peak was made using the centroid of the particular peak, C_n, the centroid of the β-peak,

[11]The 1.0 ns time resolution owing to electronics was the FWHM of the γ-peak observed in the time-of-flight spectrum from a collimated ^{60}Co source. Although this measurement is not totally independent of flight path uncertainty (the γ-ray may have interacted at the front or the back of the neutron detector, a difference of 2.54 cm or about 0.17 ns in flight time), these uncertainties were minimized by placing the collimated source flush against one part of the detector thereby minimizing flight path uncertainty due to the detector's curvature.

[12]This total flight path uncertainty is the result of three contributions. First, the thickness of the neutron detector (2.54 cm) and not being able to tell at what depth of the detector the neutron actually was detected. Second, the size of the ^{15}B beam spot on the implantation detector; this could be as large as 2 cm (height dimension of the implantation detector). Third, the neutron detector's deviation from a true 1 m radius of curvature; some parts of the 157 cm long detector were actually closer (or further) from the implantation detector than other parts and this adds an additional 2 cm to the uncertainty.

C_β, the time calibration, ns/ch, the known flight path of 100 cm and accounting for the 3.35 ns it took the β-particle to travel 100 cm:

$$v_n = \frac{100cm}{(C_n - C_\beta) \times ns/ch + 3.35ns} \tag{3.7}$$

For the lowest energy neutron peak in the raw spectrum (top of Figure 3.5, peak furthest to right), this velocity turns out to be 1.84 cm/ns, corresponding to a neutron energy of about 1.77 MeV[13]. Since the lowest energy peak was not "riding on the shoulder" of any other peak but was well separated and Gaussian, its peak width could be very easily measured and was selected to be the standard from which the other peak widths would be determined. Its peak width was 7.35 channels or 2.52 ns (0.3428 ns/ch). This 2.52 ns is the *total* time uncertainty. Reiterating, the total time uncertainty, Δt_{total}, is a combination of the time uncertainty from the electronics (1.0 ns), Δt_{elec}, and the time uncertainty owing to the uncertainty in flight path, $\Delta t_{\Delta l}$:

$$\Delta t^2_{total} = \Delta t^2_{elec} + \Delta t^2_{\Delta l} \tag{3.8}$$

As such, $\Delta t_{\Delta l}$ for this peak is 2.31 ns. Knowing the velocity of the neutron, v_n, the flight path uncertainty, Δl, can be determined:

$$\Delta l = \Delta t_{\Delta l} \times v_n \tag{3.9}$$

and is 4.25 cm; this value is reasonable considering the three sources of flight path uncertainty, and their amounts, discussed in footnote # 12. Now having established the flight path uncertainty, the widths of the four other neutron peaks can easily be determined by simply reversing the order of the above process. The total width of these peaks for detector # 6, going from the lowest to highest neutron energy, turns out to be 2.52 ns, 2.09 ns, 1.99 ns, 1.79 ns, and 1.73 ns. These are the widths that were

[13]For neutrons with energies much lower then the neutron's rest mass (939.6 MeV), the neutron energy in MeV is approximately the square of the velocity (cm/ns) times 0.523.

used as fixed parameters in the PHADERUS fitting procedure resulting in the fitted spectrum shown at the bottom of Figure 3.5; notice the five unfolded neutron peaks. In addition, a smooth polynomial function was fit through the regions of the spectrum with no peaks for the background. The background consisted of (1) a constant level throughout the entire spectrum resulting from random coincidence events, and (2) a steadily increasing level toward the low energy end of the spectrum resulting from decay neutrons that did not travel directly from the implantation detector to the neutron detector.

The fitted spectrum for each neutron detector resulted in a centroid for each peak from which an accurate measurement of the neutron energies could be determined, and an area for each peak from which a relative population of states or branching ratios could be deduced. The determination of the neutron energies will be addressed first.

For neutrons with kinetic energies much lower than the rest mass of the neutron (m_0c^2 = 939.6 MeV), the energy of the neutron in MeV, E_n, can be determined as follows:

$$E_n = \frac{1}{2}(939.6MeV)\frac{v_n^2}{c^2} = 0.5227v_n^2 \qquad (3.10)$$

where v_n is the neutron velocity in cm/ns and c is the speed of light in a vacuum, 29.979 cm/ns. Thus, the neutron energy is easily determined once the neutron velocity is known. Eq. 3.7 shows how to determine the neutron velocity from its centroid in the time-of-flight spectrum. Notice that this calculated velocity is a function of the flight path distance (100 cm in Eq. 3.7). It is clear that the large, lowest energy neutron peak in the time-of-flight spectra belongs to the lowest negative parity state in ^{15}C (refer to Figure 1.2). The energy of this state has been accurately measured to be 3.103±0.004 MeV [Aj91]. Accounting for the ^{14}C neutron binding energy of 1.2181 MeV [Aj91] and the recoil energy of ^{14}C during the neutron decay, the energy

of the emitted β-delayed neutron associated with this state is 1.759±0.004 MeV. Using the centroid corresponding to this state from the fitted time-of-flight spectra in Eq. 3.7 and allowing the flight path to vary such that it results in a neutron energy of 1.759 MeV is a method of calibrating the exact flight path distance for the sixteen array detectors. Then, the energies associated with the four other neutron peaks can be determined using this calibrated flight path and their centroid values from the fitted spectra. Table 3.10 shows these results for the sixteen array detectors.

Referring to Table 3.10, the calibrated flight paths are all within one cm of the assumed one meter distance. Observing the neutron energies, there is good agreement among the sixteen detectors. The neutron energies adopted from the sixteen detector measurements are taken to be 2.81±0.02 MeV, 3.21±0.01 MeV, 4.32±0.03 MeV, and 4.75±0.07 MeV (mean value of the sixteen measurements, with error being ± one σ). It should be noted that these energies are determined from a "relative" measurement. If instead a fixed flight path of 100.0 cm is choosen, the neutron energies are within 2% of the values obtained from the relative measurement. After correcting for the ^{14}C recoil energy and neutron separation energy, these correspond to ^{15}C states of 4.23±0.02 MeV, 4.66±0.01 MeV, 5.85±0.03 MeV, and 6.31±0.07 MeV. These values agree with the known low level, negative parity states in ^{15}C (refer to Figure 1.2); this will be discussed in more detail later.

Next, a determination of the relative population of these ^{15}C states can be made from the neutron peak areas and the neutron detector efficiencies established in the last chapter. The relative branching ratios for the five neutron emitting states were determined from *each* of the sixteen detector measurements in the following manner. The individual neutron peak areas, A_{N1}, A_{N2}, etc. were normalized with their corresponding (specific neutron energy and specific detector) measured efficiencies, ϵ_{N1},

ϵ_{N2}, etc. from Table 2.2 to give the relative branching ratios[14], BR_{N1},BR_{N2}, etc.

$$BR_{N1}(\%) = \frac{A_{N1}/\epsilon_{N1}}{A_{N1}/\epsilon_{N1} + A_{N2}/\epsilon_{N2} + A_{N3}/\epsilon_{N3} + A_{N4}/\epsilon_{N4} + A_{N5}/\epsilon_{N5}} \times 100 \quad (3.11)$$

These results are summarized in Table 3.11. Errors associated with these measurements will be discussed shortly.

Referring to Table 3.11, there is reasonably good agreement for the branching ratios among all the separate detectors, except for the noticably low 3.10 MeV branch of 59.0% obtained from detector # 7. A Monte-Carlo simulation was performed [Ce79] to estimate the attenuation of neutrons in the implantation detector. Assuming the neutrons travelled an average 0.5 cm of plastic before exiting the implantation detector, the probability of *any* interaction was about 10% for 1.77 MeV neutrons and this probability remained almost the same for the higher energy neutrons (9.6%, 9.1%, 9.0% and 7.0% for the 2.80 MeV, 3.21 MeV, 4.30 MeV and 4.80 MeV neutrons, respectively). Therefore, if attenuation (to the degree predicted) did occur it should effect all the neutrons in essentially the same manner and not noticably change the relative branching ratios. Detector # 7 was "straight above" the implantation detector (at a right angle to the direction of the beam axis), so if the ^{15}B beam spot was "low" the amount of plastic travelled before exiting the implantation detector could be a maximum of 1 cm. This would increase the probability for interaction with the detector, however the other energy neutrons should be effected in a similar manner. So, for the present it remains unresolved as to why the 3.10 MeV branch obtained from detector # 7 is this low and it will be interesting to see if this phenomenon is observed in future experiments using the array (this matter *is* actually addressed at the end of this chapter). Chauvenet's criterion was applied to test the "reasonableness" of the 59.0% value and showed that about 110 measurements would have to be made

[14]Note that in these calculated branching ratios, it assumes 100% of the β-delayed neutrons populate only these five ^{15}C states; this assumption will be addressed in the next section.

before obtaining one as "bad" as 59%. For this reason, a decision not to include the detector # 7 measurements was made resulting in some noticeably smaller standard deviations, given at the bottom of Table 3.11. These standard deviations from the mean values can be regarded as a *random* component of the total uncertainty in the branching ratio measurements. Next, an estimation of error associated with each array detector measurement can be made which can be regarded as an *instrumentation* uncertainty.

Referring to Eq. 3.11, each calculated branching ratio percentage is a function of the five neutron peak areas and, in addition, the five corresponding neutron detection efficiencies. As such, in order to determine the error associated with each percentage, $\lambda_{BR_{N1}}$, $\lambda_{BR_{N2}}$, etc. the following expression is evaluated:

$$\lambda_{BR_{N1}} = (\frac{\partial BR_{N1}}{\partial A_{N1}})\lambda_{A_{N1}} + (\frac{\partial BR_{N1}}{\partial \epsilon_{N1}})\lambda_{\epsilon_{N1}} + \cdots + (\frac{\partial BR_{N1}}{\partial \epsilon_{N5}})\lambda_{\epsilon_{N5}} \tag{3.12}$$

where $\lambda_{A_{N1}}$, $\lambda_{A_{N2}}$, etc. is the error associated with the neutron peak area values and is obtained from the fitting procedure, and $\lambda_{\epsilon_{N1}}$, etc. is the error associated with the measured neutron detection efficiency and obtained from Table 2.2. By taking the simple sum in the above expression rather than adding in quadrature, the estimation of $\lambda_{BR_{N1}}$ is actually a conservative upper bound and does not require that errors in the neutron peak areas and detector efficiencies be random and independent (adding in quadrature does require this). These errors were evaluated for the branching ratio percentages listed in Table 3.11 and are listed in Table 3.12. Also listed in this table is the "weighted" mean and uncertainty determined as follows:

$$x_{weighted} = \frac{\sum_{i=1}^{16} x_i/\sigma_i^2}{\sum_{i=1}^{16} 1/\sigma_i^2} \tag{3.13}$$

$$\sigma_{weighted} = (\sum_{i=1}^{16} 1/\sigma_i^2)^{-1/2} \tag{3.14}$$

where x_i and σ_i are the branching ratio percentage and associated uncertainty, respectively, for detector # i. It should be noted that the detector # 7 measurements are not included in these weighted values.

Finally, an estimate of the total uncertainty associated with the branching ratio percentages was made by adding the random uncertainty (standard deviations at the bottom of Table 3.11) and the instrumental uncertainty (weighted uncertainties at the bottom of Table 3.12). Note again, that by taking the simple sum and not the sum in quadrature, these errors are rather conservative. This results then in the β-delayed neutron branching ratio percentages of 63.2±2.4%, 7.75±1.3%, 22.9±1.6%, 4.10±0.8%, and 1.82±0.5% to the 3.10 MeV, 4.23 MeV, 4.66 MeV, 5.85 MeV, and 6.31 MeV states, respectively, in ^{15}C. Figure 3.8 shows the branching ratio percentage versus detector # obtained from the different detectors (refer to Figure 2.3 to see neutron detector's orientation with respect to the implantation detector).

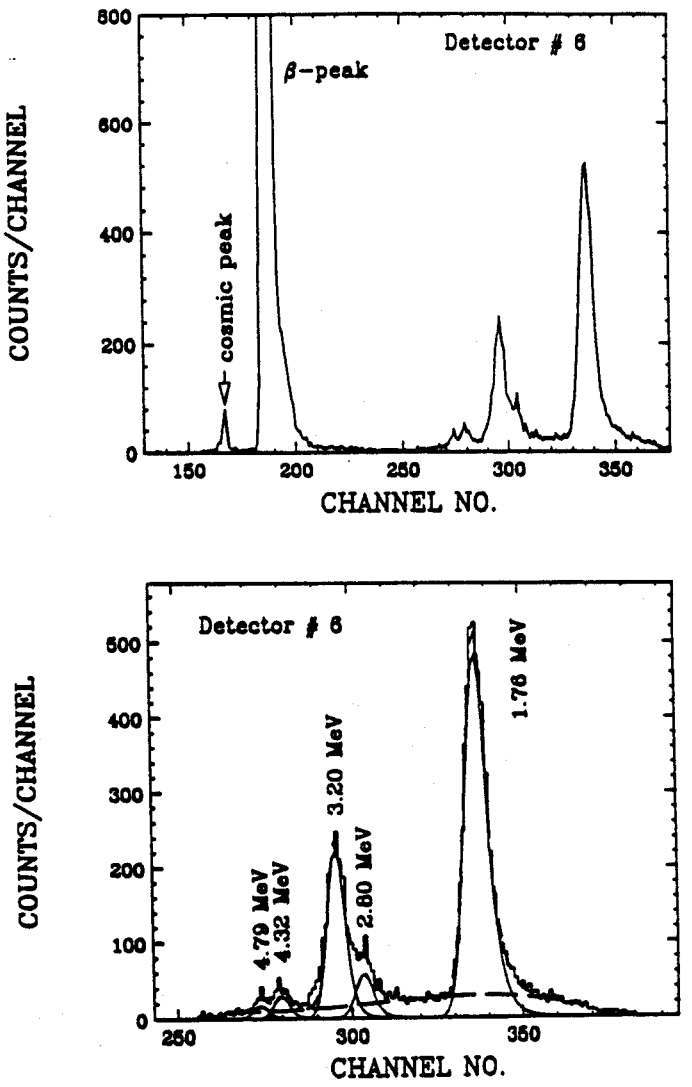

Figure 3.5: Top figure is the raw, unfitted β-delayed neutron time-of-flight spectrum obtained from detector # 6. The x-axis corresponds to time, with the lowest energy neutrons in the highest channel number peak. Shown is the "fast" β-peak and the "cosmic" peak; these are explained in the text. Bottom figure is the above spectrum which has been fitted. The five unfolded β-delayed neutron peaks, with their energies, are shown. The spectrum is not corrected for neutron efficiency. The fits to individual peaks are indicated with solid lines, the background by long dashes, and the sum of all contributions by the short dashes. The fitting procedure is described in the text.

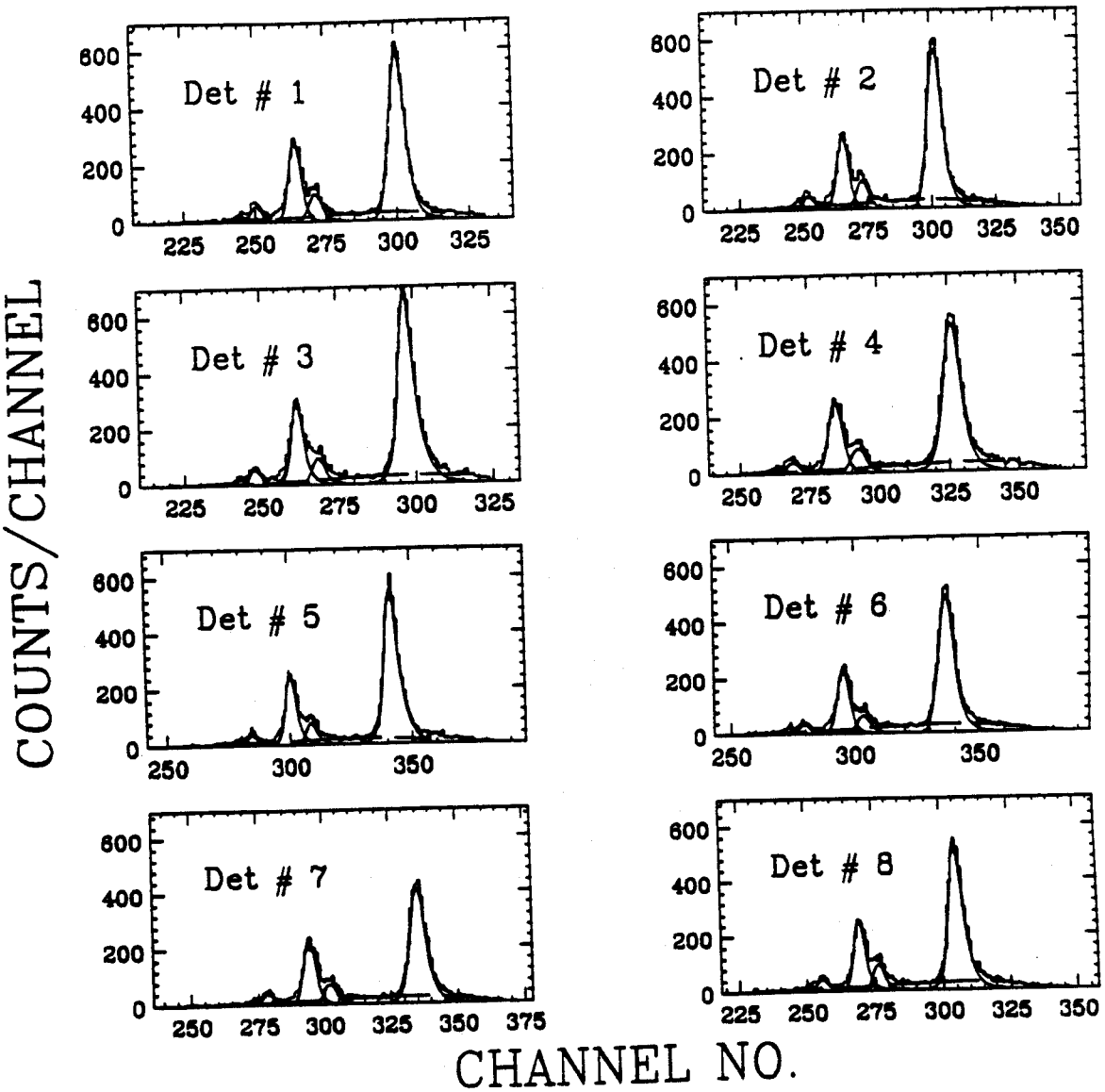

Figure 3.6: Fitted β-delayed neutron time-of-flight spectra obtained from the neutron array detectors # 1 through 8.

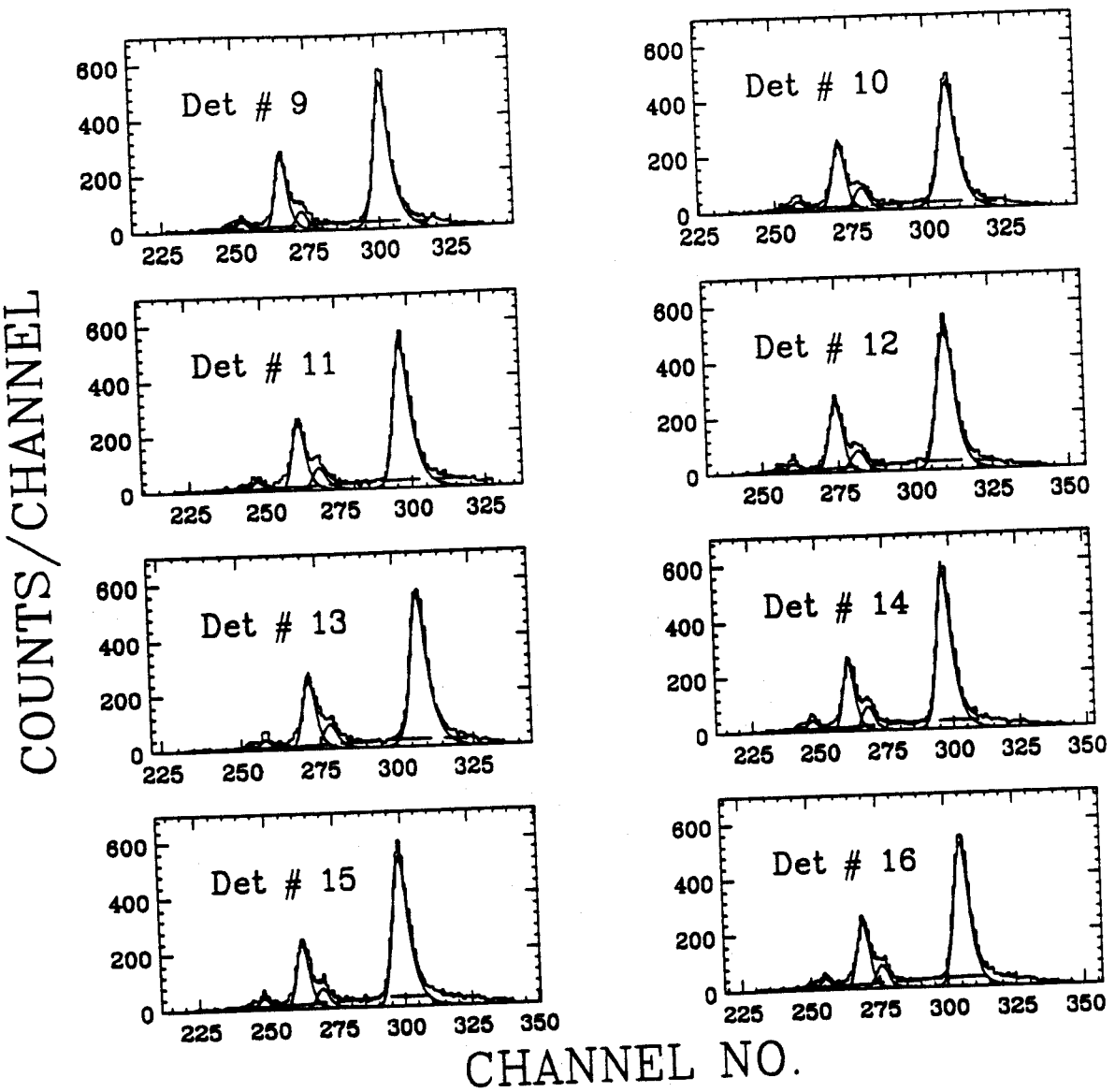

Figure 3.7: Fitted β-delayed neutron time-of-flight spectra obtained from the neutron array detectors # 9 through 16.

Table 3.10: Summary of the calculated neutron energies from the fitted spectra of the sixteen neutron detectors. The flight path was calibrated using the lowest energy neutron peak in the fitted spectra as a standard; this peak represents a 1.759 MeV neutron and corresponds to the known 3.103 MeV state in ^{15}C. The other neutron energies shown below were calculated using this calibrated flight path and their associated peak centroid supplied by the fitting procedure. All neutron energies are in MeV.

Det #	Calibrated flight path (cm)	E_n # 2	E_n # 3	E_n # 4	E_n # 5
1	100.9	2.81	3.20	4.30	4.84
2	100.9	2.79	3.21	4.30	4.70
3	100.4	2.80	3.18	4.33	4.77
4	100.9	2.83	3.22	4.30	4.74
5	100.8	2.79	3.20	4.31	4.77
6	100.7	2.80	3.20	4.32	4.79
7	100.8	2.83	3.21	4.34	4.73
8	100.2	2.82	3.21	4.32	4.76
9	100.4	2.80	3.20	4.27	4.66
10	100.7	2.80	3.22	4.30	4.57
11	100.7	2.81	3.20	4.33	4.77
12	100.5	2.81	3.22	4.36	4.75
13	100.7	2.83	3.22	4.27	4.77
14	100.5	2.82	3.22	4.35	4.75
15	100.9	2.83	3.24	4.32	4.87
16	100.8	2.84	3.22	4.33	4.81
$\overline{x}$	100.7	2.81	3.21	4.32	4.75
σ	0.2	0.02	0.01	0.03	0.07

Table 3.11: Summary of the relative β-delayed neutron branching ratios for the populated states in ^{15}C determined from the results of the sixteen array detector time-of-flight measurements. Listed is the mean and standard deviation for the branching ratio percentages; first, to include the detector # 7 values, and second, to exclude them. All branching ratios are in percent. Errors associated with each detector measurement are dealt with later.

Detector #	3.10 MeV state	4.23 MeV state	4.66 MeV state	5.85 MeV state	6.31 MeV state
1	61.4	8.41	23.7	4.80	1.71
2	63.1	9.03	22.2	4.21	1.41
3	63.2	7.76	22.4	4.72	1.93
4	62.2	8.42	23.2	4.29	1.86
5	63.8	7.37	22.9	3.99	1.92
6	64.9	6.30	23.3	3.59	1.97
7	59.0	8.43	25.5	5.14	1.96
8	61.4	9.05	23.4	4.25	1.87
9	64.4	6.34	23.7	3.42	2.16
10	64.0	7.81	21.8	4.14	2.28
11	63.7	7.97	23.1	3.44	1.87
12	63.5	7.63	23.6	3.52	1.68
13	63.7	8.36	22.8	3.62	1.56
14	62.7	8.23	22.4	4.64	2.07
15	63.8	7.29	22.8	4.57	1.50
16	61.5	8.29	23.3	4.82	2.08
$\overline{x}_{incl.\#7}$	62.9	7.92	23.1	4.20	1.86
$\sigma_{incl.\#7}$	1.48	0.80	0.84	0.56	0.24
$\overline{x}_{excl.\#7}$	63.2	7.88	22.9	4.13	1.86
$\sigma_{excl.\#7}$	1.10	0.82	0.57	0.51	0.25

Table 3.12: Summary of the relative β-delayed neutron branching ratios for the populated states in ^{15}C with their corresponding uncertainties. Also listed is the "weighted" mean and uncertainty for each branching ratio percentage. The details concerning the method used to determine the uncertainties and weighted values are explained in the text. All values are in percentage. Note that the detector # 7 values are not included.

Detector #	3.10 MeV state	4.23 MeV state	4.66 MeV state	5.85 MeV state	6.31 MeV state
1	61.4±5.2	8.41±1.7	23.7±3.7	4.80±1.1	1.71±0.7
2	63.1±5.2	9.03±1.9	22.2±3.6	4.21±1.1	1.41±0.6
3	63.2±5.0	7.76±1.7	22.4±3.3	4.72±1.0	1.93±0.7
4	62.2±5.4	8.42±1.8	23.2±3.8	4.29±1.1	1.86±0.7
5	63.8±5.4	7.37±1.7	22.9±3.8	3.99±1.0	1.92±0.8
6	64.9±5.1	6.30±1.4	23.3±3.7	3.59±1.0	1.97±0.7
8	61.4±5.5	9.05±2.0	23.4±3.9	4.25±1.1	1.87±0.6
9	64.4±5.5	6.34±1.5	23.7±4.0	3.42±1.0	2.16±0.8
10	64.0±5.6	7.81±1.8	21.8±3.8	4.14±1.2	2.28±0.9
11	63.7±5.4	7.97±1.8	23.1±3.9	3.44±0.9	1.87±0.8
12	63.5±5.2	7.63±1.7	23.6±3.8	3.52±1.0	1.68±0.6
13	63.7±5.5	8.36±1.9	22.8±3.9	3.62±1.0	1.56±0.6
14	62.7±5.6	8.23±1.8	22.4±3.8	4.64±1.3	2.07±0.8
15	63.8±5.5	7.29±1.7	22.8±3.8	4.57±1.2	1.50±0.7
16	61.5±5.6	8.29±1.9	23.3±3.9	4.82±1.3	2.08±0.8
$\overline{x}_{weighted}$	63.2±1.4	7.75±0.5	22.9±1.0	4.10±0.3	1.82±0.20

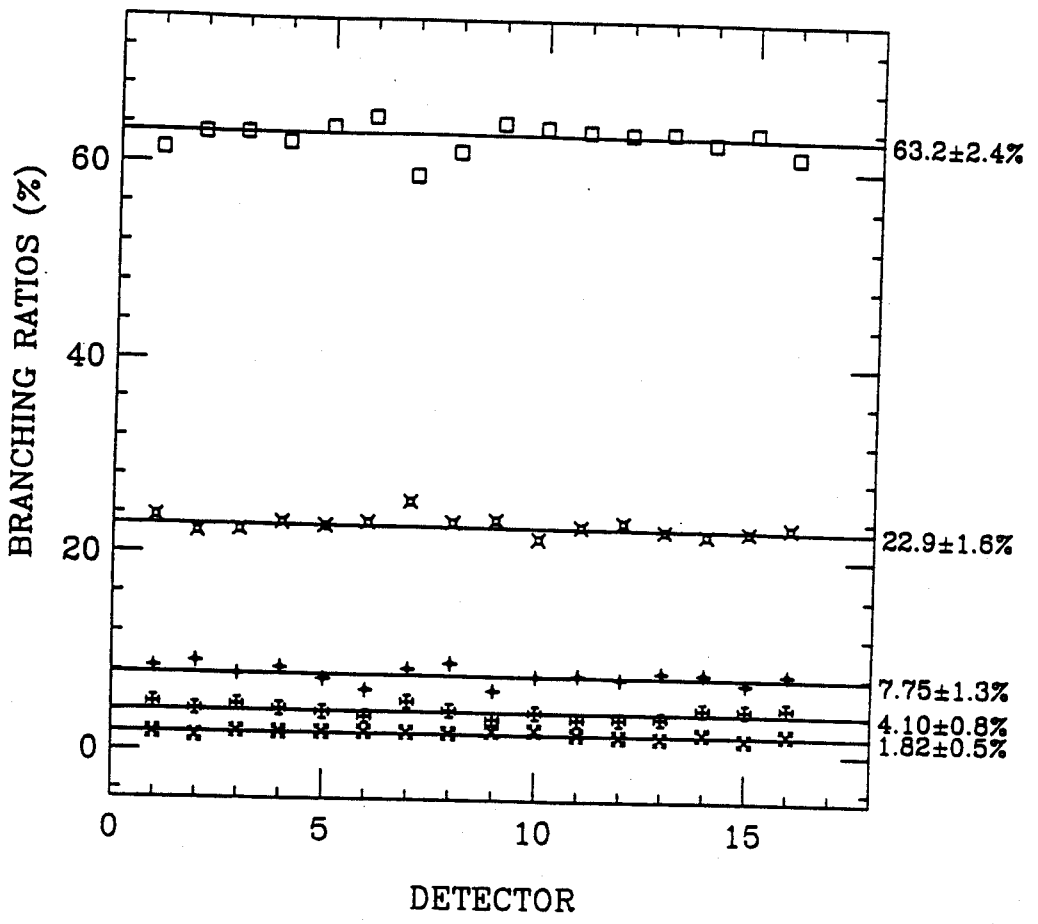

Figure 3.8: The β-delayed neutron decay branching ratios obtained from the different array detectors. The solid lines and values on the right are the weighted averages obtained for each of the five percentages from the detector measurements; note that the detector # 7 values are shown here but its values were not used in calculating the weighted averages.

3.4.2 Other Decay Channels for ^{15}B β-Delayed Neutron Emission

A β-decay branch leading to single neutron emission via the first excited state of ^{14}C at 6.08 MeV (compared to the five observable peaks resulting from decays via the ^{14}C ground state) requires the excitation energy of ^{15}C to be at least 7.31 MeV and should result in distinct neutron energy peaks[15]. No evidence for such peaks could be found in any of the individual sixteen detector neutron time-of-flight spectra. In order to look more closely for evidence of any additional neutron peaks, the results obtained from all the neutron detectors were summed. This summation first required that the neutron time-of-flight measurement be converted into an neutron energy measurement in software; this was necessary since the different detectors had unique time calibrations and a simple summing of time-of-flight spectra would not add the neutron peaks properly. By converting each detector measurement to an energy measurement, all detectors were put on equal footing and could then be added together. Figure 3.9 shows the spectrum obtained by adding all sixteen detector results together.

Several points need to be made concerning this summed energy spectrum. First, all sixteen detectors contributed to this spectrum (including detector # 7). Second, since the purpose of this spectrum was to find evidence of additional neutron peaks (*not* to determine branching ratios), the threshold setting for each detector was set as low as possible, essentially the "intrinsic" threshold of the detector (estimated to be a neutron energy cut-off of about 0.7 MeV). Referring to Figure 3.9, there appears to be no new neutron peaks to indicate population of any state in ^{15}C above 7.31 MeV; the five neutron peaks present correspond to the ^{15}C states already identified from

[15]It should be noted that the available phase space for the electron and neutrino during β-decay behaves roughly as the fifth power of the decay energy, so population of high level states in ^{15}C is diminished due to this effect. It should also be noted, however, that a "good" overlap of initial and final nuclear wave functions can result in a high-lying state being populated more favorably than "just accounting for phase space" would predict.

the individual detector spectra. It should be noted however that with the 0.7 MeV neutron cut-off, states populated in ^{15}C below 8.0 MeV and decaying via the first excited state of ^{14}C (^{15}C states between 7.31 MeV and 8.0 MeV) would produce neutrons with energies too low in energy to be detected. It should also be noted that if a state in ^{15}C between 7.31 and 8.0 MeV was populated, it would also be possible for this state to decay via the ground state of ^{14}C, yielding neutrons with energies between 6.1 and 6.8 MeV. These neutrons would be detectable, yet none were observed.

For the population of states in ^{15}C above 9.40 MeV, two neutron emission via the ground state of ^{13}C is possible. One might expect that the population of states in ^{15}C this high in energy would be quite inhibited due to the severely decreased available phase space for the electron and neutrino; yet here too, good initial and final nuclear wave overlap can result in favorable feeding to these high lying states. The probability established for the β-delayed two neutron emission of ^{15}B was a limit of $P_{2n} < 1.5\%$ by Dufour *et al.* in 1984 [Du84] and a more recent measurement of $P_{2n} = 0.4 \pm 0.2\%$ by P.L. Reeder *et al.* in 1990 [Re90]. In the present work, an attempt was made to observe ^{15}B β-delayed two neutron emission using the neutron detector array by looking for neutron coincidences in detector pairs. This involved creating two dimensional spectra and plotting the neutron time-of-flight measurement for one detector vs. the neutron time-of-flight measurement of another detector. Figure 3.10 shows the fifteen spectra obtained by plotting detector # 6 vs. the other fifteen detectors; these are the result of approximately 5 million ^{15}B decays.

Using the upper limit of 1.5% for two neutron emission, one would expect less than one two-neutron event per detector pair given the total number of ^{15}B nuclei that actually decayed at the center of the array. Accounting for detector solid angle and neutron detection efficiency, a 1.5% two neutron decay branch would result in

about 0.6 events (less than this for neutrons below 1.8 MeV) per detector pair for the given 5.083 million ^{15}B decays observed. Referring to Figure 3.10, random coincidence events are observed at a level of about 3–4 per detector pair. The heavy horizontal and vertical lines in each spectrum correspond to a coincidence event between the detection of a β-particle in one detector and a neutron in the other (most of these neutrons are the five identified peaks). Notice that the neutron detectors (#'s 5 and 7) adjacent to detector # 6 show neutrons that scattered from one detector to its neighbor; this is observed by the diagonal pattern in these two spectra. Since the neutron detector array was thus not adequate for measuring the two neutron emission decay branch, the present work adopts the P.L. Reeder *et al.* [Re90] value of 0.4±0.2% for this branch in the determination of the ^{15}B β-decay branching ratios.

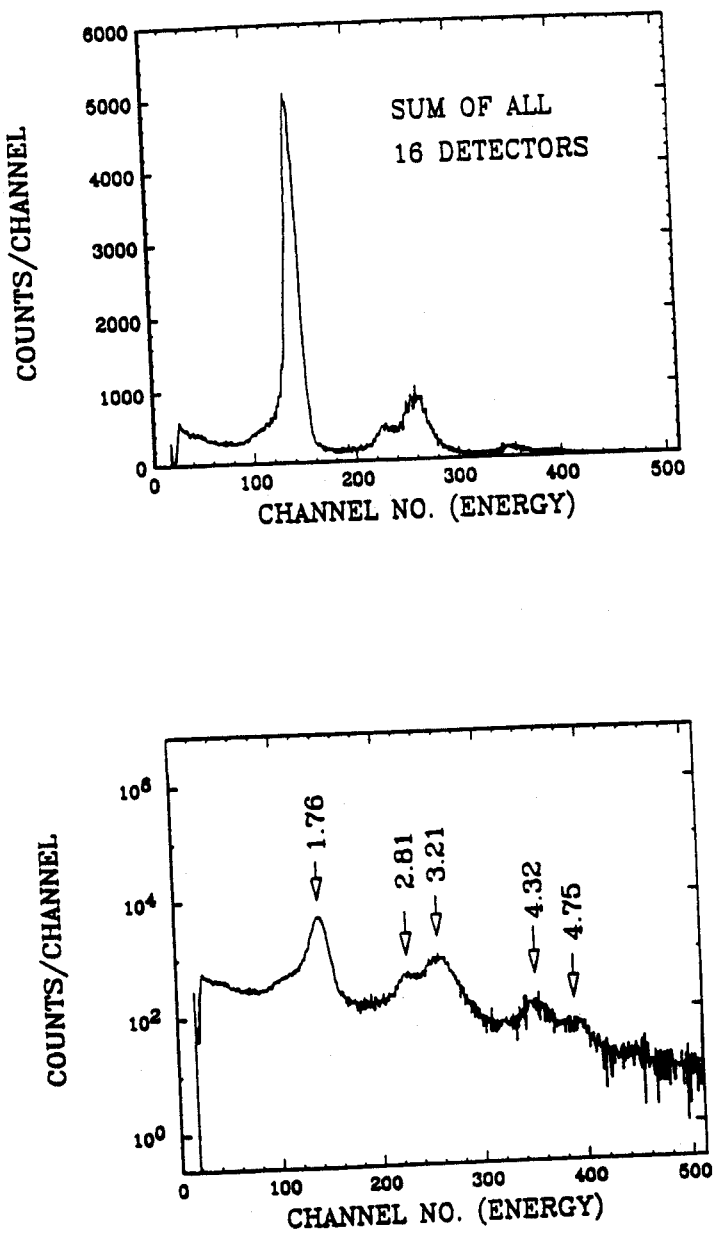

Figure 3.9: Neutron energy spectrum generated from the sixteen neutron detector time-of-flight measurements. Top figure is the energy spectrum with a linear y-axis, bottom figure is the same spectrum with a log y-axis. Note the evidence of only five β-delayed neutron peaks.

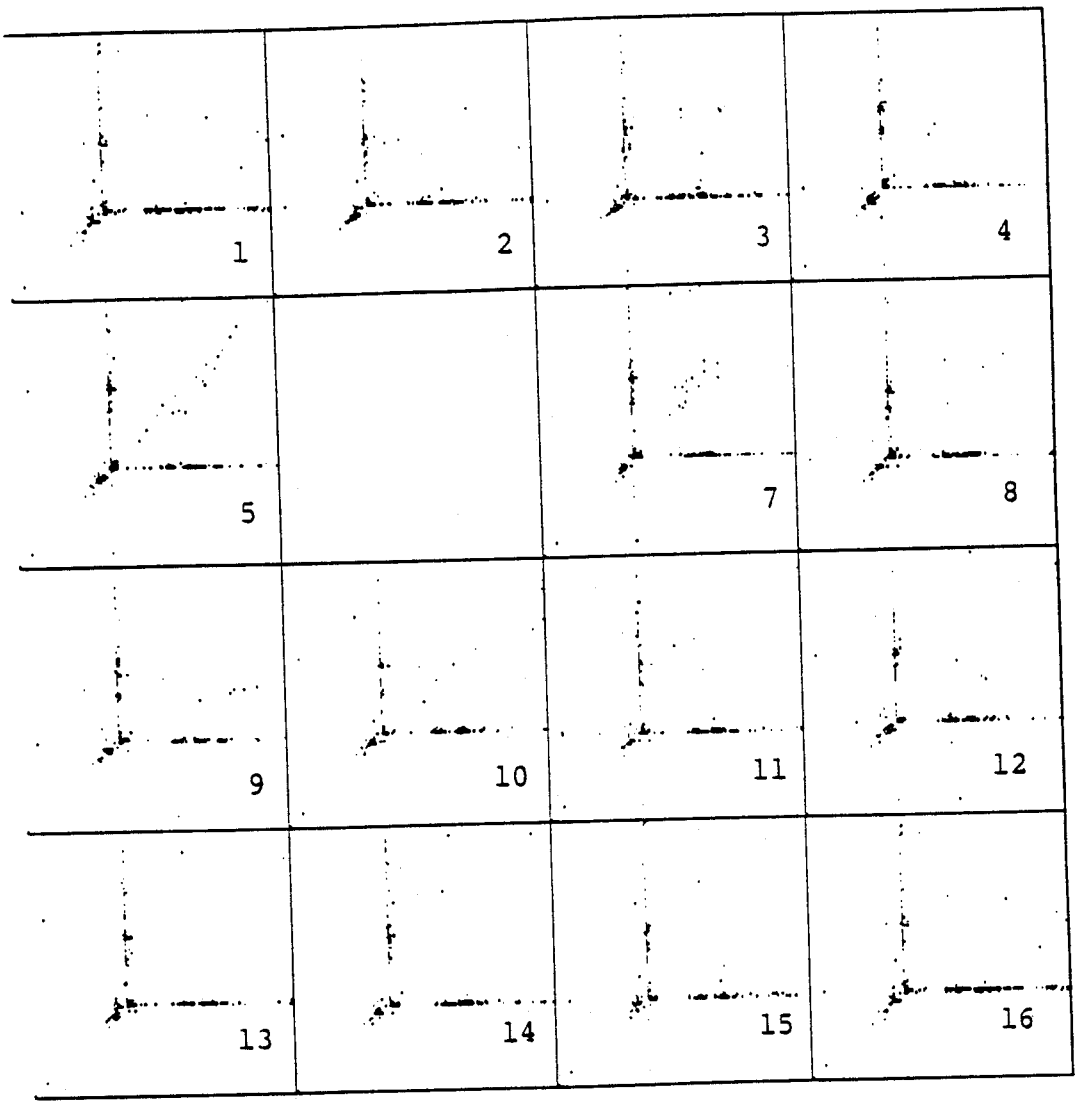

Figure 3.10: Two dimensional spectra showing the neutron time-of-flight measurement for detector #6 (x-axis) vs. the neutron time-of-flight measurement for the fifteen other detectors (y-axis, and numbered for detector number). These spectra were used to look for two neutron coincidence events and evidence of ^{15}B β-delayed two neutron emission via the ground state of ^{13}C.

3.5 The ^{15}B β-Decay Branching Ratios

Having measured the 0.46±0.08% ^{15}B β-decay branch to ^{15}C bound states, adopting the value of 0.4±0.2% for ^{15}B two neutron emission [Re90], and having no evidence that any ^{15}C state other than those represented by the five observable neutron peaks in the array detector time-of-flight spectra were populated, it is therefore concluded that 99.14±0.28% of the ^{15}B β-decays populate the five lowest negative parity states in ^{15}C (the five observable neutron peaks). Table 3.13 contains a summary of the deduced branching ratios.

Before discussing the values in this table, it should be mentioned here that a recent measurement of delayed neutron emission probabilities of neutron-rich nuclides from Li to Al, including a value of $P_{1n} > 77.3\%$ for ^{15}B, was made by Reeder *et al.* [Re91] using the Los Alamos National Laboratory time-of-flight isochronous spectrometer (TOFI) and a polyethylene-moderated neutron detection system which included forty ^{3}He proportional tubes [16]. The TOFI system measured the A, Z, and Q of each neutron-rich ion and the decay neutrons were observed by means of a delayed coincidence technique. Figure 3.11 shows the efficiency curve provided by Reeder *et al.* for their neutron detection system. The solid circles in this figure are the Monte-Carlo calculated efficiencies for the detector geometry, having values that range from 64% for 0.1 MeV neutrons to 42% for 3.0 MeV neutrons. Also shown in this figure are measured efficiencies for ^{9}Li, ^{16}C, and a PuBe source (open circles). The efficiencies for the ^{9}Li and ^{16}C were calculated from the data obtained during the measurement and the previously known P_n values. Since the delayed neutron and PuBe sources are not monoenergetic, the experimental efficiencies are valid for the average energy of the known spectra. In their $P_{1n} > 77.3\%$ determination of ^{15}B, they assumed a

[16] This type of neutron detection system had a high efficiency for the detection of a broad energy range of neutrons, although it provided no specific information on the neutron energy.

60% detection efficiency for the delayed neutrons (for an assumed average energy of ≈0.5 MeV). Using the branching ratios established in the present work, the average delayed neutron energy from ^{15}B is much higher, 2.4 MeV; using the efficiency curve in Figure 3.11 this corresponds to a 47% neutron detection efficiency. In their published results, Reeder *et al.* [Re91] pointed out that a 47% assumed efficiency for the delayed neutrons from ^{15}B would change their P_{1n} to 99%, *in agreement* with the previous measurement of Dufour *et al.* [Du84] of $P_{1n} > 93.5\%$ and the $P_{1n} = 99.14\%$ adopted by the present work.

Recently the neutron detector array was used in another experiment at the NSCL to study the decay of ^{18}N (Görres, *et al.* - PAC91011). For calibration purposes, a ^{17}N beam was deposited into the implantation detector during a 16.48 s beam on period and its decay was observed during a 15.50 s beam off period. ^{17}N is a β-delayed neutron emitter, having a half-life of 4.173 s and emitting neutrons with kinetic energies/absolute branching ratios of 0.383 MeV/38.0±1.3%, 1.172 MeV/50.1±1.3%, and 1.702 MeV/6.9±0.5% [Aj86]. Using this information, the *absolute* efficiency of a neutron detector could be determined for the neutrons with these kinetic energies (particularly the 1.702 MeV neutrons), and from this an *absolute* branching ratio could be estimated for the ^{15}B decay which feeds the lowest negative parity state in ^{15}C (this produces neutrons with the kinetic energy of 1.759 MeV). Although, of course, (1) the experimental conditions under which ^{15}B and ^{17}N decays were not identical, and (2) the neutron energies (1.702 and 1.759 MeV) were not exactly the same. However, the threshold settings of the neutron array could be duplicated and the neutron energies differed by only 3.2%.

Figure 3.12 shows the decay curve obtained for the ^{17}N implantation (^{19}O was an impurity) from which the number of ^{17}N atoms that decayed during the beam off period could be determined. Figure 3.13 contains the ^{17}N β-delayed neutron

time-of-flight spectrum obtained from neutron array detector # 6; notice that the 1.702 MeV and 1.172 MeV neutrons are present, however the detector was not able to observe the 0.383 MeV neutrons. From the decay curve it was determined that 1.479E6 ^{17}N atoms decayed; as a result of these decays, 127 neutrons at 1.702 MeV were observed by detector # 6. Adjusting for the known branching ratio of 6.9±0.5% to this state, an absolute detector efficiency of (1.24±0.16)E-3 was obtained; this compared to the efficiency of (2.14±0.26)E-3 obtained using the PuBe source (the discrepancy among these two values will be discussed in the next paragraph). As a result of 4.905E6 ^{15}B atoms decaying (from the present work), 4080 neutrons at 1.759 MeV were observed by detector # 6. Normalizing this number of neutrons by the 1.24E-3 efficiency, gives an *absolute* branching ratio of 67.1±7.7%, compared to the 64.9±5.1% *relative* branching ratio determined for this detector. This agrees reasonably well, especially when it is considered most likely that the absolute detector efficiency for 1.759 MeV neutrons would be slightly higher than it is for 1.702 MeV neutrons, and this would give even closer agreement among the absolute and relative branching ratios. In addition, recall from earlier in this chapter that array detector # 7 showed abnormally low detection efficiency for the lowest energy (≈1.76 MeV) β-delayed neutrons from the decay of ^{15}B. This detector did not exhibit a similar low efficiency for the ^{17}N decay; its detection efficiency for the 1.172 MeV and 1.702 MeV neutrons from the decay of ^{17}N appeared to be very similar to that of detector # 6. This would very likely indicate that the abnormally low efficiency observed for the 1.76 MeV ^{15}B neutrons could not be soley attributed to the location of detector # 7 but rather some problem in the electronics.

A rather large discrepancy is observed among the *absolute* efficiency values obtained for detector # 6 from the ^{17}N measurement ((1.24±0.16)E-3) and the PuBe neutron source measurement ((2.14±0.26)E-3). It is noted however, that there

is very good agreement among branching values obtained for the ^{15}B β-decay to the 3.103 MeV state in ^{15}C derived from these two separate measurements; the 67.1±7.7% value could be properly termed an "absolute" branching ratio, whereas the 64.9±5.1% value a "relative" branching ratio. The disagreement among the absolute efficiencies lies in the 119.5 msr solid angle which was choosen for the array detector element in Eq. 2.2; this selected solid angle is the result of assuming the entire area of the detector (entire 157 cm tube-to-tube length) is active. Closer agreement among the efficiencies is obtained if a smaller solid angle is assumed for the array element; for example instead of assuming the active area of the detector is from tube-to-tube, one assumes the detector active area is from frame-to-frame[17], this would result in a solid angle of approximately 100 msr. The advantage of determining "relative" branching ratios, as was done in the present work, is that the solid angle cancels out in the calculated branching ratios and the *same* ratios are obtained regardless of the solid angle value. Changing the array element solid angle value in Eq. 2.2 to bring closer agreement among the efficiencies however would result in larger discrepancies among the PuBe source and the calculated Monte-Carlo values shown in Table 2.3. Discrepancy among these values would appear to indicate that the entire PuBe time-of-flight spectra shown in Figures 2.7 and 2.8 were "riding-on" a background which would inflate the PuBe determined efficiency values. This background could have been estimated if a "shadow bar" was used; the purpose of a bar is to mask neutrons that travel directly from the source to the detector, so any events observed in the spectra are attributed to neutrons that did not follow this direct path (scattered off surroundings) or any other source of background. Thus agreement among the 67.1±7.7% absolute and 64.9±5.1% relative branching ratio values would appear to indicate that the relative β-decay branching ratios determined for ^{15}B from the PuBe source efficiencies are

[17]The frame corresponds to the mounting hardware which supports the 16 array elements around the implantation detector.

not significantly effected by this background component (it *cancels out* in the values determined for the relative branching ratios), however one must be very cautious in using the PuBe source to determine *absolute* branching ratios, and additional work must be conducted to determine the actual background attributed to this source.

Referring to Table 3.13, the energies of the ^{15}C states deduced from this work (recall that the 3.103 MeV state was fixed as a calibration), the known ^{15}C states [Aj91], the β-branching ratios, and the deduced $logft$ values are listed. The ft values were calculated using a half-life of 10.3±0.2 ms, the measured branching ratios (BR), a Q_β of 19.1 MeV [Aj91], in the expression:

$$ft = \frac{f(Q_\beta - E_x)t_{1/2}}{BR} \tag{3.15}$$

The statistical rate function $f(Q_\beta - E_x)$ was calculated with the method of Wilkinson and Macefield [Wi74]. Recalling from Chapter I the predictive ability of $logft$ values, it is reasonably clear that the five neutron peaks observed in the present work all represent allowed decays to negative parity states in ^{15}C ($J^\pi = \frac{3}{2}^-$ for ^{15}B, [Aj91]); decays to the ground state and first excited state of ^{15}C (both positive parity states states) represent first-forbidden decays. In addition, the 62.8%, 7.7%, 22.8%, and 4.1% observed branches correspond to the (E_x(MeV), J^π) 3.103, $\frac{1}{2}^-$; 4.220, $\frac{5}{2}^-$; 4.657, $\frac{3}{2}^-$; and 5.866, $\frac{1}{2}^-$ known ^{15}C states, respectively. The state observed at 6.31±0.07 MeV probably represents the 6.358±0.006 MeV ^{15}C state, however it may be the 6.417±0.006 MeV state; it could also be a mixture of both. The literature lists only possible J^π assignments for these latter states; since the present work suggests this to be is an allowed transition, this would restrict the state's J^π to be $\frac{1}{2}^-$, $\frac{3}{2}^-$, or $\frac{5}{2}^-$.

Table 3.13: Neutron energies, measured ^{15}C states (*this work*), known ^{15}C states [a], β branching and $logft$ values in ^{15}B decay. All energies are in MeV.

E_n	^{15}C (E_x) (*this work*)	^{15}C (E_x, J^π) (Ajzenberg-Selove [a])	I_β (%)	$logft$
4.75±0.07	6.31±0.07	6.358±0.006 $\frac{5}{2}^-, \frac{7}{2}^+, \frac{9}{2}^+$ 6.417±0.006 $\frac{3}{2}^-, \frac{5}{2}^-, \frac{7}{2}^-$	1.8±0.5	5.41±0.15
4.32±0.03	5.85±0.04	5.866±0.008 $\frac{1}{2}^-$	4.1±0.9	5.10±0.10
3.21±0.01	4.66±0.01	4.657±0.009 $\frac{3}{2}^-$	22.8±1.6	4.56±0.04
2.81±0.02	4.23±0.02	4.220±0.003 $\frac{5}{2}^-$	7.7±1.3	5.13±0.10
1.759 (calibration)	3.103 (calibration)	3.103±0.004 $\frac{1}{2}^-$	62.8±2.4	4.34±0.02
(neutron bound states in ^{15}C)	—	0.740 $\frac{5}{2}^+$ g.s. $\frac{1}{2}^+$	0.46±0.08	—

[a] Ref. [Aj91]

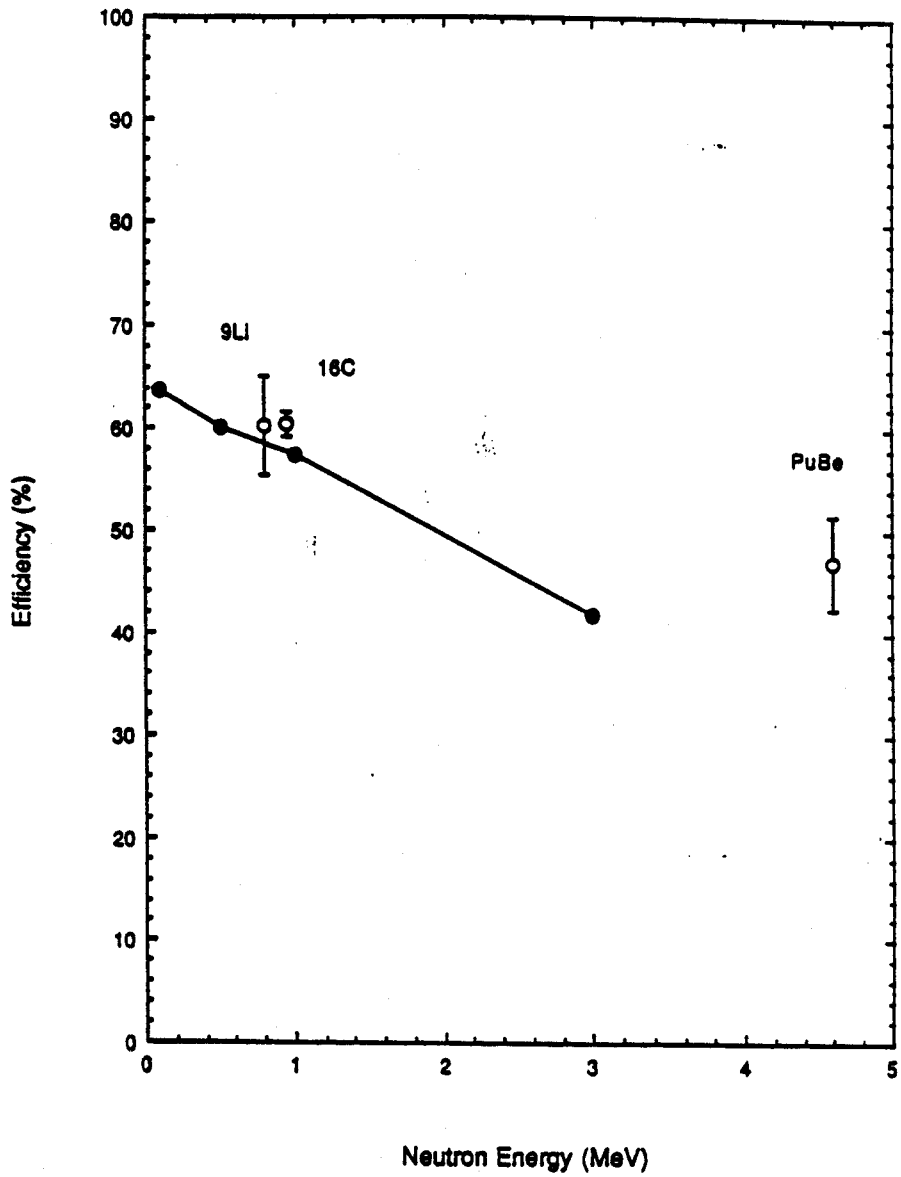

Figure 3.11: Efficiency curve for the polyethylene-moderated neutron detection system used by Reeder *et al.* [Re91] in their recent measurement of the ^{15}B P_{1n}. Calculated Monte-Carlo efficiencies are represented by the solid circles and experimentally determined efficiencies by the open circles. See text for a detailed explanation.

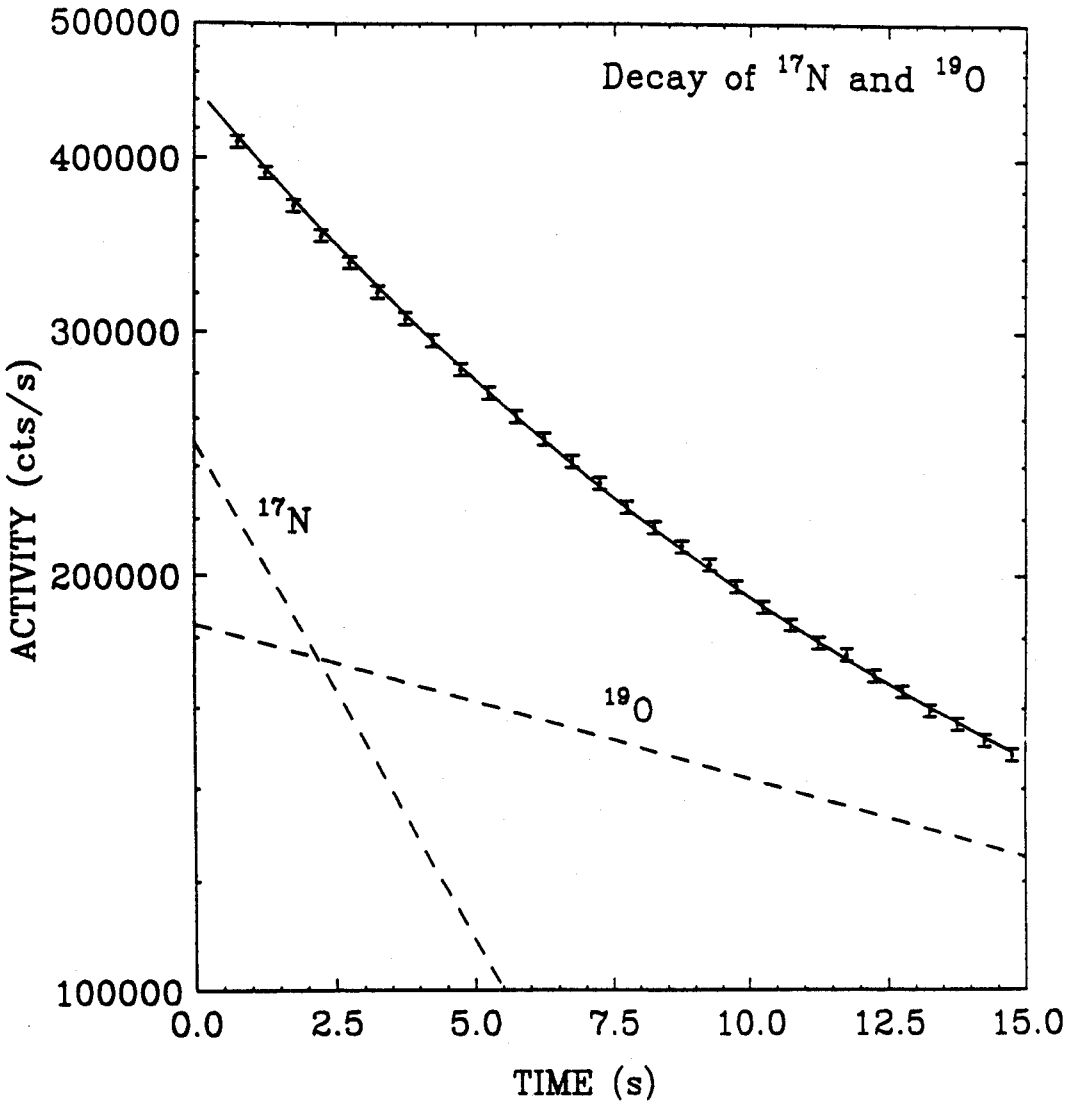

Figure 3.12: Experimental decay curve for ^{17}N inclusive β-emission; ^{19}O was an impurity. The solid line corresponds to a two-component fit, the reduced chi-square for this fit was 0.5.

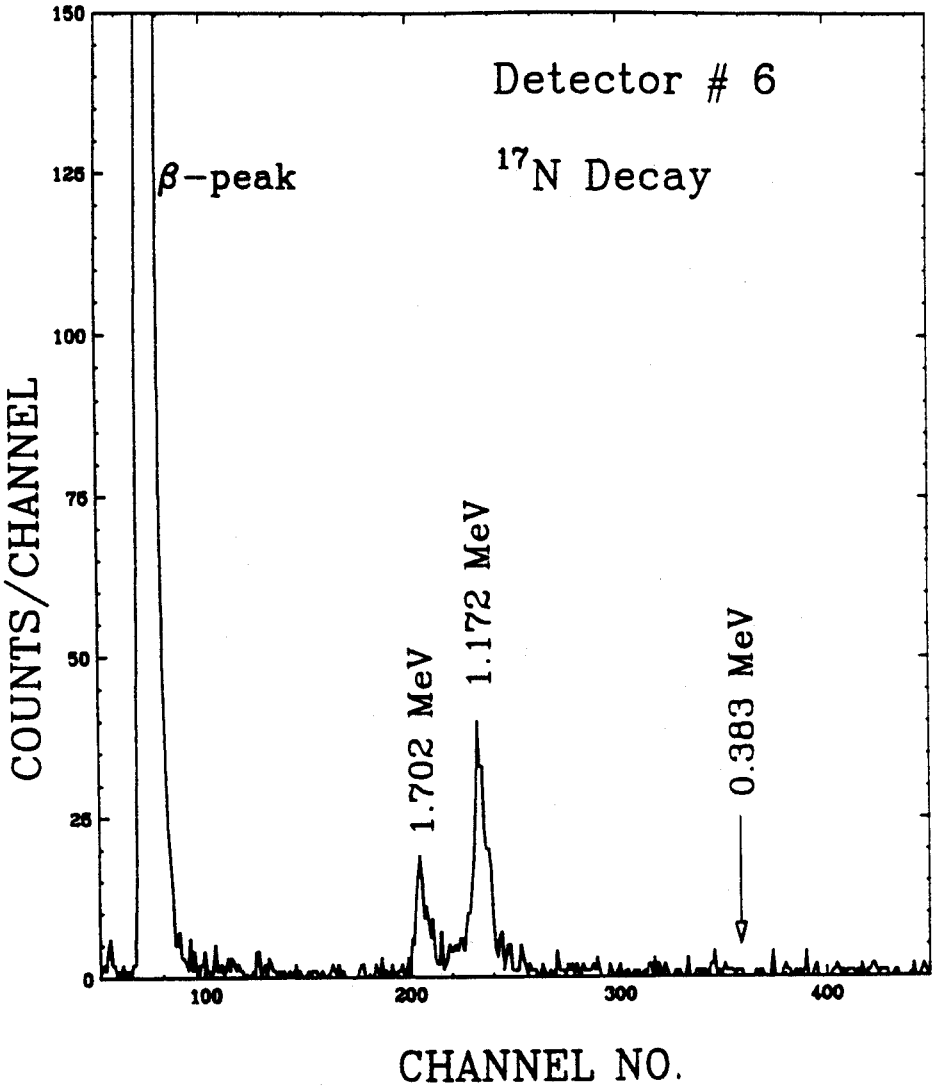

Figure 3.13: Time-of-flight β-delayed spectrum obtained for the decay of ^{17}N from neutron array detector number # 6. Shown are the "fast" β-peak and the 1.702 MeV and 1.172 MeV neutron peaks. Note that the detector was not able to detect the 0.383 MeV neutrons from the decay of ^{17}N, however the spectrum location where they would be expected is shown.

Chapter 4

Discussion – Comparison to Theoretical Predictions

In this chapter, the experimentally determined ^{15}B β-decay properties from the present work are compared to theoretical shell-model calculations. Before the details of the ^{15}B specific shell-model calculations are examined and compared to the experimental results, a general discription of the nuclear shell-model will be presented.

4.1 The Nuclear Shell-Model

Nuclear theorists have constructed a nuclear shell-model somewhat after the atomic theorists constructed their atomic shell picture. In the atomic theory the energy shells of increasing energy are filled with electrons consistent with the requirements of the Pauli principle. Filling these shells, an inert core is generally obtained and the valence electrons determine the chemical properties of the atom. The atomic shell-model has been able to predict an impressive list of atomic properties. When attempting to create a nuclear model based on "shells", some major differences become apparent when compared to the atomic model. First, in the atomic model the interaction potential is the result of a central Coulomb field from the nucleus; for the nuclear case, the nucleons have to move in a potential that they themselves create (this major

tenet of the nuclear shell-model was already brought to light in the opening of Chapter I).

Choosing the correct form of this "self generated" potential was very important if a good nuclear model was to be obtained. A realistic nuclear model would be able to successfully reproduce physically observed quantities, for example, first and foremost the nuclear *magic numbers.* It is observed that specific numbers of protons or neutrons create obviously more stable nuclei; these magic numbers are Z = 2, 8, 20, 28, 50, and 82 and N = 2, 8, 20, 28, 50, 82, and 126. The significance of these numbers in a shell-model is that they represent the exact filling of major nuclear shells, analogous to the stability of the noble gases caused by the exact filling of atomic shells by electrons. Several examples of the significance of the magic numbers are the enhanced binding energy of the alpha particle (Z = N = 2; being *doubly magic*), the element tin (Z = 50) having the largest number (10) of stable isotopes in nature, and the element lead (Z = 82) ending four long radioactive decay chains.

Two nuclear potentials that were considered are the infinite potential and the harmonic oscillator. Neither of these potentials alone was successful in approximating the real nuclear potential, however an intermediate form which combined the two, known as a *Woods-Saxon* potential [Wo54] was better able to approximate the true potential. The Woods-Saxon potential can be written:

$$V(r) = \frac{-V_0}{1 + exp[(r - R)/\alpha]} \tag{4.1}$$

where R is the nuclear radius (taken to be $1.25A^{\frac{1}{3}}$), V_0 is the well depth of the nuclear potenial (usually on the order of ≈50 MeV), and α is the nuclear *skin thickness* or distance over which the nuclear charge density falls from 90% to 10% (typically ≈2.3 fm).

The left side of Figure 4.1 (labeled Intermediate form) shows the energy levels

resulting from the model nucleus using the Woods-Saxon potential. Notice that this potential successfully predicts the magic numbers (numbers in the circles) for the lower energy levels (2, 8, and 20), however as the energy levels increase the calculation fails to predict the correct numbers. Again following the atomic shell-model, a nuclear *spin-orbit* potential can be added. The spin-orbit potential results in the two-fold splitting (except for $l = 0$ where there is no splitting) of energy levels with the same orbital angular momentum due to the intrinsic spin s $= \frac{1}{2}$ of the nucleon. For example, the nuclear p energy level with orbital angular momentum $l = 1$, will be split into two orbitals, one with a total angular momentum of 1/2 ($p_{1/2}$) and the other with a total angular momentum of 3/2 ($p_{3/2}$). It should be noted that each orbital is specified by three labels: a single letter s, p, d, f, etc. which stands for l = 0, 1, 2, 3, etc.; a subscript to denote the total angular momentum, j, of a single particle in that orbital; and a numerical prefix that counts the number of levels with that l value (for example, $1p$ means the lowest p state). This addition results in the successful prediction of all the known magic numbers; this is shown on the right side of Figure 4.1 (labeled Intermediate form with spin orbit). This nuclear shell-model not only successfully predicts all the magic numbers but is also able to predict other nuclear properties such as spin-parity assignments, nuclear magnetic dipole moments, and electric quadrupole moments.

In its most extreme limit (known as the *extreme independent particle model*) the nuclear shell-model predicts that the last single unpaired nucleon determines the properties of the nucleus; the other nucleons form an inactive core which create the nuclear self potential. Despite its drastic simplicity, this extreme model is successful in predicting the properties of numerous nuclei, particularly when the single unpaired nucleon is one less or one more and the other nucleons correspond to the filling of a major shell (for example $^{15}_{7}N_8$, $^{17}_{8}O_9$, and $^{41}_{20}Ca_{21}$). For other nuclei, it is a next better

approximation to consider all the nucleons in an unfilled shell. For a nucleus such as $^{43}_{20}Ca_{23}$ the extreme model would consider *only* the single unpaired 23rd neutron, where a more complete model would consider the interaction of all three valence neutrons.

Present day shell-model calculations, such as the one used to predict the β-decay properties of ^{15}B, are generally quite rigorous and their complexity should not be underestimated by the very basic explanation of the shell-model which was just provided. Generally three steps, all of which are related to each other, must be carried out before a shell-model calculation can be performed which include (1) the choice of a single-particle basis, (2) selection of an active space, and (3) the derivation of an effective interaction. A brief discussion of these steps will now be presented, and a more complete, clear discussion of these steps can be found in "Introductory Nuclear Physics" by S.S.M. Wong [Wo90].

Referring to Figure 4.1, for a nucleus such as $^{15}_{5}B_{10}$, with 5 protons and 10 neutrons, 3 of the protons occupy the $1p$ shell (made up of the $1p_{3/2}$ and $1p_{1/2}$ orbitals), lying outside the closed $1s$ shell (made up of the $1s_{1/2}$ orbital); 2 of the neutrons occupy the $1d2s$ shell (made up of the $1d_{5/2}$, $2s_{1/2}$, and $1d_{3/2}$ orbitals), lying outside the closed $1p$ shell. The protons occupying the "proton" $1s$ shell and the neutrons occupying the "neutron" $1s$ shell are never excited and form an inert core (a ^{4}He core) and the single-particle states they occupy do not have to be included in an active space. Likewise, single-particle states very high above the valence nucleons can be ignored in the active space if interest is primarily in the low-lying excited states of the nucleus (below approximately 15 MeV). All that remains then are the valence nucleons to form the active space from which nuclear wave functions can be approximated; these single-particle wave functions are then used to construct a complete many-body basis state. For ^{15}B, the shell-model calculations discussed in the next section used the

complete *psd* model space, in which the $1p_{3/2}$, $1p_{1/2}$, $1d_{5/2}$, $2s_{1/2}$, and $1d_{3/2}$ orbitals are all included in the active space.

Single-particle wave functions, $\phi_i(\vec{r}_i)$, are taken as eigenfunctions of a single-particle Hamiltonian, $h(\vec{r}_i)$:

$$h(\vec{r}_i)\phi_k(\vec{r}_i) = \epsilon_k \phi_k(\vec{r}_i) \tag{4.2}$$

where ϵ_k is the single-particle energy. A many-body Hamiltonian is then generated from two parts: one, the single-particle Hamiltonian and two, a residual two-body interaction term, $V(\vec{r}_i, \vec{r}_j)$, which accounts for nucleon-nucleon interactions:

$$H = \sum_{i=1}^{A} h(\vec{r}_i) + \sum_{i \neq j=1}^{A} V(\vec{r}_i, \vec{r}_j) \tag{4.3}$$

The matrix elements of H in the many-body basis states can then be expressed as a sum of two terms:

$$H_{jk} = \delta_{jk} \sum_{n=1}^{A} \epsilon_n + V_{jk} \tag{4.4}$$

The first term of Eq. 4.3 is constructed out of eigenfunctions of $h(\vec{r}_i)$ and the second term is the contribution to the Hamiltonian matrix element from the residual interaction.

An effective many-body Hamiltonian can be generated semi-empirically from known experimental data. The single-particle energy term is obtained from binding energy differences between filled-shell and single-particle/single-hole nuclei, and the residual two-body term is obtained by fitting experimental data available in the mass region of the active model space. The semi-empirical methods used to determine the effective interactions for the ^{15}B shell-model calculations are outlined in the next section.

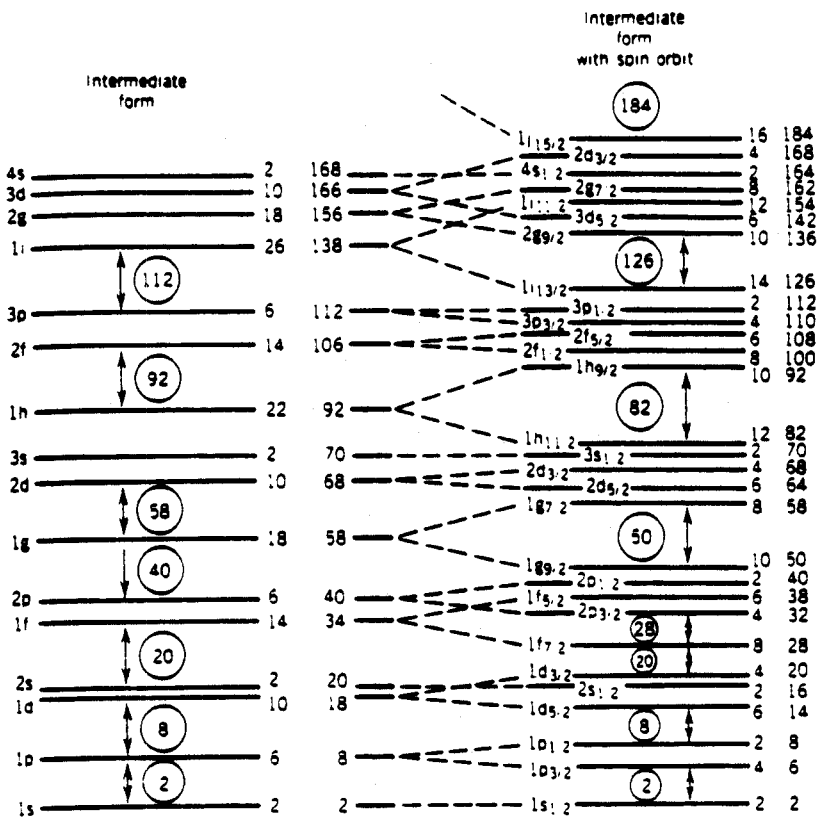

Figure 4.1: At the left are the energy levels calculated using the Woods-Saxon potential (Eq. 4.1) alone (Intermediate form). At the right are the energy levels calculated when the spin-orbit potential is included (Intermediate form with spin orbit); notice the spin-orbit interaction splits the levels with $l > 0$ into two new levels. To the right of each energy level is, first the individual nucleon capacity of that level and, second the cumulative number of nucleons up to that level. The inclusion of the spin-orbit potential results in the magic numbers (shown in the circles) being exactly reproduced. From K. Krane, *Introductory Nuclear Physics* (New York: John Wiley and Sons, 1987).

4.2 Shell-Model Calculations for ^{15}B

Shell-model calculations to predict Gamow-Teller β-decay strengths for mass 15 were carried out in the complete *psd* model space, within the framework of a spherical shell-model formalism [Wi83] by B.A. Brown [Br90]. The Millener-Kurath-Wildenthal (MKW) interaction [Cu86] was used in which the $1p_{3/2}$, $1p_{1/2}$, $1d_{5/2}$, $2s_{1/2}$, and $1d_{3/2}$ orbitals are all active (refer to Figure 4.1). The MKW interaction is constructed in the following manner. First of all, the single-particle energies were chosen to reproduce single-particle states in A = 17 nuclei and single-hole states in A = 15 nuclei with the assumption of a closed $1s$-$1p$ shell configuration for ^{16}O. The residual interaction matrix elements connecting the 1p-shell orbits were taken from a fit to $1p$-shell energy levels in the A = 10–15 mass region obtained by Millener [Mi86]. The complete p-shell effective interaction comprises a total of seventeen parameters, two single-particle energies and fifteen two-body matrix elements. The interaction matrix elements connecting the $2s1d$-shell orbitals were taken from a fit to $2s1d$-shell energy levels in the A = 18–38 mass region obtained by Wildenthal [Wi83A]. The complete ds-shell effective interaction comprises a total of sixty-six parameters, three single-particle energies and sixty-three two-body matrix elements. Lastly, the cross-shell interaction matrix elements connecting both the $1p$-shell and $2s1d$-shell orbitals were calculated with the residual interaction of Millener and Kurath [Mi75]. This contributes approximately twelve additional parameters.

The theoretically predicted shell-model Gamow-Teller β-decay strengths are expressed in terms of a "B(GT)" value which is directly related to the nuclear matrix element, $|M_{fi}|^2$:

$$B(GT) \propto |M_{fi}|^2 \tag{4.5}$$

Recall from Chapter I that the nuclear matrix element accounts for the overlap of

initial and final nuclear states. Experimentally determined ft values (comparative half-lives) are related to B(GT) values through the following expression:

$$B(GT) = \frac{6177\ s}{ft} \tag{4.6}$$

The 6177 s in the above equation is arrived at by combining constants used to calculate the decay constant and ft values. Table 4.2 presents the comparison of the experimentally determined ^{15}B Gamow-Teller β-decay strengths to those predicted by the MKW shell-model calculations; Figure 4.2 graphically displays this comparison. The theoretical B(GT) values include the $(g_a/g_v)^2$ factor that properly accounts for the weak-interaction axial-vector and vector coupling constants (denoted by g_a and g_v, respectively) for the decay of a neutron into a proton. The theoretical B(GT) values have also been multiplied by a factor of 0.6 to take into account the empirical quenching observed for Gamow-Teller decay strengths in *sd*-shell nuclei [Br88]. An investigation of hundreds of experimentally determined ft values for *sd*-shell nuclei has been conducted by Brown *et al.* [Br85]. This investigation showed that experimentally determined ft values were consistently larger than the theoretically predicted ones. Multiplying the theoretical values by a 0.6 "quenching factor" generally brings about good agreement among the two sets of values.

Referring to Table 4.2 and Figure 4.2, agreement among the experimentally determined and theoretically predicted Gamow-Teller β-decay strengths is quite good for the largest decay branch (62.8% branch to the 3.103 Mev, $\frac{1}{2}^-$ state) while the shell-model underestimates the decay strengths to the higher lying states. In addition, the shell-model predicts a total decay branch of less than 0.8% to all remaining negative parity states in ^{15}C (states lying above the first five negative parity states), in agreement with the experimental results.

Concerning the shell-model underestimation of allowed Gamow-Teller β-decay

strengths to the higher lying states in ^{15}C, it is noted that in this *psd* model space the active protons occupy the $1p$ shell and the active neutrons occupy the $2s1d$ shell. Previously half-life [Cu86] as well as other Gamow-Teller β-decay strength [Sn83] discrepancies between the model predictions and experimental data have been found with this type of configuration. The allowed Gamow-Teller β-decay of ^{16}C to states in ^{16}N is particularly noted (notice $^{16}_{6}C_{10}$ has only one more proton occupying the $1p$ shell than $^{15}_{5}B_{10}$, the neutrons occupying the $2s1d$ shell are identical for the two nuclei); here, essentially 100% of the ^{16}C β-decay strength feeds the 3.36 MeV level ($\approx$84%) and the 4.32 MeV level ($\approx$16%) in ^{16}N. Model predictions using the complete *psd* model space and Millener-Kurath interaction to connect the $1p$ protons and $2s1d$ neutrons predicts ^{16}C B(GT) values noticeably *lower* than that experimentally observed [Sn83]. It is proposed that a better determination of the cross-shell residual interaction between protons and neutrons for these nuclei might improve these discrepancies [Cu86].

Additional calculations were performed to estimate the first-forbidden β-decay strengths to the ground state ($\frac{1}{2}^+$) and first excited state ($\frac{5}{2}^+$) of ^{15}C. These calculations are different from the allowed-decay calculations described above and employ a first-forbidden decay operator. The calculations were performed with *psd* wave functions using the Behrens-Buhring formulation [Be72] as explicated by Warburton *et al.* [Wa88]. The results obtained with harmonic-oscillator radial wave functions are a branch of 0.53% to the ground state and 0.52% to the first excited state. The results obtained with Woods-Saxon wave functions are 0.23% to the ground state and 0.23% to the first excited state. The latter value for the total calculated branching ratio of 0.46% is in exceptionally good agreement with the experimental value of 0.46$\pm$0.08%.

Table 4.1: Measured and predicted Gamow-Teller β-decay strengths to the lowest $\frac{1}{2}^-$, $\frac{5}{2}^-$, $\frac{3}{2}^-$, $\frac{1}{2}^-$ and $\frac{5}{2}^-$ [a] states in mass 15; also included are the measured and predicted energy levels of ^{15}C populated. The 3.103 MeV ^{15}C level was adjusted in the shell-model calculations to match the experimental value. (BR) denotes branching ratio. All energies are in MeV.

State	^{15}B (*this work*)			A = 15 shell-model calculations	
J^π	BR (%)	^{15}C (E_x)	B(GT) [b]	^{15}C (E_x)	B(GT)
$\frac{1}{2}^-$	62.8±2.4	3.103 (calibration)	0.282±0.012	3.103 (adjusted)	0.312
$\frac{5}{2}^-$	7.7±1.3	4.23±0.02	0.046±0.010	4.876	0.022
$\frac{3}{2}^-$	22.8±1.2	4.66±0.01	0.170±0.015	5.757	0.112
$\frac{1}{2}^-$	4.1±0.9	5.85±0.04	0.049±0.010	6.333	0.010
$\frac{5}{2}^-$ [a]	1.8±0.5	6.31±0.07	0.024±0.007	6.881	0.001

[a] Shell-model calculations predict a $J^\pi = \frac{5}{2}^-$ state following the $\frac{1}{2}^-$ state. Experimentally, there is uncertainty as to the J^π of this state (see last paragraph of Chapter 3, Section 5).

[b] B(GT) values calculated from Eq. 4.6.

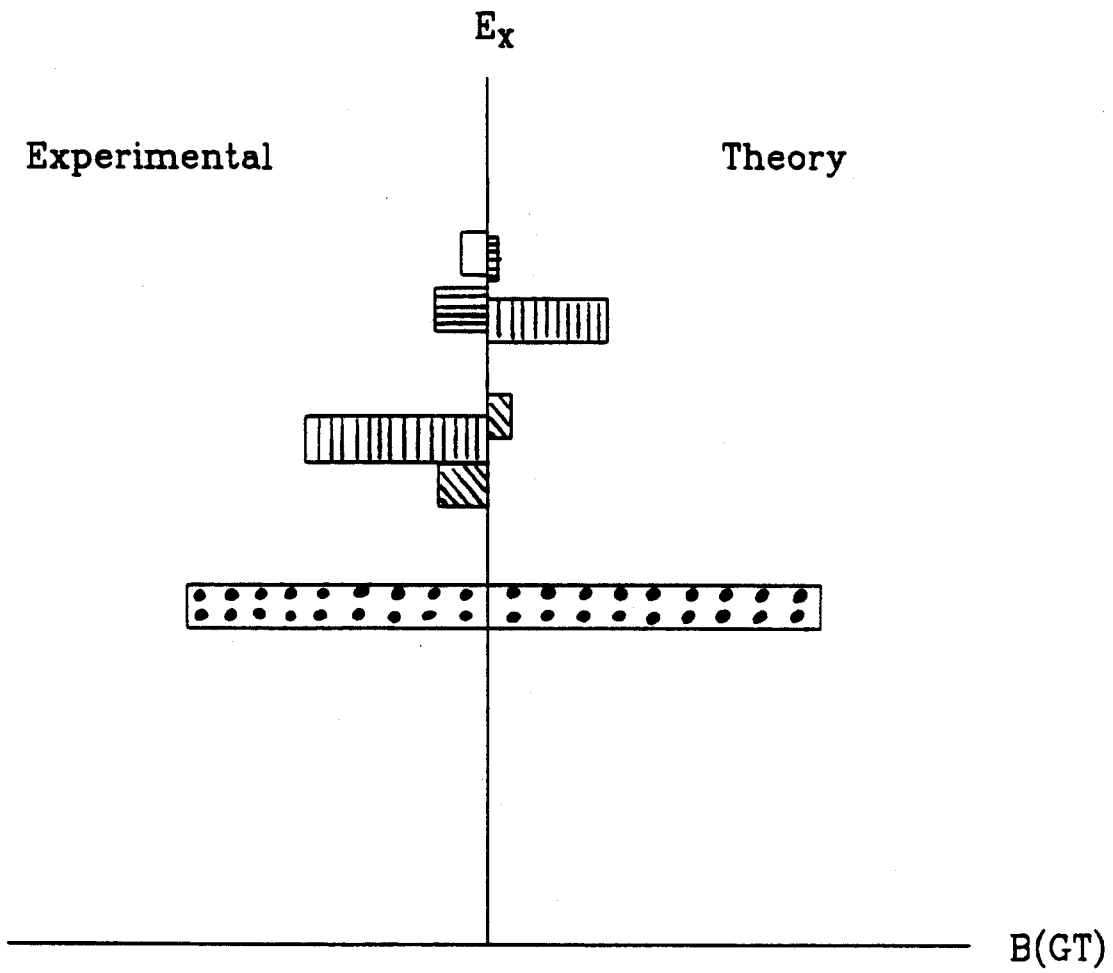

Figure 4.2: Graphical comparison of the experimentally determined Gamow-Teller β-decay strengths for ^{15}B and those predicted by the theoretical shell-model for mass 15. The y-axis represents the energy levels (E_x) in ^{15}C. Refer to Table 4.1 for the actual B(GT) and E_x values.

Chapter 5

Conclusions

In the present work, a number of goals have been successfully reached. It has been demonstrated that the NSCL A1200 radioactive beam device is capable of producing relatively pure radioactive secondary beams at exceptional rates, and in addition, these radioactive beams can be successfully transported to low background experimental vaults where decay studies can be conducted. Comparison of the number of ^{15}B atoms created and studied in the present work using the A1200 to the number that where available in previous studies at the NSCL before the A1200 shows an approximately 1700-fold improvement. It is reasonable to conclude that the future looks optimistic for the decay studies of many other exotic nuclei at the NSCL.

The newly constructed NSCL neutron detector array, a device designed for the study of β-delayed neutron emitting nuclei, was used for the first time in the present study of ^{15}B decay. This provided an opportunity to assess the array's performance and learn about its capabilities and limitations, and identify areas where improvements could be made. A "working protocol" has been established for the use of the array. The electronic setup used in the ^{15}B decay study, outlined in the present work, is the basis for other studies only needing those changes necessary to customize the implantation detector. A technique to determine the neutron detection efficiency of the array using a PuBe neutron source has been demonstrated. While this source

produces neutrons with a continuum of kinetic energies, it has been shown that a time-of-flight technique can be utilized to determine the neutron detection efficiency using γ-ray/neutron coincidences. Monte-Carlo neutron detection efficiency calculations have also been performed for the array, and compared to the PuBe source results. It appears that the neutron detection efficiencies obtained for the array detectors using the PuBe source were adequate and reliable in determining the "detector solid angle independent" *relative* ^{15}B β-decay branching ratios, however if ***absolute*** branching ratios are to be determined from PuBe source determined detector efficiencies, work is needed in assessing the background attributed to this neutron source (this is discussed in the next to last paragraph of Chapter III, Section 5). In addition, different techniques have been explored to investigate the array's ability to provide position information of detected neutrons. Here a technique employing timing signals of left vs. right detector sides showed position resolution of 13 cm (FWHM) could be achieved (this opens new possibilities for using the array in neutron correlation experiments).

In the present work, the half-life for ^{15}B inclusive β-emission was observed to be 10.3$\pm$0.2 ms, and an additional measurement requiring β-neutron coincidences gave a value for this half-life of 10.5$\pm$0.5 ms. Both these values are in good agreement with the value of 10.5$\pm$0.3 ms in the literature, and confirm the ^{15}B half-life value. The first β-delayed neutron spectroscopy of ^{15}B was performed using the neutron detector array. The population of the first five previously known negative parity states (J^{π} assignments for the first four states being known, the fifth having some uncertainty) that are neutron unbound in ^{15}C was observed. In addition, the weak β-decay branch to the ^{15}C particle bound ground state and first excited state was observed and established to be 0.46$\pm$0.08%. Taking this as the zero-neutron emission probability, P_{0n}, and the measurement of P_{2n} = 0.4$\pm$0.2% by Reeder *et al.* [Re90], it

was concluded that 99.14±0.28% of the ^{15}B β-decays populate the five lowest negative parity states in ^{15}C. As a result of these measurements the ^{15}B β-decay branching ratios have been established as 62.8±2.4%, 7.7±1.3%, 22.8±1.6%, and 4.1±0.9% to the known (E_x(MeV),J^π) 3.103, $\frac{1}{2}^-$; 4.220, $\frac{5}{2}^-$; 4.657, $\frac{3}{2}^-$; and 5.866, $\frac{1}{2}^-$ ^{15}C states, respectively. In addition, it was deduced that the 1.8±0.5% branch to the ^{15}C state at 6.31±0.07 MeV must be an allowed β-decay. This helps to limit its J^π assignment to $\frac{1}{2}^-$, $\frac{3}{2}^-$, or $\frac{5}{2}^-$. The reported β-decay branching ratios are supported by (1) a measurement of 67.1±7.7% as the *absolute* β-decay branch to the 3.103, $\frac{1}{2}^-$ ^{15}C state, and (2) the "adjusted" (refer to Chapter III, Section 5 of the present work) P_{1n} of 99% for ^{15}B from the Reeder *et al.* [Re91] measurement. As a result of the present work, therefore, P_{0n} and P_{1n} for ^{15}B, as well as β-decay branching ratios have been established. This establishes ^{15}B as a potentially useful neutron detector calibration standard for other β-delayed neutron experiments.

Among limitations of the neutron detector array and areas where improvements could be made in addition to the work already addressed needed involving the PuBe source efficiency measurements, first and foremost is the neutron energy threshold of approximately 0.7 MeV. Since the amount of light produced in the plastic scintillation neutron detector is a function of neutron energy, it may be the case that this detector design is not adequate for the detection of low energy neutrons. The present detector design appears to be best for the detection of neutrons with kinetic energies in the range of 2 to 7 MeV. Presently, tests are being conducted to see if a third photo-multiplier tube placed at the center of a detector element can improve the detector's ability to detect low energy neutrons. Another area of concern is multiple neutron detection using the array. In the present work, the low P_{2n} for ^{15}B was impossible to differeniate from the background. For other situations where the P_{2n} is significantly higher (compared to the 0.4% P_{2n} for ^{15}B), two-neutron decay studies may be very

feasible using the array. The advantages of using the array for such studies are the exceptionally large solid angle (1.9 steradians) and the ability to determine neutron positions; this opens the possibility of performing neutron angular correlation experiments. It should be noted that the efficiency to detect more than two neutrons at once (for example P_{3n}, P_{4n}, etc.) drops dramatically due to the fractional solid angle coverage ($\approx 1/9$) and the intrinsic efficiency ($\approx 1/5$), and the feasibility of such measurements using the array is probably low.

The agreement among the experimentally determined ^{15}B β-decay strengths from the present work and the shell-model predictions using the Millener-Kurath-Wildenthal interaction is, overall, quite good. It is thought that a better determination of the cross-shell interaction between protons and neutrons for the ^{15}B case might improve its β-decay description of exotic nuclei; the results of this work can aid in improving these shell-model interactions.

Recently, two experiments were performed at the NSCL using the neutron detector array. These were decay studies of the β-delayed neutron emitting nuclei ^{18}N and ^{14}Be. The array appeared to perform well in these experiments and analysis of the results are presently underway. An experiment to study multiple neutrons from the decay of ^{11}Li using the array is planned for the near future. Modifications are presently taking place which will allow for coincidence measurements between charged particles and neutrons from the decay of ^{11}Li. With the impressive exotic nuclei production rates of the A1200 separator, it is thought that the array will be useful in studying many other β-delayed neutron emitters in the coming years.

Bibliography

[Aj86] F. Ajzenberg-Selove, Nucl. Phys. **A460**, 1 (1986).

[Aj88] F. Ajzenberg-Selove, Nucl. Phys. **A490**, 1 (1988).

[Aj91] F. Ajzenberg-Selove, Nucl. Phys. **A523**, 1 (1991).

[Be72] H. Behrens and W. Buhring, Nucl. Phys. **A162**, 111 (1972); "Electron Radial Wave Functions and Nuclear β-Decay" (Clarenson Press, Oxford) 1982.

[Bo74] J.D. Bowman, A.M. Poskanzer, R.G. Korteling, and G.W. Butler, Phys. Rev. C **9**, 836 (1974).

[Br85] B.A. Brown and B.H. Wildenthal, AD and NDT **33**, 347 (1985).

[Br88] B.A. Brown and B.H. Wildenthal, Ann. Rev. Part. Sci. **38**, 29 (1988).

[Br90] B.A. Brown, private communication.

[Ce79] R.A. Cecil, B.D. Anderson, and R. Madey, Nucl. Instr. and Meth. **161**, 439 (1979).

[Cu86] M.S. Curtin, L.H. Harwood, J.A. Nolen, Jr., B. Sherrill, Z.Q. Xie, and B.A. Brown, Phys. Rev. Lett. **56**, 34 (1986).

[Du84] J.P. Dufour, S. Beraud-Sudreau, R. Del Moral, H. Emmermann, A. Fleury, F. Hubert, C. Poinot, M. Pravikoff, J. Frehaut, M. Beau, A. Bertin, G. Giraudet, A. Huck, G. Klotz, C. Miehe, C. Richard-Serre, and H. Delagrange, Z. Phys. **A319**, 237 (1984).

[Fr81] G. Friedlander, J.W. Kennedy, E.S. Macias, and J.M. Miller, "Nuclear and Radiochemistry" (John Wiley and Sons, New York) 1981.

[Ha81] L.H. Harwood and J.A. Nolen, Jr., Nucl. Instr. and Meth. **186**, 435 (1981).

[Hu90] F. Hubert, R. Bimbot, and H. Gauvin, AD and NDT **46**, 1 (1990).

[Kr88] K. Krane, "Introductory Nuclear Physics" (John Wiley and Sons, New York) 1988.

[Le89] M. Lewitowicz, Y.E. Penionzhkevich, A.G. Artukh, A.M. Kalinin, V.V. Kamanin, S.M. Lukyanov, N.H. Chau, A.C. Mueller, D. Guillemaud-Mueller, R. Anne, D. Bazin, C. Detraz, D. Guerreau, M.G. Saint-Laurent, V. Borrel, J.C. Jacmart, F. Pougheon, A. Richard, and W.D. Schmidt-Ott, Nucl. Phys. **A496**, 477 (1989).

[Mi75] D.J. Millener and D. Kurath, Nucl. Phys. **A255**, 315 (1975).

[Mi86] D.J. Millener, private communication.

[Mi89] David Mikolas, Doctoral Dissertation, Michigan State University, 1989.

[Mu84] J.A. Musser and J.D. Stevenson, Phys. Rev. Lett. **53**, 2544 (1984).

[Mu88] A.C. Mueller, D. Bazin, W.D. Schmidt-Ott, R. Anne, D. Guerreau, D. Guillemaud-Mueller, M.G. Saint-Laurent, V. Borrel, J.C. Jacmart, F. Pougheon, and A. Richard, Z. Phys. **A330**, 63 (1988).

[Pa72] L. Pages, E. Bertel, H. Joffre, and L. Sklavenitis, AD and NDT **4**, 1 (1972).

[Po66] A.M. Poskanzer, S.W. Cosper, E.K. Hyde, and J. Cerny, Phys. Rev. Lett. **17**, 1271 (1966).

[Re90] P.L. Reeder, R.A. Warner, W.K. Hensley, D.J. Vieira, and J.M. Wouters, "Exotic Nuclear Spectroscopy", Edited by Wm. C. McHarris (Plenum Press, New York) 1990.

[Re91] P.L. Reeder, R.A. Warner, W.K. Hensley, D.J. Vieira, and J.M. Wouters, Phys. Rev. C **44**, 1435 (1991).

[Sa88] M. Samuel, B.A. Brown, D. Mikolas, J. Nolen, B. Sherrill, J. Stevenson, J.S. Winfield, and Z.Q. Xie, Phys. Rev. C **37**, 1314 (1988).

[Sc83] H.W. Schuh, PHAEDRUS, Institut fur Kerphysik der Universitat zu Koeln (1983) [unpublished].

[Sh91] B.M. Sherrill, D.J. Morrissey, J.A. Nolen, Jr., and J.A. Winger, Nucl. Instrum. Methods Phys. Res. **B56/57**, 1106 (1991).

[Sn83] K.A. Snover, E.G. Adelberger, P.G. Ikossi, and B.A. Brown, Phys. Rev. C **27**, 1837 (1983).

[Wa88] E.K. Warburton, J.A. Becker, B.A. Brown, and D.J. Millener, Ann. Phys. **187**, 471 (1988).

[Wi74] D.H. Wilkinson and B.E. Macefield, Nucl. Phys. **A232**, 58 (1974).

[Wi83] B.H. Wildenthal, M.S. Curtin, and B.A. Brown, Phys. Rev. C **28**, 1343 (1983).

[Wi83A] B.H. Wildenthal, "Progress in Particle and Nuclear Physics" (Pergamon, New York) 1983.

[Wi91] J.A. Winger, B.M. Sherrill, and D.J. Morrissey, in Proceedings of the 12^{th} International Conference on Electromagnetic Isotope Separators and Techniques Related to Their Applications, Sendai, Japan, Sept. 2–6, 1991 [Nucl. Instr. and Meth. (to be published)].

[Wo54] R.D. Woods and D.S. Saxon, Phys. Rev. **95**, 577 (1954).

[Wo90] S.S.M. Wong, "Introductory Nuclear Physics" (Prentice Hall, New Jersey) 1990.